UNIVERSITÀ DEGLI STUDI DI PALERMO

Dottorato in Scienze della Terra e del Mare.

Dipartimento di Scienze della Terra e del Mare.

Settore Scientifico Disciplinare GEO/08.

Constrains on mantle, slab and crustal contributions to major volatiles and noble gases along the Andean Volcanic Belt

IL DOTTORE

Joao Pedro Nogueira Lages

IL COORDINATORE

Prof. Alessandro Aiuppa

IL TUTOR

Prof. Alessandro Aiuppa

IL CO TUTOR

Dr. Andrea Lucca Rizzo

CICLO XXXII

ANNO CONSEGUIMENTO TITOLO 2020

Abstract

Major volatiles and trace volatiles, like He, are key for understanding the lithospheric mantle signature and the complex role of subduction in global geochemical cycles, as well as fluid migration processes governing volcanic gas fluxes and compositions of geochemical elements along volcanic arcs.

Our investigation reports 3 years of in-situ measurements of volcanic gas compositions, ground-based remote sensing SO_2 flux measurements and noble gas analyzes of fluid inclusions (FIs) trapped within eruptive products across three of the four arc segments of the Andean Volcanic Belt: Northern, Central and Southern volcanic zones. Here we discuss transport mechanisms and geochemical patterns of magmatic fluids in subduction zones to shed light on the origin and recycling efficiency of volatiles, including Noble gases, at arc trenches.

New volcanic gas compositions and volatile fluxes here reported for Nevado del Ruiz, Galeras, and Purace, three of the most persistently degassing volcanoes located in the Colombian Arc Segment of the Northern Volcanic Zone indicate that this arc segment contributes about 50% to the total subaerial CO_2 budget of the Andean Volcanic Belt. Furthermore, our work highlights the northward increase in carbon-rich sediment input into the mantle wedge via slab fluids and melts that is reflected in magmatic CO_2/S_T values far higher than those reported for Southern Volcanic Zone and Central Volcanic Zone volcanoes. We estimate that about 20% (~1.3 Mt C/year) of the C being subducted (~6.19 Mt C/year) gets resurfaced through subaerial volcanic gas emissions in Colombia (Nevado del Ruiz ~0.7 Mt C/year).

On the other hand, our work suggests the same mechanisms to play a negligible role in the arc-scale variations of Noble gas signatures, especially $^3He/^4He$, here put in evidence by our new reported results from fluid inclusions in olivine and pyroxene phenocrysts from Andean eruptive products. For instance, Noble gas abundances and isotope signatures of eruptive products from five of the most active volcanoes along the Northern Volcanic Zone, as well as updated fumarolic gas data for Galeras (Colombia) shows a substantial discrepancy between the consistently measured isotope signature of eruptive products from the Ecuadorian arc segment (~7.2 R_A) and values reported for the Colombian part of the NVZ (~8.5 R_A). Previous studies into whole-rock trace element of lavas erupted from these volcanic centers suggest minor variations along the main magmatic arc. Instead, this study proposes that significant disparities in crustal thickness (from <35 km at the Northern-most part of the segment, to >50 km at the Ecuadorian arc segment) may factor largely into the variability recorded on our data set. Therefore, melting and/or assimilation of crustal lithologies (U- and Th-rich) may be the predominant process of contamination of MORB-like fluids at volcanic arc settings characterized by exceptionally thick continental crusts. This trend is even more pronounced in the Central Volcanic Zone for volcanoes like Sabancaya, Ubinas and Misti, where the overlying continental crust reaches a maximum of ~70 km and $^3He/^4He$ isotope ratios consistently show values below the MORB range (~8±1 R_A).

Therefore, this work suggests a possible de-coupling between slab processes contributing to regional trends in CO_2/S_T and shallower crustal controls on Noble gas chemistry in subduction zones, to be confirmed with more detailed studies of volcanic arcs worldwide.

Table of Contents

List of figures

List of tables

CHAPTER 1

Introduction

Volcanic activity and metamorphic processes are the main geological agents controlling the carbon cycle on our planet, from the Earth's interior to surface reservoirs. Here, active, passive and diffuse tectonic and volcanic degassing play a key role in balancing the input and output budgets of Carbon at arc trenches, fed at depth by Carbon removal through silicate weathering and the subduction of carbon-bearing marine deposits, which happen over timescales of millions of years.

Subduction zones are the prevailing geodynamic process through which volatiles (H_2O, CO_2, sulfur, chlorine and fluorine) and noble gases (such as helium, argon and neon) are transferred between the Earth's mantle and the atmosphere. At volcanic arcs, the input of altered oceanic crust, slab sediments and serpentinized lithospheric mantle play a key role in recycling major volatiles such as Carbon and Sulfur, as well as Hydrogen, Chlorine and many other volatile components (including noble gases), into the Earth's upper mantle. Magmatism in these regions is notoriously rich in water due to the release of hydrous fluids into the overlying mantle wedge by the descending oceanic slab, which decreases the melting temperature of the mantle, causing it to melt and subsequently rise by buoyancy producing chains of volcanoes such as those found around the Pacific "Ring of Fire".

Over the span of this PhD project, our investigation focused on studying fluid's migration through major volatiles and noble gases source signatures, as well as geochemical compositions inherited through the complex migration record of fluids measured in rocks (melt and fluid inclusions) and/or at the surface, as subaerial gas emissions from open vent degassing volcanoes, fumarolic fields and/or geothermal areas. We here attempt to correlate arc-scale volatile and noble gas compositions with other along-arc geochemical, geophysical and petrological parameters, to improve upon the ability to decode the complex intermingling of geochemical agents (such as the subduction plate, the upper mantle and shallower crustal reservoirs) affecting global patterns of magmatic fluids geochemistry. Therefore, quantifying and understanding the role of along-arc global geochemical cycles bears crucial insights into the nature and scale of chemical heterogeneities in the Earth's mantle, as well as our atmosphere's past and present compositional evolution, since volatile emissions are thought to have been implicated in regulating atmospheric CO_2 levels, temperature fluctuations, oxygen rise, and biosphere evolution over the planet history (Gaillard et al., 2011; Edmond and Huh, 2003; Pagani et al., 2005; Johnston et al., 2011; Lee et al., 2013).

Therefore, we have chosen to focus on subduction zone dynamics and attempt to improve and add to our current understanding of source, fate and cycling of volatiles between the Earth's reservoirs. Clear chemical distinctions in compositions of volcanic-arc gases being emitted at different regions of our planet raise the question, and reinforce the need, to quantify and constrain the role

of the slab and subducted sediments, the underlying crust and the mantle in compositions of gases vented at active volcanoes. Magmas originating at such tectonic settings have higher volatile concentrations than magmas derived from mid-ocean ridges (Marty et al. 1989; Giggenbach, 1992a; Giggenbach, 1996), and volatiles contents in magmas and exsolved gas may help constrain the relative contributions of the subducted slab, depleted vs. undepleted mantle, crustal assimilation (e.g., de-carbonation and dehydration of crustal rocks) and processes of magma differentiation in the crust. Although the hydrous nature of volcanic arc gases (Fischer and Chiodini, 2015) and magmas (Wallace and Anderson, 1999; Wallace, 2005) provide clear evidence for effective recycling of subducted H_2O via de-hydration reactions in the slab (Kerrick and Connolly, 2001a, b; Schmidt and Poli, 2014), the transportation effectiveness via slab of other volatile species (such as carbon) remains ambiguous. Furthermore, subducted materials in slabs are recycled into the deep mantle, but light noble gases are often assumed to be returned to the surface through arc volcanism with little, if any transferred to the deep mantle (Staudacher and Allègre, 1988).

Our scientific communities' understanding of global geochemical cycles has been significantly skewed towards arc regions, and individual volcanic system for which data has been collected extensively over the years (e.g., Mount Etna, Sicily). Under Deep Earth Carbon Degassing (DECADE) initiative of the Deep Carbon Observatory we here attempted to direct our efforts to less studied arc regions and improve upon the present volcanic gas CO_2/S_T dataset, currently unconstrained volatile budgets, and give contribution to unceasing efforts to quantify global Carbon emissions from volcanism on Earth (Aiuppa et al., 2019; Werner et al., 2019).

Furthermore, as sophisticated volcanic gas instrumentation is developed, our investigation into the chemistry of volcanic gases has also led us to focused on developing monitoring infrastructures that allowed continuous acquisition of real time data of plume composition, here integrated to help mitigate volcanic risk at highly hazardous regions.

1.1. Overview of developed research activities and structure of the dissertation

This dissertation starts with an overview of sampling methods and global geochemical datasets of noble gases and major volatiles at volcanic arcs (Chapter 2), to then focus on the Andean Volcanic Belt (AVB; Chapter 3), where our investigation was conducted over the 3-year span of this PhD, the geodynamics and tectonic setting of the arc and available volcanic gas (composition and fluxes) and Noble gases data in the literature prior to the beginning of this program. Chapter 4 of this dissertation reports volcanic gas compositions and volatile fluxes acquired during the first year of this PhD from three of the most persistently degassing volcanoes along the Colombian Arc Segment (Northern Volcanic Zone), Nevado del Ruiz, Purace and Galeras, in which we attempted to constrain the contribution of this arc segment to the overall volatile budget of the Andean trench. From these initial field work campaigns, the opportunity arose to install a MultiGAS station and permanently monitor volcanic gas emissions at Nevado del Ruiz. With incredible logistical and technical support from UNIPA and SGC-OVS Manizales real-time volcanic gas data was first acquired in July 2017. Chapter 5 integrates our CO_2/S_T 3-year time-series with cotemporally-

acquired SO_2 flux data from the global Network for Observation of Volcanic and Atmospheric Change (NOVAC), in order to improve the monitoring network of an historically hazardous volcano such as Nevado del Ruiz, by setting robust background datasets of volcanic gas compositions for this volcano during a period of mild volcanic activity. Chapter 6 investigates the Noble gas signatures in fluid inclusions from lavas and scoriae layers from active volcanic centers along the Northern Volcanic Zone (NVZ; Ecuador and Colombia) in order to isotopically characterize mantle sources, constrain along-arc fluid migration patterns and investigate the geophysically-governed along-arc isotope signatures of northern magmatic fluids. Finally, chapter 7 describes similar scientific approaches to other Andean volcanoes in terms of the characterization of volcanic gas emissions (Sabancaya and Ubinas, Peru) and noble gas isotope signatures of free gases (Peru) and in fluid inclusions (Peru and Villarrica) and reflects upon along-arc noble gas and composition data trends evidenced in this work. The work developed throughout the course of this PhD, along with the main remarks and unanswered scientific questions are summarized in Chapter 8 that concludes this dissertation.

CHAPTER 2

Noble Gases and Major Volatiles at Volcanic Arcs: an overview of sampling methods, global geochemical datasets and limitations to current scientific approaches

The attempt to constrain and somewhat quantify arc volatile fluxes, especially for greenhouse gases such as CO_2, that play a huge role at controlling temperatures on the Earth's surface, is critical for studies related to geochemical cycles at a planetary scale. This has been recently investigated by Dasgupta and Hirschmann (2010), Dasgupta (2013) and Kelemen and Manning (2015). Such studies provide calculations of carbon solubility in aqueous fluids and carbonates stability (considering that the largest portion of carbon input in subduction zones derives from carbonate minerals) during the subduction process. Their estimates of carbon amounts stored in the different Earth's reservoirs are illustrated in Figure 2.1.

Extensive compilations of gas flux data from arc volcanoes (Hilton et al., 2002; Burton et al., 2013; Aiuppa et al., 2019) reported estimates of about 18 Mt C/year to 43 Mt C/year (Figure 2.1). These studies were largely based on remote sensed SO_2 flux measurements in volcanic gas plumes and/or strong-enough SO_2 emitters that release sufficiently high amounts of SO_2 to be detected from space (e.g., the Ozone Monitoring Instrument, on NASA's Aura satellite between 2005–2015; Carn et al., 2017). These measurements, when coupled with measured CO_2/S_T ratios in free gases (obtained in-situ by gas sensing instruments) and magmatic fluids, as well as CO_2/S_T ratios predicted from trace element composition at volcanoes for which gas information is still insufficient (Aiuppa et al., 2019), allow estimates of CO_2 emitted out of volcanoes via subaerial gas emissions or fumarolic fields.

However, the origin of volatiles being vented along arc trenches remains somewhat ambiguous. Helium, in particular ^3He, is perhaps one of most important geochemical parameters among volatile species because of its primordial signature (Lupton, 1983; Mamyrin and Tolstikhin, 1984), and its abundance and isotope signature ($^3He/^4He$) in magmatic fluids has long been taken into consideration when trying to constrain tectonic controls and relative importance of the crust, mantle and subducted slab contributions to mantle-derived melts (e.g., Poreda and Craig, 1989; Hilton and Craig, 1989; Hilton et al., 1993; Hilton et al., 2002; Sano and Fischer, 2012). Previous noble gas global compilations have attributed a mean $^3He/^4He$ ratio to arc-related volcanism of 5.4 ± 1.9 R_A (Hilton et al., 2002 estimates for all arc segments), which is considerably lower than the expected MORB range (8 ± 1). Where CO_2 contents correlate with ^3He, it is inferred that most of the CO_2 is introduced from the mantle into the base of arc crust. Where CO_2 and ^3He are correlated, and $CO_2/^3He$ ratios are lower than in other tectonic settings, and/or where $\delta^{13}C$ reflects input of non-mantle carbon, this is interpreted as recycling of carbon from subducting sediment and altered oceanic crust.

However, arc volcanoes, especially those of continental arcs, may also emit CO_2 added to magmas during metamorphism of carbon-bearing lithologies within the crust. It is, therefore, essential to constrain the contribution of each individual volatile source to the output of volatiles along volcanic arcs and to validate the arc-scale variability in volcanic gas emissions (composition and flux) based on regional and global variations of estimated volatile inputs at subduction zones.

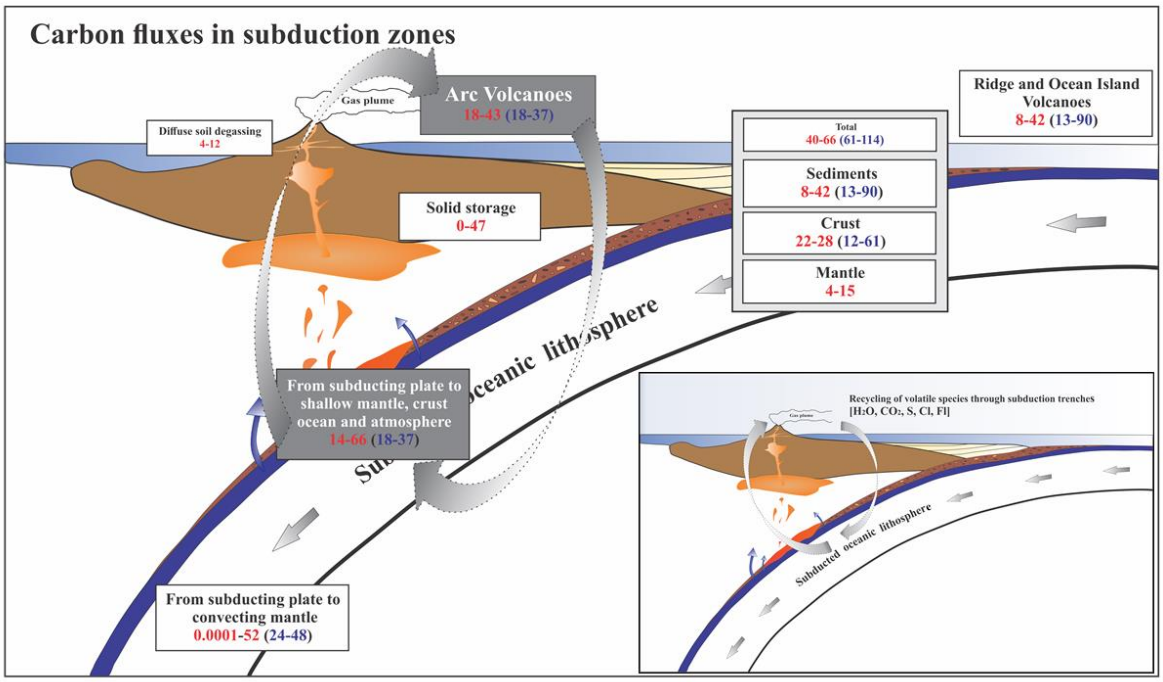

Figure 2.1: Schematic illustration of major carbon fluxes at subduction zones (adapted from Kelemen and Manning, 2015, to which correspond the values in red; values in blue are from Dasgupta and Hirschmann (2010) and are given as a comparison).

2.1. Source discrimination and volatile output from subduction zone volcanism

Subduction zones are the main tectonic regime through which volatiles, including noble gases, are returned to the mantle. Therefore, constraining volatile budgets and inventories at arc trenches is crucial to understanding volcanic gas emissions on Earth and the nature and efficiency of recycling between the mantle and the atmosphere, hydrosphere and crust.

2.1.1. Volcanic gas compositions

Carbon dioxide degassing from active convergent margins is sourced from three main "reservoirs": (i) CO_2 dissolved in the mantle; (ii) recycled CO_2 from subducted slab (e.g., Marty and Tolstikhin 1998 and, more recently, Aiuppa et al., 2017); and (iii) decarbonation of shallow crustal material (e.g., Troll et al. 2012, Mason et al., 2017). Unravelling the relative proportions of mantle and crustal carbon is possible through the investigation of the isotopic composition of emitted carbon (e.g., Chiodini et al. 2011). For instance, for a subset of arcs such as Central America, part of the Andes and Indonesia, where the mature, continental nature of the overlying crust shows similar characteristics, the high $\delta^{13}C$ values of volcanic gases that correlate with high proportions of ^4He (radiogenic helium) have been attributed to Carbon being sourced predominantly from crustal

limestones (Mason et al., 2017). For the Costa Rica segment of the Central America Volcanic Arc other authors developed a model which suggests that ~91% of carbon released from the slab/mantle beneath the Costa Rican forearc is sequestered within the crust by calcite deposition with an additional ~3.3% incorporated into autotrophic biomass (Barry et al., 2019).

On the other hand, high-temperature arc gas emissions in the form of Carbon dioxide (CO_2) and Sulfur dioxide (SO_2) analyzed over the years (Oppenheimer et al. 2011, 2014) yield isotope compositions that transpire slab-derived fluid contributions to emitted volcanic gases (Sano and Marty, 1988; de Hoog et al., 2001; Hilton et al., 2002; Fischer and Sano, 2013; Kagoshima et al., 2015). However, the large compositional heterogeneity of subducted materials leads to difficult estimates of Carbon and Sulfur input fluxes at subduction zones (Plank and Langumir, 1998; Jarrard, 2003; Freundt et al., 2014; Plank, 2014), which adds to the necessity of constraining the contribution of such fluids to the amounts of Carbon being vented at the Earth's surface (Aiuppa et al., 2017). Bebout (2014), however, argues that slab-derived and crustal sedimentary Carbon (and Sulfur) are likely to have overlapping isotopic signatures, which would ultimately undermine our capacity to accurately discriminate crustal contributions to emitted arc gases and the atmosphere.

Aiuppa et al. (2017) studied the compositional heterogeneities of volcanic gas compositions (e.g., CO_2/S_T), put in evidence by global data sets (e.g., Hilton et al., 2002; Fischer and Marty, 2005; Fischer, 2008), and suggested that different arc regions receive substantially distinct volatile inputs from depth. The relative abundance of gas species within the exsolving magmas is, therefore, one way of constraining the contributions of different volatile sources at subduction zones. This is because the potential involved sources above described (the depleted mantle, CO_2/S_T of 0.3-0.8, Saal et al., 2002; subducted sediments/crust, CO_2/S_T of 1-100, Freundt et al., 2014; and CO_2-rich fluids from limestone de-carbonatation (CO_2/S_T >>100) exhibit distinct CO_2/S_T signature (Aiuppa et al., 2017). A strong example is, for instance, the along-arc variation recorded in volcanic gas CO_2/S_T ratios in the Nicaragua-Costa Rica segment of the Central American Volcanic Arc (CAVA). The increase to about ~3 in CO_2/S_T measured in Nicaragua, from those measured in Costa Rica of ~0.5 – 1.0 has been interpreted as due to increased contributions of slab-derived fluids into the melt, relative to more-MORB-like magmatic volatile signature in Costa Rica (Aiuppa et al., 2014). In terms of the relative abundance of Carbon and Sulfur species in magmas, Aiuppa et al. (2017) suggest CO_2-rich volcanoes (higher CO_2/S_T in-plume ratios) are mainly sourced by de-volatilization of C-rich sediments, while (C-poorer) terrigenous sediments and/or AOC are increasingly involved in volatile generation at C-poor volcanic systems.

2.2. Noble gases at subduction zones

Tectonic settings are geodynamic environments prone for sampling of noble gases. These can be found on a large variety of fluids and rock samples. Fumarolic gas discharges, hydrothermal springs, groundwaters, and natural gases are noble gas-rich media, as well as submarine glasses and various minerals which can be crushed or melted in vacuo to release their trapped volatiles dissolved in the magma at depth.

2.2.1. Helium, Argon and Neon - Light noble gases in subduction-related volcanism

The distinct isotopic composition of noble gases in the atmosphere and mantle has long been interpreted to indicate their ineffective transfer to the mantle during subduction. For instance, Staudacher and Allègre (1988) estimated that ~96% Ar is removed during subduction in order to maintain mantle isotopic differences relative to air. However, total extraction of noble gases from the slab is unlikely, and a portion (although small) of noble gases may be delivered to the mantle during subduction. Several important observations also suggest that noble gases are subducted beyond depths of arc magma genesis and into the mantle, and measurements of exhumed portions of oceanic and continental lithosphere show that hydrated sections of the oceanic slab, as well as terrigenous lithologies, have a capacity to host significant quantities of seawater-derived noble gases (Porcelli and Wasserburg, 1995a; Baldwin and Das, 2015; Chavrit et al., 2016; Dai et al., 2016; Guo et al., 2017; Honda et al., 2012; Hopp et al., 2016; Kendrick et al., 2013, 2015, 2011; Moreira et al., 2003; Staudacher and Allègre, 1988; Holland, 2006).

Due to distinct compositions and discrepancies in isotopic abundances, the lower and upper part of the mantle have long been considered two separated layers within the deep reservoir (e.g., Kurz et al., 1982; O'Nions and Oxburgh, 1983; Allegre et al., 1983, 1986 and 1987; Kaneoka and Takaoka, 1985; Poreda and Farley, 1992; Hiyagon et al., 1992; Matsuda and Marty, 1995). The lower mantle region appears to be a source of primordial, unfractionated noble gases. For instance, Helium and Neon have being identified in plume materials (Kurz et al., 1983; Rison and Craig, 1983; Honda et al., 1991, 1993; Hiyagon et al., 1992; Richard et al., 1996), whereas the upper part of the mantle, as sampled by Mid-Ocean Ridge Basalts (hereafter referred to as MORB), contributes radiogenic isotopes, such as radiogenic-^{4}He to primordial rare gases transferred from the lower mantle (Allegre et al., 1986, 1987; Kellogg and Wasserburg, 1990; O'Nions and Tolstikhin, 1994; Porcelli and Wasserburg, 1995a, b). Therefore, MOR-type He may be carried by the magma from the mantle to the surface. One of the first discoveries of elevated terrestrial ^{3}He/^{4}He ratios was in fact from a subduction zone setting in the volcanic and hot spring gases in the Southern Kurile Islands (Mamyrin et al. 1969). Since then extensive research of He isotopes in hydrothermal gases has been carried out in subduction zones. In the cases of neon and argon, however, reported isotope results invariably reflect varying degrees of air contamination as a consequence of both the low intrinsic concentrations of these volatiles in natural samples and their greater abundance (relative to helium) in air. Therefore, more significance could be given to the extreme (higher) values as they represent samples least affected by air contamination.

2.2.2. Helium and Carbon systematics of arc gases

Carbon dioxide is one of the major components of high-temperature volcanic gases and volcanic-derived, intermediate to low-temperature surface discharges on Earth. The origin of the carbon has been discussed based on the isotopic compositions of free gases since the 1950's (Craig, 1953; Hulston and McCave, 1962). However, this approach has proved incapable of estimating the magmatic fraction of carbon, since the mixing of organic sedimentary carbon and oceanic limestone carbon may produce a ^{13}C/^{12}C ratio identical to that of MORB-type CO_2 (Hoefs, 1980).

Sano and Marty (1995) have suggested that it is possible to distinguish the carbon fractions of the upper mantle, organic sediment and limestone (including slab components) in CO_2 of volcanic and hydrothermal fluids from subduction zones based on the $^{13}C/^{12}C$ ratios and $CO_2/_3He$ ratios. Higher sedimentary fluxes to the volcanic arc segment of Nicaragua, on the other hand, showed by He-CO_2 relationships consistent with an enhanced input of slab-derived C to magma sources beneath the arc (Shaw, et al., 2003) may be explained by either off scraping of the uppermost sediments in the Costa Rica forearc and/or a cooler thermal regime in the Nicaragua subduction zone, preserving a higher proportion of melt-inducing fluids to subarc depths, leading to a higher degree of sediment transfer to the subarc mantle. In any case, secular variations of the $^{12}C/^{13}C$ ratios and $CO_2/^3He$ ratios may provide useful information on the relation between origin of the carbon and volcanic activity.

2.3. Recent advances in volcanic gas measurements

Recent technological advances in volcanic gas instrumentation have allowed significant improvements to global datasets of volcanic gas compositions and volatile fluxes. Today, easy-to-transport instruments allows for a much more rigorous and continuous recording of the volcanic degassing phenomena, thus providing insightful information on magma degassing and risk assessment associated with volcanic eruptions. This increase in volcanic gas information for different volcanic arc settings has also allowed to correlate geochemical patterns of compositions and fluxes to the role of subducted sediments in arc magmatism and crust–mantle recycling, as well as models of continental growth, continental composition, convergent margin magmatism and mantle heterogeneity that also require a better understanding of the mass and chemical fluxes associated with subducting sediments. An overview of relevant instrumentation for this project is given below, and specific analytical and on-the-field procedures are described in later chapters.

2.3.1. Volcanic gas composition measurements

The MultiGAS (Aiuppa et al., 2005; Shinohara, 2005) is an in-situ gas sensing instrument consisting of a series of electrochemical and nondispersive infrared sensors. Each sensor produces an electrical current in response to the presence of specific target gases, which is proportional to the concentration of the target gas in the total gas volume, allowing retrieval of the composition of the volcanic plume. The instrument allows measurement of most major elements in volcanic emissions: H_2O, CO_2, CO, SO_2, H_2S and H_2 (Aiuppa et al. 2009, 2010, 2012 and references therein). A MultiGAS-type instrument was used exhaustively during this PhD, and more details on calibration gases, measurement results and data processing are provided in the following chapters.

Although data was not included in this dissertation, Open-path Fourier Transform Infrared (FTIR; Oppenheimer et al., 1998) spectrometers were used to measure the composition of volcanic plumes, capturing most major gas species (H_2O, CO_2, SO_2, CO, HCl, HF and OCS). The technique uses infrared radiation produced by the volcano itself, such as that emitted by lava or hot vents at the surface and measures the absorption of a broad range of species in the infrared spectrum. This

technique is by far the most accurate available to measure volcanic gas composition and its 1Hz acquisition allows transient events such as eruptions, to be recorded. The weight (30 kg) and fragility of the system, together with its reliance on a close and strong infrared source (>700°C for a ~400 m range) limits its application to a few volcanic systems.

The use of filter packs (Finnegan et al.,1989) for sampling of gaseous species such as fluorine, chlorine and total sulfur was also attempted, however, without much success especially due to the need to perform distant measurements at highly active volcanoes. However, this system has proven to be efficient for measurements of SO_2, H_2S, HCl, HF in plumes, by pumping volcanic gas through a series of filters pre-treated with an alkaline solution that traps acid gases (SO_2, H_2S, HCl, HF). Subsequent laboratory analysis of the filters allows gas ratios to be determined. In addition, aerosols and ash particles trapped on the filter can be analyzed (e.g., Crowe et al., 1987 and references therein). Figure 2.2 shows an example of simultaneous MultiGAS and filter pack downwind gas collection on the slopes of Nevado del Ruiz (Colombia) in July 2018.

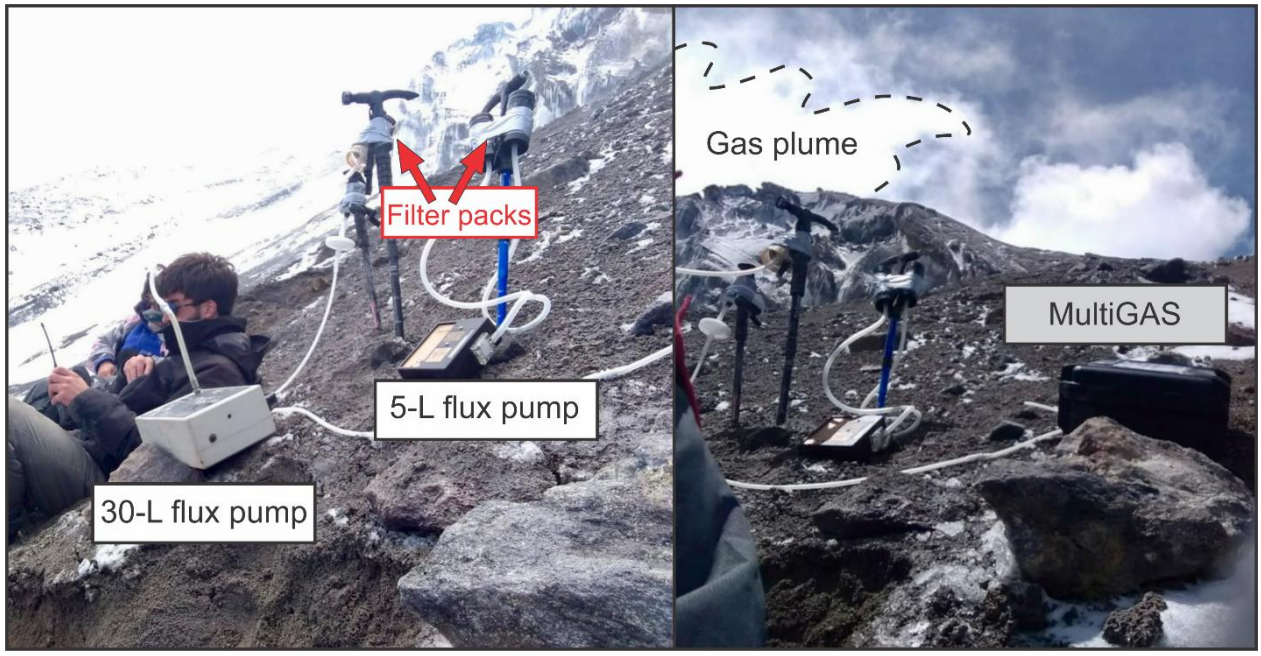

Figure 2.2: Downwind filter pack (5-L and 30-L flux pumps) and MultiGAS data collection at Nevado del Ruiz (SW flank, 5000 m a.s.l.). The 30-Litter flux pump setup included 3 filter packs and 1 PTFE filter for particles.

2.3.2. Thermal Infrared surveys

Infrared cameras were also used to map thermal features, such as crater walls and fumarolic fields. Determining the temperature of various vents is an essential parameter to interpret volcanic gas composition and processes of gas scrubbing (especially Sulfur) happening along the volcanic conduit. Such data can be difficult to acquire directly when access to fumaroles and vents cannot be undertaken safely. Infrared cameras permit remote (few hundred meters) measurement of vents temperatures. In addition, the high (50 Hz) acquisition rate allow observation of the gas output dynamics, especially valuable during explosive activity. Figure 2.3 shows thermal imaging

acquired from the old lava dome from Guagua Pichincha, Ecuador, during the *Trail by Fire* (www.trailbyfire.org) campaign in February 2017.

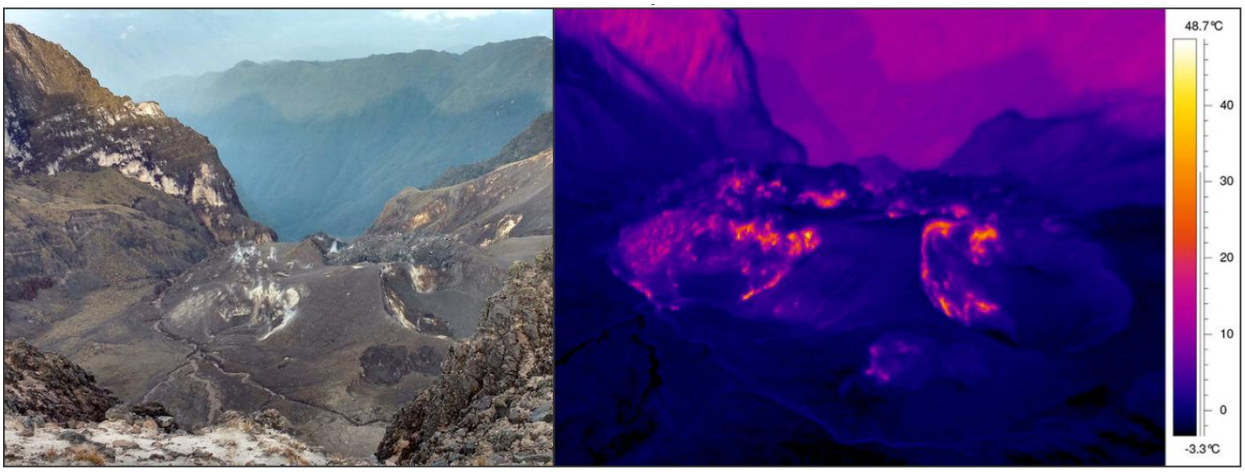

Figure 2.3: Thermal Infrared imaging of the old Guagua Pichincha lava dome (Ecuador). Images were acquired using a FLIR camera.

2.3.3. Volcanic gas fluxes

Oscillations in Sulfur dioxide (SO_2) emission rates have long been a key parameter of volcano monitoring. Research into constraining subaerial volatile fluxes has focused on SO_2 because of its strong UV absorption features, low background atmospheric concentrations (<1 ppb) and relatively high abundance in volcanic plumes (>1 ppm; Galle et al., 2003 and references therein). Correlation spectrometers were the standard instruments used to measure volcanic SO_2 fluxes from volcanoes. These instruments were first developed in the 1960s to measure pollution emitted from industrial and chemical plants (as SO_2 and NO_2), but their utility for volcanic flux measurements was recognized shortly thereafter. The COSPEC (Moffat and Millan 1971; Stoiber et al., 1984), was first used at Mt. Mihara volcano, Japan, in April 1971. Today, COSPEC measurements remain the basis for the majority of global volcanic volatile flux estimates (Hilton et al., 2002) and provide the most extensive data set regarding volcanic gas fluxes (Andres and Kasgnoc, 1998).

Most recently, ultraviolet spectrometers and cameras are used to measure the flux of sulfur dioxide (SO2) emitted by volcanoes. In contrast to the COSPEC, which works on a small range of the UV spectrum via an internal mechanical correlation procedure (Millán, 1980), the less expensive USB spectrometers (e.g. USB2000, USB4000, Avaspec) acquire an entire UV spectrum, which can be subsequently processed using a differential optical absorption retrieval technique to derive SO_2 column amounts (McGonigle et al.,2002; Galle et al., 2003; Mori and Burton, 2006). Using backscattered solar light as the ultraviolet source, these instruments measure the absorption caused by SO_2 in the volcanic plume at specific wavelengths in the ultraviolet spectra. The amount of "missing light" is then used to determine the amount of SO_2 in the volcanic plume. By imaging the entire plume, its speed can then be determined and use to compute the total flux of SO_2 emitted by a volcano at a 1Hz acquisition frequency (Kantzas et al., 2010; Tamburello et al., 2002; and

references therein). Measurements are typically performed at a 2-km distance from the plume. SO_2 flux measurements and data processing are reported and discussed in more detailed in later chapters of this dissertation.

Satellites have been used to measure eruptive SO_2 emissions for several decades (e.g., Carn et al., 2016), but quantification of passive volcanic degassing is relatively recent and concurrent with the advent of sufficiently sensitive space-borne instruments, such as OMI (Carn et al., 2017). These UV spectroscopic measurements and infrared (e.g., IASI-A and IASI-B onboard MetOp) spaceborne sensors have the potential to deliver snapshots of the dispersed SO_2 emitted by a volcano every 12 or 24 hours. Despite limitations to plume capture, especially for low-altitude volcanoes, it is important to refer that satellite observations from remotely, inaccessible volcanoes have allowed the scientific community to identify previously unknown, strongly degassing, SO_2 sources and to improve significantly the constrains of global inventories not only of SO_2, but also, CO_2 (Aiuppa et al., 2019).

2.3.4. Unmanned aerial vehicles (UAV)

Possibly the most innovative and empowering advance in volcanic gas geochemistry measurements in the use of unmanned aerial vehicles (UAV) able to carry ultraviolet spectrometers for SO_2 flux measurements, MultiGAS instruments for plume composition (H_2O, CO_2, SO_2, H_2S and H_2), infrared cameras for temperature measurements, and bag collector systems to aimed at sampling and storing gas for later characterization of plume isotopic composition (especially $\delta^{13}C$). As described in the following chapter, most of this project developed in areas of high altitude, which still represents a challenge for this type of vehicles in terms of flight turbulence, stability and operating capacity via remote controls.

2.4. Combining SO_2 flux measurements with in-situ composition estimates

Carbon dioxide (CO_2) flux estimates are crucial to constrain the role of volcanic subaerial emissions to current atmospheric CO_2 levels, and to quantify CO_2 outputs from active volcanism all around the globe. This has become increasingly possible with technological advances in volcanic gas instrumentation described previously in this chapter. The combination of SO_2 fluxes and in-situ volcanic gas compositions (Aiuppa et al., 2006 and references therein) has allowed estimation of total volatile output (H_2O, CO_2, SO_2, H_2S, H_2, and others; Fischer, 2008) from subaerial emissions for several arc volcanoes.

2.4.1. Unmeasured volcanoes

Global inventories of volatile emissions have suffered from important data gaps in the literature, mostly due to the inaccessibility or high level of volcanic activity at some volcanoes for ground-based SO_2 measurements and in-situ MultiGAS measurements. Estimates from Hilton et al. (2002) were significantly improved upon in Burton et al. (2013) and Aiuppa (2015) as a result of improving data quality and, especially, data density.

However, to this day, the number of ground-based investigations and global volatile outputs estimates remain significantly biased towards volcanoes that are easily accessible and for which data has been collected exhaustively over the years (e.g., Mount Etna, Italy). Significant data gaps were covered in recent years (e.g., Bani et al., 2012 in Vanuatu; Tamburello et al., 2014 and 2015 in Chile; Lopez et al. 2017 at the Aleutians;), but others, such as the Northern Marianas, still persist.

Furthermore, as discussed previously, SO_2 emissions detected from space, combined with have also allowed improvement of CO_2 flux constrains for roughly ~62% of the 91 strongest volcanic SO_2 sources globally (Aiuppa et a., 2019).

2.5. Long- and short-term volcanic gas compositional variations as precursors of volcanic unrest

The recent advances in instrumental monitoring of volcanic gas compositions described previously in this chapter have significantly improved our ability to track pre-eruptive degassing of magmas, and therefore to interpret and predict transition from quiescence to unrest, that can ultimately culminate in volcanic eruptions (e.g., Edmonds, 2008; Oppenheimer et al., 2014; Fischer and Chiodini, 2015; Aiuppa et al., 2017). These studies have greatly focused on the interpretation of volcanic CO_2/SO_2 ratios, which, in light of the contrasting solubility properties of the two volatiles (Papale, 1999; Moretti and Ottonello, 2005), is considered to be a key parameter of magma degassing.

The MultiGAS plays a central role in geochemical monitoring of gas emissions at active volcanoes and has enabled systematic measurements of volcanic CO_2/SO_2 gas ratios and to establish high temporal resolution time series of volcanic gas compositions. Therefore, it provides the opportunity to capture the passive degassing of CO_2-rich gas prior to eruption of mafic arc volcanoes (e.g., Aiuppa et al., 2007). High temporal resolution gas measurements initially focused on Italian volcanoes, where the first permanent MultiGAS networks were installed (Aiuppa et al., 2009, 2010a, 2010b), and where a peculiar CO_2-rich magmatism (Métrich et al., 2004; Kamenetsky et al., 2007) makes the relative abundance of CO_2/SO_2 in the magmatic gas phase a particularly suitable monitoring parameter. However, this method has proved valuable for a range of magmatic contexts, including CO_2-poor volcanoes (Aiuppa et al., 2017) such as Redoubt (Aleutians, Werner et al., 2013), Bezymianny (Kamchatka, Lopez et al., 2013), Turrialba (Costa Rica, de Moor et al., 2016) and Villarrica (Chile, Aiuppa et al., 2017).

Given the remarkable compositional dissimilarity between magma-derived gas and hydrothermal gases, gas monitoring can potentially provide invaluable insights into the processes causing unrest (e.g., Giggenbach et al., 1990; Vaselli et al., 2010; Chiodini et al., 2015; de Moor et al., 2016; Aiuppa et al., 2017). However, continuous long-term instrumental records of gas compositional variations at the quiescence-to phreatic- to magmatic transition are essentially absent in the geological literature.

2.6. Noble gas sampling and advances in analytical techniques

Due to the acidic nature of high-temperature fumarolic gases, attempts of sampling dry gases during this investigation were conducted using stainless steel bottles and 12ml vials. Furthermore, Helium permeation through pyrex has been experimentally determined by several researchers in the in 1950s–1960s (Altemose 1961; Norton 1953; Rogers et al.1954) and is discussed in detailed, for example, by Fischer and Sano (2012). References of sampling procedure of high-temperature fumarolic gases and specific approach here used are described in later chapters. Although data is not included in this dissertation, sampling of hydrothermal areas for noble gases were also conducted during this investigation, mostly to provide knowledge to local observatories of the isotope characteristics (noble gases and carbon) of peripheral emissions. Some of the sampling sites included bubbling waters near Tungurahua (Ecuador), Purace (figure 2.4) and Nevado del Ruiz (Colombia).

Figure 2.4: Sampling of dry gases from bubbling springs at San Juan de Purace (Colombia)

CHAPTER 3

The Northern Volcanic Zone of the Andean Volcanic Belt

The Andes consist of the largest orogenic belt system formed by subduction of oceanic crust along an active continental margin. It includes ~200 potentially active Quaternary volcanoes, occurring in four separate segments defined as the Northern, Central, Southern and Austral Volcanic Zones (Fig. 3.1). Volcanism results from subduction of the Nazca plate, for the largest portion of the arc, and the Antarctic oceanic plates (at the southern-most part of the volcanic arc) below South America. Here, as well as in other volcanic arcs, geochemical evidences in Andean magmas of dehydration and/or melting of subducting oceanic lithosphere and interaction of these slab-derived fluids/melts with the overlying mantle wedge (Thorpe, 1984), prove the intimate relationship between active volcanism at the surface and subduction dynamics along the arc. In fact, active volcanism occurs in regions characterized by a relatively steep (>25°) subduction angle, normalized to relatively flat (<10°) geometries in areas separating the most active portions of the Andes (Stern, 2004).

3.1. Andean magmatism

Andean magmatism started by dehydration of the subducted oceanic lithosphere resulting in the addition of subducted components into the melt of the overlying mantle wedge, as described above. Along-arc distinctions in magma genesis and isotope characteristics are, however, notorious, especially in areas characterized by significantly dissimilar crustal thicknesses. For instance, it has been argued that low $^{3}He/^{4}He$ ratios in the Andes indicate (upper) crustal additions to the volatile budget (Hilton et al. 1993a), and that crustal contamination may play a major role on measured $^{3}He/^{4}He$ along the Andes (Hilton et al., 2002). For example, the volcanic front of the Central SVZ of the Andes (~30 km of crustal thickness) is generally characterized by tholeiitic and high-Al basalts (Hickey-Vargas et al., 1984), that yield isotope and trace-element ratios similar to oceanic island arc basalts, which implies little-to-no assimilation of continental crust, as suggested in Hickey-Vargas et al. (1986, 1989). Differences in isotopic composition of volcanic rocks from the Northern SVZ and CVZ of the Andes compared with those erupted in the Central SVZ and oceanic island arcs also indicate the participation of continental crust and/or subcontinental mantle lithosphere in the formation and evolution of the NSVZ and CVZ Andean magmas. This may occur during interaction of magmas derived in the subarc asthenospheric mantle wedge with continental lithosphere (Rogers and Hawkesworth, 1989; Stern et al., 1990; Stern and Kilian, 1996; Hickey et al., 2002), by intra-crustal assimilation (James, 1984; Hildreth and Moorbath, 1988; Davidson et al., 1991), and/or by source region contamination of subarc mantle by subducted continental components (Stern et al., 1984b; Stern, 1988, 1991a; Stern and Skewes, 1995). The next chapters aim to discuss and provide further evidence of crustal controls in fluids chemistry measured at volcanic centers along the trench.

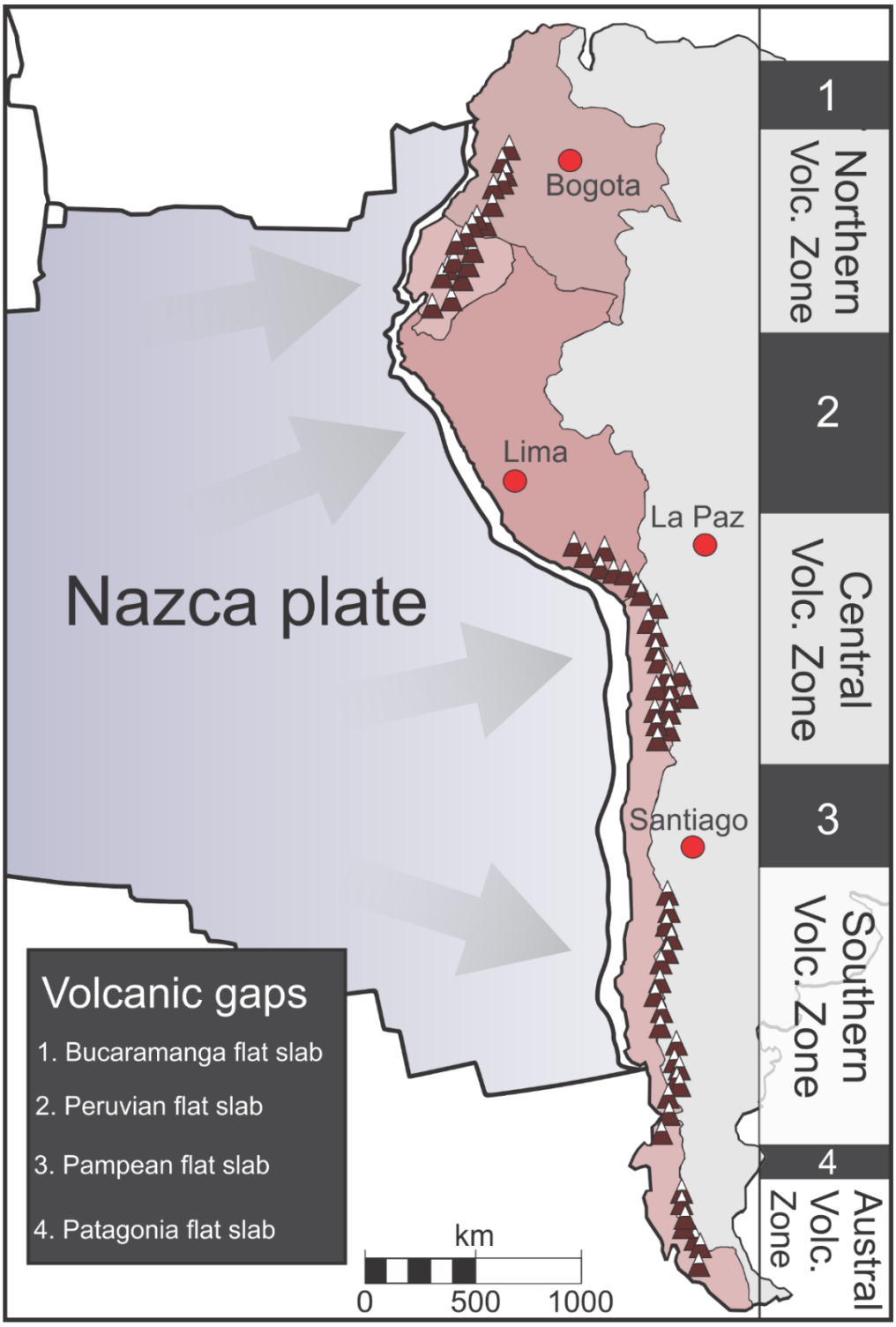

Figure 3.1: Subduction geometry and along-arc distribution of Andean volcanic centers. Flat slab information is from Stern (2004).

3.2. Subduction geometry along the Andean active margin

The crust below the CVZ in the Central Andes is >70 km thick below both the western Cordillera Occidental and the eastern Cordillera Oriental flanking the Altiplano and Puna plateaus, and 60-65 km thick below the Altiplano and Puna (James, 1971; Schmitz, 1994; Beck et al., 1996; Dorbath et al., 1996; Schmitz et al., 1999; Swenson et al., 2000; ANCORP Working Group, 2003). This very thick crust underlies a region 700 km long and 200 km wide which has an average elevation >3,700 m, while many peaks in these two cordilleras reach >6,000 m. Crustal thickness decreases rapidly to the east of the Cordillera Oriental, to 43-47 km below the Subandean zone and 32-38 below the Chaco plain further to the east (Beck et al., 1996). Crustal thickness also decreases gradually to the north, to 65 km at the northern end of CVZ (15°S) and to 40-45 below northern Perú (7°S). Further north, below the NVZ in Ecuador and Colombia the crust is 40-60 km thick below both the western Cordillera Occidental and eastern Cordillera Real and Central (Feininger and Seguin, 1983). Crustal thickness also decreases to the south of the Puna plateau to >55 km below both the Sierras Pampeanas ranges (Jordan et al., 1983; Kay et al., 1999) and the Main Cordillera at the northern end of the SVZ (33°S) in the Southern Andes, 40 km at 39°S (Lüth and Wigger, 2004) and ultimately 30-35 km south of 37°S below the central and southern SVZ and AVZ (Lowrie and Hey, 1981).

The very thick crust below the Central Andes may be due to crustal shortening (Isacks, 1988; Beck et al., 1996; Allmendinger et al., 1997; Kley et al., 1999), magmatic underplating (Tosdal et al., 1984; Schmitz et al., 1997), a combination of the two, with more crustal shortening in the eastern Cordillera Oriental and more magmatic underplating and lithospheric hydration below the western Cordillera Occidental (James, 1971; James and Sacks, 1999; Giese et al., 1999; Victor et al., 2004), or lithospheric delamination (Kay et al., 1994, 1999). Crustal thickening and uplift in the northern Central Andes began during the Eocene as a result of an episode of very rapid oblique convergence (Pardo-Casa and Molnar, 1987), and continued episodically to generate the thick crust below the Central Andes (Mpodozis et al., 1995; Kay et al., 1999; Jaillard et al., 2000). The timing and style of deformation, uplift and magmatism varied from one region of the Central Andes to another (James and Sacks, 1999; Kay et al., 1999). While the Altiplano (James and Sacks, 1999) and northern Puna (Kay et al., 1999) plateaus began to evolve as subduction angle increased after the Eocene event, the Main Andean Cordillera of the Pampean flat-slab segment began to be uplifted as subduction angle decreased (Jordan et al., 1983; Cornejo et al., 1993; Kay et al., 1999; Kay and Mpodozis, 2002; Ramos et al., 2002).

This appears reflected on along-arc signatures of magmas erupted at the Andes. Crustal components are most significant in magmas erupted in the Central Volcanic Zone, where the crust is extremely thick (>70 km) and estimated rates of subduction erosion of the continental, possibly equivalent to as much as 4% of the volume of subducting oceanic crust, are also greatest due to the hyper-arid climate conditions and low sediment supply to the trench.

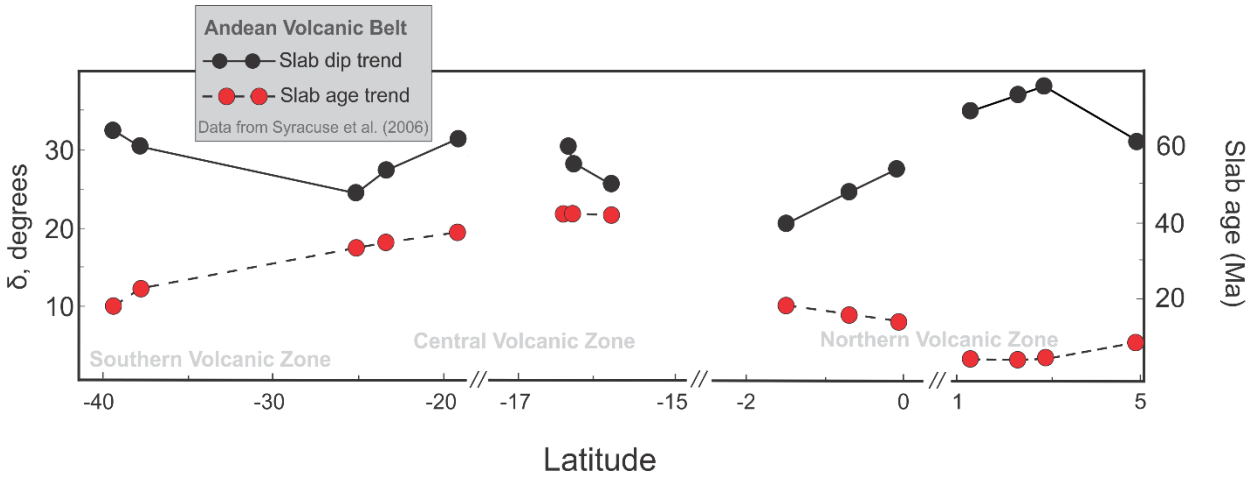

Figure 3.2: Along-arc variation of slab age (in degrees) and Subducting slab age (in Ma). Data is from Syracuse et al. (2006).

3.3. Volatile budget estimates for Andean volcanoes

3.3.1. A view of Andean Volcanism from Space: Subaerial SO_2 emissions from the Ozone Monitoring Instrument

The first volcanic SO_2 emissions inventory derived from global, coincident satellite measurements, made by the Ozone Monitoring Instrument (OMI) on NASA's Aura satellite between 2005 and 2015 was reported by Carn et al. (2017). For the SO_2 inventory sources were identified based on 3-year averages of OMI data for 2005–2007, 2008–2010 and 2011–2014, then annual emissions were calculated for each source for the entire 11-year period studied (2005–2015; Carn et al., 2017). Andean volcanoes are particularly suitable for satellite detections of volcanic degassing, due to the high altitude of volcanic edifices along the arc (some near the 6000 m a.s.l.). In their entire dataset, Carn et al. (2017) highlight 91 main sources of SO_2 for the 10-year period referred. Out of the 91 volcanoes, 11 are distributed between the four main volcanic regions of the Andes. At the Northern-most part of the arc Nevado del Ruiz is estimated to have emitted an average 1074 ± 1376 t d^{-1} of SO_2, which between 2005-2015 ranks the volcano 14th overall in the list of most persistently degassing volcanoes on Earth. Furthermore, what is perhaps even more relevant to our investigation is the fact that by 2015 (the last year analyzed) the same volcano had jumped to 5th place overall in SO_2 emissions. Other persistent emitters in the NVZ include Nevado del Huila whose 627 ± 665 t d^{-1} of SO_2 mostly reflect lava dome emplacement late in the year 2008 and continuous lava extrusion between November 2008 and November 2009, when volcanic gas plumes were frequently observed by webcameras from *INGEOMINAS.* Also, in the Colombian segment of the NVZ, Galeras emitted 218 ± 317 t d^{-1} (2005-2015), which is comparably lower to values of ~450 t d^{-1} previously reported in the literature (Zapata et a., 1997). Southwards along the arc, Tungurahua and Reventador (Ecuador, NVZ) have recorded SO_2 fluxes of 342 ± 235 and 206 ± 187, respectively. As for the Peruvian segment, located in the CVZ, Ubinas and Sabancaya emitted 222 ± 252 and 87± 158, respectively. In the Chilean-Argentinian arc segment Copahue

(342 ± 235), Lastarria (248 ± 62), Isluga (78 ± 107) and Villarrica (281 ± 160) registered the highest SO_2 emissions rates. Figure 3.3 shows the along-arc variation in emissions between 2005-2015 recorded by OMI and reported by Carn et al. (2017).

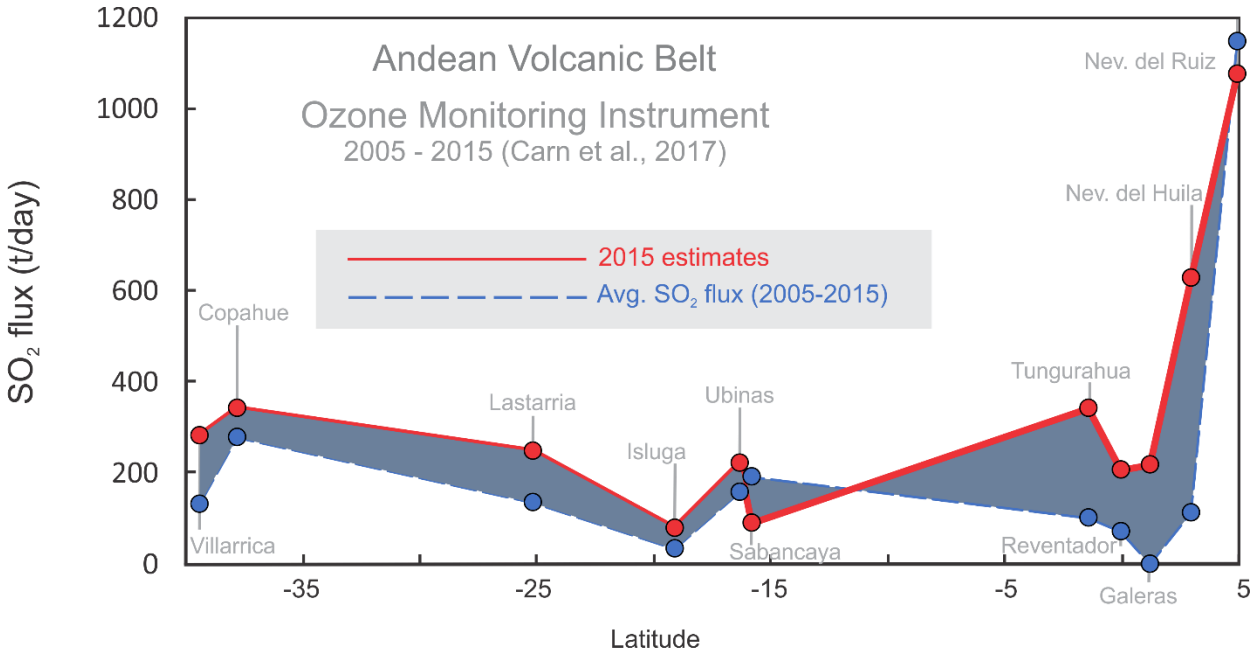

Figure 3.3: SO_2 flux emissions detected by the Ozone Monitoring Instrument (OMI) between 2005 and 2015. Blue circles and dashed line represent the 10-year SO_2 flux average, whereas red dots and red line symbolize SO_2 flux estimates from space for Andean volcanoes in 2015.

3.3.2. Recent ground-based constrains on subaerial SO_2 degassing

For the period between 1989 and 1995 exhaustive COSPEC SO_2 flux measurements reported by Zapata et al. (1997) for Galeras yield SO_2 fluxes generally in excess of 700 t d^{-1} prior to explosive episodes, which reportedly decreased after eruptive events. The highest fluxes measured from at this volcano in that period reached values as high as 3000-5000 t d^{-1} and an average flux of about 450 t d^{-1} was reported for the same period (Zapata et al., 1997; Andres and Kasgnoc, 1998). However, using recently developed UV scanners (DOAS) and portable UV cameras the number of investigations into quantifying volcanic SO_2 emissions suing ground-based instruments has significantly increased. Although altitude here may in fact be an obstacle, due to dense cloud coverage at higher altitudes, examples of successful measurements at Andean volcanoes include Moussallam et al. (2017), that estimated an SO_2 flux of 2313 ± 529 t d^{-1} for Sabancaya and Ubinas together, and Tamburello et al. (2014), who's total SO_2 flux output estimates for five Chilean volcanoes (Putana, Lastarria, Láscar, Ollagüe and San Pedro) were reported at 1818 t d^{-1}.

3.3.3. Volcanic gas compositions and CO_2 budget of Andean Volcanoes

Over the last 10 years, the development of gas sensing instrumentation more easily transported to high altitude volcanoes translated into what today is considered a comprehensive dataset of volcanic gas compositions for a big portion of the Andes volcanoes. Ecuador is perhaps the most

noticeable exception. As described in the previous chapter, Aiuppa et al. (2017) used the combination CO_2/S_T vs. Ba/La in Ecuadorian lavas to cover that gap.

In the Andes, there is documented evidence in the literature for large along-arc variations in volcanic rock trace-element and isotope geochemistry. Available whole-rock data based on the subpopulation of Andean volcanoes shows an overall south-to-north increase in trace-element slab-fluid proxies (Ba/La, Sr/Nd and U/Th), which is discussed in more detail in later chapters of this dissertation. Aiuppa et al. (2017) also argued that the along-arc variations in the volcanic gas CO_2/S_T ratio scale well with the trace-element variation patterns, therefore suggesting common source processes. Figure 3.4 summarizes the CO_2/S_T along-arc trend reported in the literature through the first stages of this PhD and corresponding CO_2 flux estimates for the main arc emitters along the Andean Volcanic Belt.

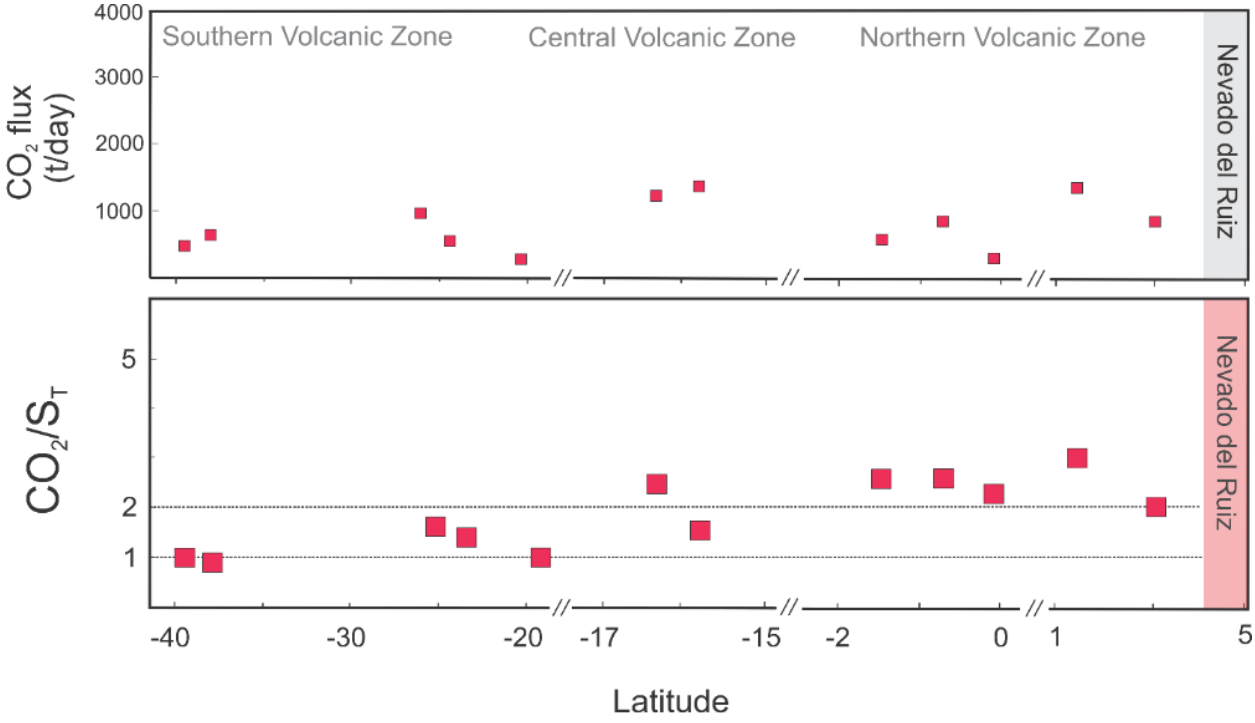

Figure 3.4: Along-arc CO_2/S_T trend and CO_2 flux estimates for the main arc gas emitters in the Andean Volcanic Belt. This dataset and data provenance are discussed in detail in the next chapter.

3.4. Noble gas isotope variability along the Andes

The lack of noble gas data in the Andes is evident and limits the interpretation of existing datasets in terms of constraining the role of crust, slab and mantle in the isotope signature of these magmatic fluids. Arguably this is mostly due to the heterogeneity of sampling media and the different conditions free gases can be found at areas of active volcanic activity. Figure 3.5 demonstrates how C and helium may be affected by different temperature conditions and the existing variability in current datasets.

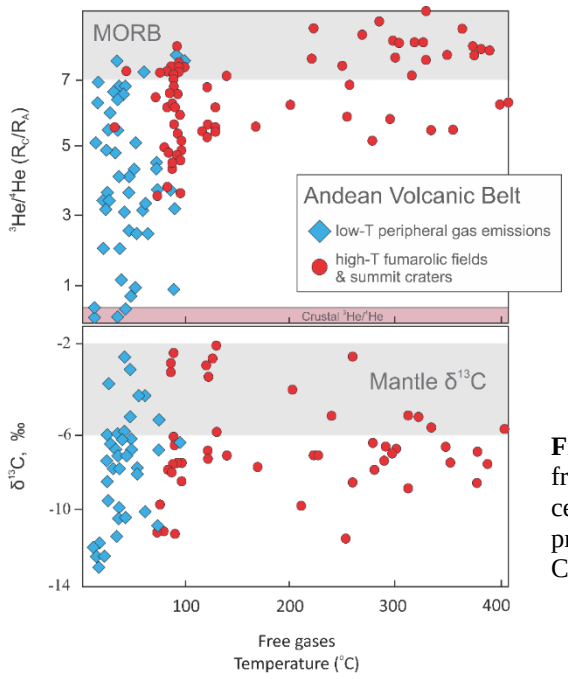

Figure 3.5: $^{3}He/^{4}He$ and $\delta^{13}C$ vs temperature of free gases collected over time at volcanic centers along the Andes. This dataset and data provenance are discussed in more detail in Chapter 6 of this dissertation.

However, within the Northern Volcanic Zone of the Andes, Colombia and Ecuador contrast in the amount of data available. Both Nevado del Ruiz and Galeras were extensively studied during the last 15 years of the 20th century. Williams et al. (1987) and Sano et al. (1990) reported on a wide range of gas emissions at Nevado del Ruiz, from steam vents to crater fumaroles. Curiously, the authors reported the highest $^{3}He/^{4}He$ (6.6 R_A) on an acid-sulfate river source, about 0.3 R_A units higher than the fumarolic isotope signature of Arenas crater. Carbon isotope systematics of several low-temperature peripheral gas discharges were contemporarily investigated by Sturchio et al. (1988), that reported $\delta^{13}C$ ranging from -8.9 to -14.6 (‰). On the other hand, the majority of samples available for the Ecuadorian segment are from low-temperature gas sources, especially due to high levels of risk associated with on-going activity, difficult-to-access fumarolic fields, or even lack of surface gas manifestations, such as the case of Tungurahua, even at periods preceding volcanic unrest. Figure 3.6 shows the Northern Volcanic Zone trend in Helium isotope signatures.

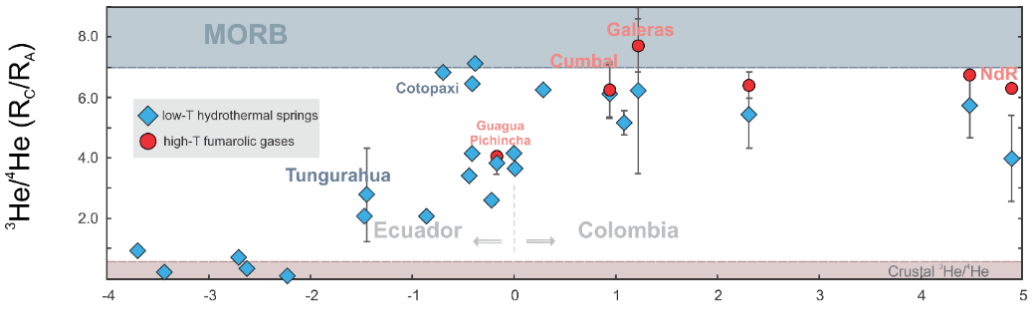

Figure 3.6: $^{3}He/^{4}He$ variations along the Northern Volcanic Zone of the Andean Volcanic Belt. A detailed discussion on this dataset, as well as data provenance, are provided in Chapter 6 of this dissertation.

CHAPTER 4

Volcanic Gas Emissions Along the Colombian Arc Segment of the Northern Volcanic Zone (CAS-NVZ): Implications for volcano monitoring and volatile budget of the Andean Volcanic Belt

Published as: Lages, J., Chacón, Z., Burbano, V., Meza, L., Arellano, S., Liuzzo, M., Giudice, G., Aiuppa, A., Bitetto, M., López, C. (2019). Volcanic gas emissions along the Colombian Arc Segment of the Northern Volcanic Zone (CAS-NVZ): Implications for volcano monitoring and volatile budget of the Andean Volcanic Belt. Geochemistry, Geophysics, Geosystems, 20. https://doi.org/10.1029/2019GC008573

Abstract. Studying spatial and temporal trends in volcanic gas compositions and fluxes is crucial both to volcano monitoring and to constrain the origin and recycling efficiency of volatiles at active convergent margins. New volcanic gas compositions and volatile fluxes are here reported for Nevado del Ruiz, Galeras, and Purace, three of the most persistently degassing volcanoes located in the Colombian Arc Segment of the Northern Volcanic Zone. At Nevado del Ruiz, from 2014 to 2017, plume emissions showed an average molar CO_2/S_T ratio of 3.9 ± 1.6 (S_T is total sulfur, S). Contemporary, fumarolic chemistry at Galeras progressively shifted toward low-temperature, S-depleted fumarolic gas discharges with an average CO_2/S_T ratio in excess of 10 (6.0–46.0, 2014–2017). This shift in volcanic gas compositions was accompanied by a concurrent decrease in SO_2 emissions, confirmed on 21 March 2017 by high-resolution ultraviolet camera-based SO2fluxes of ~2.5 kg/s (~213 t/day). For comparison, SO_2 emissions remained high at Nevado del Ruiz (weighted average of 8 kg/s) between 2014 and 2017, while Puracé maintained rather low emission levels (<1 kg/s of SO_2, $CO_2/SO_2 \approx 14$). We here estimate carbon dioxide fluxes for Nevado del Ruiz, Galeras, and Puracé of ~23, 30, and 1 kg/s, respectively. These, combined with recent CO_2 flux estimates for Nevado del Huila of ~10 kg/s (~860 t/day), imply that this arc segment contributes about 50% to the total subaerial CO_2 budget of the Andean Volcanic Belt. Furthermore, our work highlights the northward increase in carbon-rich sediment input into the mantle wedge via slab fluids and melts that is reflected in magmatic CO_2/S_T values far higher than those reported for Southern Volcanic Zone and Central Volcanic Zone volcanoes. We estimate that about 20% (~1.3 Mt C/year) of the C being subducted (~6.19 Mt C/year) gets resurfaced through subaerial volcanic gas emissions in Colombia (Nevado del Ruiz ~0.7 Mt C/year). As global volcanic volatile fluxes continue to be quantified and refined, the contribution from this arc segment should not be underestimated.

4.1. Introduction

Carbon (C)- and sulfur (S)-containing molecules are, after water, the two most abundant magmatic volatiles in silicate melts (Wallace et al., 2015). The exchange of these volatiles between the Earth's crust and mantle occurs primarily along subduction zones, where volatile recycling at

subducted slabs results into volatile-rich magmas that degas carbon dioxide (CO_2) and sulfur dioxide (SO_2) to the atmosphere through active arc volcanoes (Aiuppa, Fischer, et al., 2017). Quantifying the arc-resolved (e.g., Hilton et al., 2002) and global arc (see a review in Burton and Sawyer, 2013) magmatic volatile fluxes is thus key to better understanding volatile cycling in and out of the planet and consequently planetary evolution over geological time (Dasgupta, 2013; Keleman and Manning, 2015).

Unfortunately, however, while the global volcanic arc S budget is relatively well characterized (e.g., Shinohara, 2013), estimates of the global arc volcanic CO_2 flux span 1 order of magnitude or more (Marty and Tolstikhin, 1998; Fischer, 2008; Burton and Sawyer, 2013; Shinohara, 2013). In contrast to SO_2, which is scarcely present in air and effectively absorbs ultraviolet (UV) radiation (e.g., Edmonds et al., 2003; Mori and Burton, 2006; Kantzas and McGonigle, 2008; Kern et al., 2013; Carn et al., 2017), high background concentration in the atmosphere, and the presence of several absorption interferences in the infrared, complicates volcanic CO_2 remote sensing from both ground (Aiuppa et al., 2015; Queißer et al., 2018) and space (Schwandner et al., 2017). Therefore, volcanic CO_2 flux estimates are typically derived indirectly by combining measurements of SO_2 flux and of CO_2/SO_2 ratios in volcanic gases (e.g., Aiuppa et al., 2006; Shinohara et al., 2008). The latter measurements require in situ gas observations in hazardous and/or difficult to access volcanic craters, which have so far proven to be impossible for several volcano targets worldwide (Aiuppa et al., 2019), making the CO_2 budget inaccurately known for several arc segments (Shinohara, 2013), and globally (Aiuppa et al., 2019).

Here we aim at refining our current understanding of volcanic arc CO_2 budgets, by presenting novel volcanic gas information (both compositions and fluxes) for the Colombian Arc Segment (CAS). The CAS hosts 20 Holocene volcanoes (Fig. 4.1), many of which currently show evidence of volcanic activity at the surface. While previous work has been made to characterize volatile emissions at some of these volcanoes, including Galeras (e.g., Fischer et al., 1997) and Puracé (e.g., Sturchio et al., 1993), no high-temperature volcanic gas compositions have yet been reported for Nevado de Ruiz, the most actively degassing volcano in the Andean Volcanic Belt (2005–2015; Carn et al., 2017). We here present the first volcanic gas plume results for this volcano from which, by integration with novel data for Galeras and Puracé, we derive, for the first time, the volatile (CO_2) budget for the most persistently volcanic gas emitters along the CAS. Our novel results also open the way to a better characterization of the along-arc volcanic gas compositional trends in South America and thus to shed new light on the complex origin and recycling processes of volatiles at convergent margins (Aiuppa, Fischer, et al., 2017). Moreover, our volcanic gas results will help to establish baselines for key volcanic gas-related monitoring parameters (e.g., CO_2/SO_2 ratios; Aiuppa et al., 2017), which is critical to accurately interpret variations in geochemical precursors that may precede periods of volcanic unrest. This is especially important for volcanoes such as Galeras and Nevado del Ruiz, which in recent times have caused tremendous destruction and devastation of neighboring communities in Colombia (e.g., Voight, 1990; Voight et al., 2016).

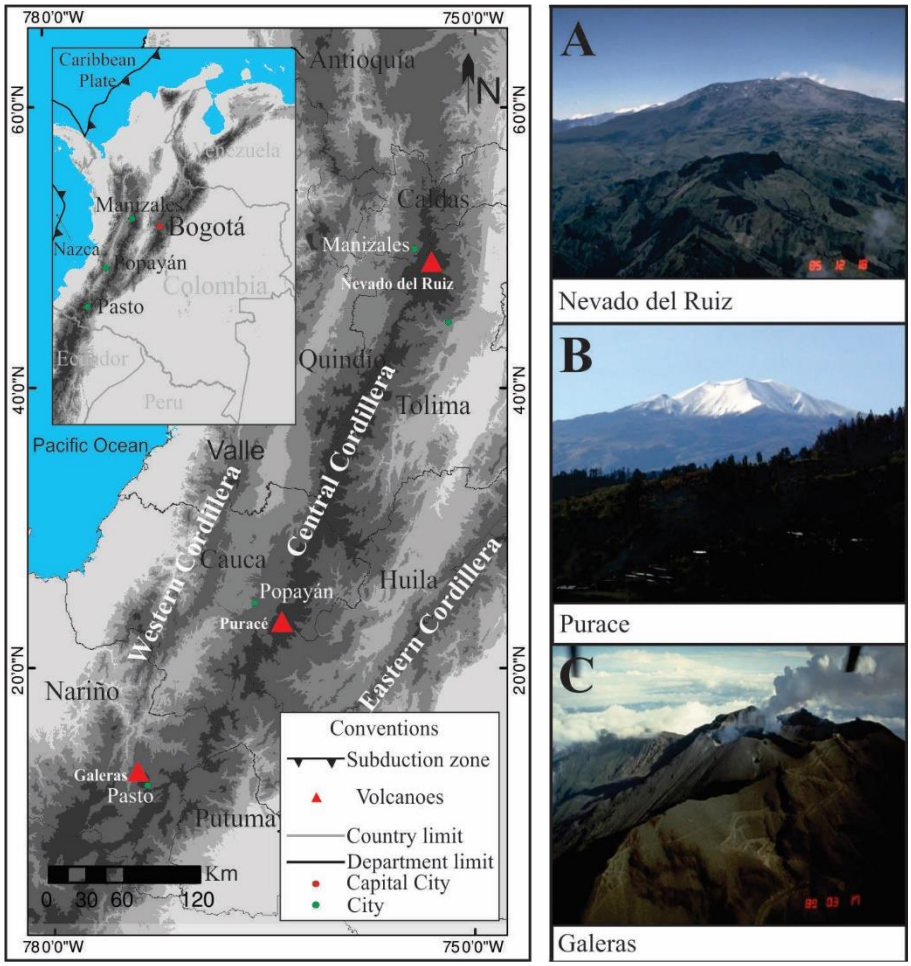

Figure 4.1: Map showing the location of Galeras, Puracé, and Nevado del Ruiz along the Central Cordillera of the Andes. (a) Nevado del Ruiz volcano; (b) Puracé volcano; and (c) Galeras (all photos from the Global Volcanism Program, 2013a, 2013b, 2013c).

4.1.1 The Colombia Arc Segment

The morphologically continuous mountain chain of the Andes persists for over 7,000 km along the western margin of South America. Volcanism here occurs in four separate regions, the Northern (NVZ), Central (CVZ), Southern, and Austral Volcanic Zones. The Colombia Arc Segment (CAS) is part of the Holocene NVZ of the Andes, which results from subduction of the 12–20 Ma Nazca Plate (slab age from Jarrard, 1986) beneath the South American Plate. This section of the volcanic arc, with an extension of approximately 530 km, hosts 20 active volcanoes located along the Central Cordillera, the highest of the three branches of the Colombian Andes (Fig. 4.1). Twelve of them are currently classified with unrest level IV, including Puracé, in a scale for which I is accredited to on-course or eminent eruptions. Nevado del Ruiz and Galeras are classified with level III of volcanic activity, attributed to volcanoes that show frequent change on monitoring parameters of volcanic activity (Boletines Informativos, Servicio Geológico Colombiano (n.d.); https://www2.sgc.gov.co/volcanes).

Here we report new compositional and flux data from three of the main volatile emitters in the CAS, Puracé, Nevado del Ruiz, and Galeras (Fig. 4.1). The last two are part of the DECADE initiative (https://deepcarboncycle.org/home-decade) that aims to improve estimates of global fluxes of volcanic CO_2 to the atmosphere. Nevado del Ruiz and Galeras have been identified as two of the 91 strongest volcanic SO_2 degassing in the period 2005–2015 (Carn et al., 2017). Based on satellite measurements made by the Ozone Monitoring Instrument (OMI), Carn et al. (2017) estimated the time-averaged (2005–2015) SO_2 flux for Nevado del Ruiz at 1,074 ± 1,376 t/day, making it the largest SO_2 emitter in the NVZ (Colombia and Ecuador). Over the same decade, Galeras emitted on average 218 ± 317 t/day of SO_2 (Carn et al., 2017), about half of the registered flux for this volcano prior to 2005 (450 t/day; Zapata et al., 1997; Andres and Kasgnoc, 1998).

4.2. Eruptive history and recent volcanic activity

4.2.1. Nevado del Ruiz

Nevado del Ruiz (4.892°N, 75.324°W; 5,279 m a.s.l.) is an andesitic stratovolcano located in the department of Caldas, central Colombia, near the northern end of the NVZ. Its first major eruptive period initiated 1.8 Ma ago, followed by a second eruptive stage that lasted approximately 0.6 Ma, from 0.8 to 0.2 Ma ago (Thouret et al., 1990). A summit caldera, formed around the end of the second eruptive period, has now been filled by numerous composite lava domes that characterize the present-day NdR. The modern edifice consists of a truncated cone built by lava flows propagating toward the northeastern, west-northwestern, and east-southeastern flanks. The volcano displays a glacier-covered summit surrounding the 1-km-wide, 240-m-deep Arenas crater. Over the past 11 ka, Nevado del Ruiz has explosively erupted andesitic to dacitic magmas, for a total of 12 identified eruptive stages. On 13 November 1985, a short-lived eruptive pulse of a Volcanic Explosivity Index (VEI) of 3 caused the melting of the summit ice cap and generated a sequence of deadly lahars that killed approximately 25,000 people (Hall, 1990). Explosive events associated with the currently active Arenas crater included other small occurrences nonetheless capable of creating debris avalanches, pyroclastic flows, and surges such as the ones recorded on 19 February 1845 (Thouret et al., 1990). Previous work done on the magmatic-hydrothermal system of Nevado del Ruiz (Arango et al., 1970; Giggenbach et al., 1990; Sturchio et al., 1988) suggests a strong gas-water interplay beneath the Arenas crater, with continuous release of heat and gas to the hydrothermal system by the intrusion and subsequent crystallization of magmas emplaced during the last period of major effusive activity several hundred thousand years ago (Thouret et al., 1985). These sporadic injections of high-temperature magmatic fluids from depth are thought to trigger recurrent periods of seismic unrests at Nevado del Ruiz, with plumes of water vapor and volcanic gas reaching heights up to ~700 m above the Arenas crater that continue to be reported today by the local volcano observatory in Manizales.

4.2.2. Galeras

Galeras (1.221°N, 77.359°W; 4,276 m a.s.l.) is the youngest active cone of the Galeras Volcanic Complex. It is located ~60 km north of the Colombia-Ecuador border, in the department of Nariño.

Over the past 1 Ma this complex has been characterized by caldera-forming eruptions, followed by the construction of active cones that produced lavas and pyroclastic flows, ranging from basaltic andesites to dacites (Calvache and Williams, 1997a, 1997b). The present-day active cone lies in the uppermost part of the sector collapse depression that occurred between 12 and 5 ka ago, during the Urcunina stage (the last eruptive stage before the formation of the present active center at the Galeras Volcanic Complex; Calvache et al., 1997a,b). It rises 150 m above the caldera floor and presents four different craters. The reactivation of the system in 1988 followed one of the four longest repose periods (1948–1988) in the last four centuries. Prior to that, most eruptive episodes, in particular those that took place in the beginning of the twentieth century (e.g., 27 August 1936), exhibited similar eruptive features, producing vertical eruptive columns, ash fall, and small pyroclastic flows (about 3–4 km long; Calvache, 1990). The reactivation of the volcanic system in 1988 was marked by increasing gas emissions and number of earthquakes. Until 1993, the volcano was almost continuously active, with a series of explosive eruptions recorded in May 1989, high levels of degassing and seismicity between 1989 and 1991, and andesitic dome emplacement between September and November 1991, which was destroyed in a series of vulcanian explosions during 1992–1993 (Stix et al., 1997). These last events are believed to have been caused by continuous pressurization of the main conduit as a result of small amounts of crystallization and cooling happening at shallow depths (Stix et al., 1993, 1997), a similar process to that described by Giggenbach et al. (1990) for Nevado del Ruiz. The same conduit dynamics are thought to be responsible for the most recent eruptive events, such as those that occurred between 2008 and 2010 (VEI 3) and more recently in January 2014 (VEI 2). Present-day gas discharges and summit activity differ from those observed in the 1990s, when degassing was concentrated in the Deformes and Besolima fumaroles, with temperatures between 200 and 500 °C (Sano et al., 1997 and Sano and Williams, 1996). Today, three main fumarolic emissions, Paisita, Chavas, and the central crater, are the main degassing sources at the closed-vent Galeras system. The temperature of the fumaroles was not directly measured due to inaccessibility to the vent areas, but visual inspection and nature of sublimates in the fumaroles' surroundings suggest near-boiling temperatures.

4.2.3. Puracé

Puracé (2.314°N, 76.395°W; 4,630 m a.s.l.) is a dacitic shield volcano, capped by an andesitic cone of lavas and pyroclastic deposits (Monsalve and Pulgarín, 1993), located in the department of Cauca, SW Colombia. It is the most active center in the Coconucos Volcanic Chain, a chain that comprises 15 volcanic features along a system of longitudinal and transversal regional faults, having erupted at least 12 times this century (Sturchio et al., 1988). Eruptions such as the last one recorded in the year of 1977 have produced andesitic lavas, pyroclastic flows, and surges, as well as lahars (Monsalve, 1996; Monsalve and Pulgarín, 1993). Currently, weak fumarolic activity is observed at the bottom of the main crater, whereas the main source of degassing is a fumarolic field on the outer northwest volcano's flank of temperatures as high as 135 °C.

4.3. Materials and Methods

Data reported in this study result from field campaigns in Colombia between 2014 and 2017. In situ fumarolic gas composition was first measured at Paisita (Galeras) on 17 October 2014, four days before the first plume measurements at Nevado del Ruiz were acquired. With support from the local observatory of Pasto (SGC-OVSP) regular MultiGAS (Multi-component Gas Analysis System; Aiuppa et al., 2005, Shinohara, 2005) surveys in Paisita took place between February and July 2016. In March 2017, volcanic gas compositions were obtained for all three volcanoes here investigated, including Puracé and two additional fumarolic sources at Galeras (Chavas and the central crater). Finally, in July 2017, volcanic gas surveys were repeated in Galeras and Nevado del Ruiz. From then until 20 December 2017, a permanent MultiGAS station deployed at Nevado del Ruiz recorded daily volcanic gas composition data.

4.3.1. In Situ Volcanic Gas Measurements

We used a set of MultiGAS units to measure the in-plume concentrations of the major volcanic volatiles at the three Colombian volcanoes. Each instrument was composed of a Gascard nondispersive infrared CO_2 spectrometer from Edinburgh Sensors (accuracy, ±1.5%; calibration range of 0–3,000 ppm) and City Tech SO_2, H_2S, and H_2 electrochemical sensors with calibration ranges of 0–200, 0–100, and 0–50 ppm, respectively (repeatability, 1%). The system also included temperature (T) and relative humidity (Rh) KVM3/5 Galltec-Mela sensors. All system components and respective power sources were contained within a weather-resistant plastic case, with inlet/outlet ports to provide access to ambient air. Gas sensors were calibrated prior and following each measurement campaign at the Earth and Marine Sciences Department (DiSTeM, University of Palermo) with standard gas mixtures for CO_2 of 300 and 3,000 ppmmol (effective concentrations of 293.7 and 2,920 ppmmol, respectively), for SO_2 of 100 ppmmol (effective concentration 102.7 ppmmol), for H_2S of 40 ppmmol (38.0 ppmmol) and for H_2 of 10 ppmmol (10.0 ppmmol). In the field, volcanic gas was pumped through the in-series connected sensors, using a small pump with a flow rate of 1.8 L/min, and in-plume gas concentrations measured at a frequency of 1 Hz. Each measurement was preceded by instrument warm-up (3 min) and 2 min of ambient air flow to flush residual volcanic gas that remained trapped within the circuit.

At Nevado del Ruiz, all measurement surveys of volcanic gas composition, from 2014 and 2017, were performed at, and around, Bruma (4.90°N, −75.34°W; 4,832 m a.s.l.), a site located in the middle of a flank canyon carved by previous volcanic activity. Due to its geomorphology, the canyon channels the main vent plume downwind, over the NW flank of the edifice. Despite persistent gas emissions from the central crater, complex weather conditions (e.g., sudden shifts in wind direction) made plume capture very intermittent and compositions were obtained from rare patches of wind-blown volcanic gas. In June 2017, the gas unit was permanently installed in Bruma, approximately 2 km away from the main vent and configured to collect measurements of volcanic gas at 1 Hz in cycles of 30-min duration, separated by intervals of 6 hr (four cycles per day).

At both Galeras and Puracé, discrete MultiGAS measurements were made at close proximity to the main summit fumarolic sources. At Galeras, the volcanic gas compositional data we report on were acquired during walking traverses in and around two sparse fumarolic gas emissions (Paisita and Chavas) and at the central crater. Today the main crater of Puracé shows no evidence of persistent degassing, and measurements at this volcano were made at the fumarola lateral, currently the most vigorous source of volcanic gases to the atmosphere.

MultiGAS data were analyzed by selecting specific acquisition windows that showed good temporal correlation between the concentrations of volatiles species measured simultaneously (e.g., Aiuppa et al., 2014; Tamburello et al., 2015). Given the pressure difference between calibration (P = 1,013 mbar) and measurement (P = 577–610 mbar) site, manufacturer pressure corrections (0.015% signal per hPa for SO2 and 0.008% signal per hPa for H2S) were estimated at ≤0.2% effect on the calculated x/SO2 ratios across our data set. Therefore, such trivial variances have not been considered, and all ratios reported are uncorrected. CO2 readings were automatically pressure compensated by the nondispersive infrared spectrometer. Cross-sensitivity effects of SO2 on the H_2S sensor were estimated at 14.5% during calibration, and corrections were applied during data processing to calculate interference-corrected H_2S concentrations in the gas plume. A scatter plot of the CO_2 versus SO_2 concentrations (in ppmv) is shown in Figure 4.2a, where the corresponding averaged CO_2/SO_2 ratio in that temporal interval is calculated from the slope of the best fit regression line (dashed blue line). The same procedure was applied to calculate in-plume relative abundances of other volatile species such as H2S/SO2 and H2O/CO2. CO2 and H_2O concentration ratios were estimated after subtraction of background-air concentration ratios acquired at plume-free areas. H_2O concentration ratios were calculated using measurements of T, P, and Rh and the Arden Buck equation (Tamburello, 2015). For each fit window, the peak SO2 concentration was used to trace the intensity of the gas plume and is here considered as an analog of measurement quality. Reported composition averages (e.g., x/SO_2 and mol%) are, therefore, based on predetermined weights assigned to each MultiGAS measurement by the maximum amount of SO_2 recorded by the instrument for a given acquisition window.

4.3.2. UV Camera Measurements

We used a dual UV camera system (Tamburello, Kantzas, McGonigle, Aiuppa, and Gaetano, 2011) for survey-type SO2 flux measurements at Nevado del Ruiz and Galeras. The system consisted of two co-aligned cameras used simultaneously to measure incident radiation through filters centered at 310 (effective SO2 absorption region) and 330 nm (outside of the absorption range). Observations at both volcanoes were conducted between 7 and 9 a.m. (GMT −5; period with the lowest cloud coverage) at distances of 2.2 and 2.5 km for Nevado del Ruiz and 0.5 km for Galeras. Measurement sites were selected so as to grant a clear view of the gas plume, with blue sky in the background and the volcanic edifice framed within the acquisition window. The JAI CM-140 GE-UV dual-set UV cameras are fitted with a Sony ICX407BLA UV-enhanced CCD array sensor (10 bit, 1,392 × 1,040 pixels) and equipped with an electronic shutter architecture and GiGE Vision interface. Two quartz lenses (UKA optics UV1228CM, focal length 12 mm)

provided a horizontal field of view of ~37°, while the two band-pass filters (Edmund 310nm CWL and 330nm CWL, 10-nm full width at high maximum) were placed between the lenses and the charge-coupled device array to avoid variations in wavelength response (Kern et al., 2013). Before acquisition, the UV camera system was calibrated using three calibration cells of known SO2 concentrations (203, 998, and 1,861, ppm m), which allowed the calibration of the qualitative measured apparent absorbance (Kantzas et al., 2010; Lübcke et al., 2012). The system was powered by a 12-V lithium battery. With this setup, sequential images of the plume were captured at ~0.5-Hz rate. For image acquisition and processing we used Vulcamera, a stand-alone code specifically designed for measuring SO2 fluxes using UV cameras (Tamburello, Kantzas, McGonigle, and Aiuppa, 2011). Cross correlation of two integrated column amounts time series (obtained along two closely spaced parallel sections, perpendicular to the plume) and absorbance for each camera pixel were calculated using the methodology of Kantzas et al. (2010; integrated in the Vulcamera software) and used to finally derive plume speed.

4.3.3. NOVAC Measurements

For Nevado del Ruiz and Galeras, in addition to our survey-type UV camera results, we also used the systematic SO2 flux records obtained by the local network of UV scanning spectrometers of NOVAC, the global Network for Observation of Volcanic and Atmospheric Change (Galle et al., 2003, 2010). At Nevado del Ruiz, data from five NOVAC scanning mini-differential optical absorption spectroscopy (DOAS; Johansson et al., 2009) instruments were combined with meteorological information to derive daily statistics of total SO2 emissions. The use of five scanners allows effective plume capturing for virtually any plume transport direction. At both Galeras and Puracé, one scanning unit was available, and data from these instruments are considered below.

Each plume scan is composed of 51 radiance spectra taken across the scanning plane at steps of 3.6°. Flat and conical scan modes were used. The first comprises a scan performed from horizon to horizon along a vertical surface passing zenith, whereas for the conical scanner, with an opening angle of 60°, a more efficient scan geometry is obtained, providing results under larger deviation in wind direction. Each scan sequence starts with optimization of the exposure time for a spectrum taken in the position closest to zenith (limited to 1,000 ms). This exposure time is kept constant for all measurements in the same scan. Usually, 15 spectra are averaged at each position to improve the signal-to-noise ratio. An additional dark-current/offset spectrum is measured on each scan, with the fore-optics facing the shadowed nadir position of the scanner. Data are saved in situ and then transmitted to the observatory for real-time evaluation. For SO_2 calculations, the plume speed is obtained from the ECMWF/ERA-Interim database (Dee et al., 2011), whereas plume direction and altitude is obtained by triangulation of consecutive scan measurements. Daily averages are estimated by simply calculating the arithmetic mean of all valid scans recorded on a single day. The uncertainties reported (1σ of the daily mean) have been factored in the weighted SO_2 flux yearly average (2014–2017 for Galeras and Nevado del Ruiz), in order to give more relevance to days for which data were acquired more consistently.

Detailed information on retrieval of relative SO_2 slant column densities, SO_2 vertical column densities, SO_2 flux and plume parameters, statistics, and uncertainties associated with each measurement (including uncertainties related to wind speed retrievals from the ECMWF-ERA5 meteorological model) are provided as supporting information Text S1.

4.4. Results

4.4.1. Gas Composition

4.4.1.1. Nevado del Ruiz

At Nevado del Ruiz, due to high volcanic activity levels recorded throughout this investigation, proximal crater areas have remained inaccessible, thus hampering near-vent in-plume observations. Our measurements at Bruma are thus representative of a distal, aged 215- to 590-s plume, depending on highly variable wind speed (daily average estimates ranging from 3.5 to 9.5 m/s) plume. Due to temporal variations in plume transport direction and speed, the plume was variably diluted while our measurement point was fumigated, so that atmospheric dilution upon transport is responsible for the large variations in gas concentrations detected by the MultiGAS. Sulfur dioxide concentrations spanned from <1 to ~15 ppm, while background air-corrected CO_2 concentrations varied from <1 to ~50 ppm (Figure 4.2a). Magmatic H_2O was more episodically detected above the atmospheric backgrounds and ranged from <10 to ~2,950 ppmv. H_2S was rarely detected above the 14.5% cross-sensitivity to SO_2 and showed maximum concentrations of ~0.30 ppmv, while MultiGAS measurements recorded H_2 concentrations up to 5 ppmv.

The derived volatile ratios (in the form of x/SO_2 ratios; where x is H_2O, CO_2, H_2S, or H_2) at Nevado de Ruiz are listed in Table 1a. All x/SO_2 plume ratios were obtained in measurement windows where strong positive covariations ($R^2 > 0.6$) were observed between SO_2 and other volatiles (see example in Fig. 4.2b) and correspond to the gradients of the best fit regression lines in the scatterplots (e.g., Fig. 4.2a). The interference-corrected H_2S/SO_2 ratio and the H_2/SO_2 ratio showed small variations throughout the course of the investigation, with mean values of 0.1 ± 0.005 and 0.2 ± 0.1 (uncertainties correspond to one standard deviation on the average, here and below), while CO_2/SO_2 and H_2O/SO_2 ratios varied more widely, as discussed below.

The derived CO_2/SO_2 molar ratios (Table 1a and Fig.4.2c) are grouped into three different categories depending on the peak SO2 concentration (SO_2 MAX) detected during each measurement interval: (I) SO_2 MAX < 5; (II) $5 \leq SO_2$ MAX < 10; and (III) SO_2 MAX ≥ 10 (in ppm). The more scattered category I CO_2/SO_2 ratio data (Fig. 4.2c, in light gray) potentially reflect either higher analytical uncertainties on the derived volcanic CO_2 concentrations in dilute plume conditions or the presence of other CO_2 sources (in addition to the magmatic plume) and should thus be considered with caution in the analysis of compositional temporal trends (Fig. 4.3b). We thus used the corresponding SO_2 peak concentration (Fig. 4.3a) to estimate the daily CO_2/SO_2 weighted daily means, which were calculated by weighting each compositional measurement by the SO_2 peak concentration recorded during individual acquisition windows, as explained above.

On our explorative surveys of 21 and 22 October 2014, the unit ran for about 2 and 0.5 hr, respectively. Measurements on October 21 yielded CO_2/SO_2 averages of 4.2 ± 3.0 and 2.3 ± 0.1 for Categories II and III data, respectively, resulting in a daily CO_2/SO_2 weighted mean of 2.6 ± 0.5 for that day. On 22 October a more diluted plume signal (SO_2 MAX of 3.8 ppm) recorded an CO_2/SO_2 average of 4.2 ± 3.1. Using the same scatterplot approach (e.g., Fig. 4.2a), H_2S/SO_2, H_2/SO_2, and H_2O/SO_2 ratios were also derived in October 2014, with obtained averages of 0.1, 0.1, and 25.7, respectively. From these compositional measurements in-plume molar proportions of 87.3 mol% H_2O, 8.6 mol% CO_2, 3.4 mol% SO_2, 0.4 mol% H_2S, and 0.3 mol% H_2 were derived in October 2014 for Nevado del Ruiz (Table 1a).

Following the same measurement routine, in March 2017, our unit measured continuously for approximate 3.5 hours in the same location. Sulfur dioxide concentrations exceeded background levels to a maximum of 4.5 ppmv, and very sparse volcanic CO_2 peaks (as high as 889 ppmv) revealed a highly diluted plume (Category I) with an CO_2/SO_2 average of 5.4 ± 5.3, similar to the results obtained in 2014 under similar measurement conditions (Fig. 4.3a and 4.3b). The plume exhibited a more H_2O-rich composition (H2O ~97.9 mol%) than in 2014, and the H_2/SO_2 ratio was also ~5 times higher (0.5 ± 0.2; Tab. 4.1a).

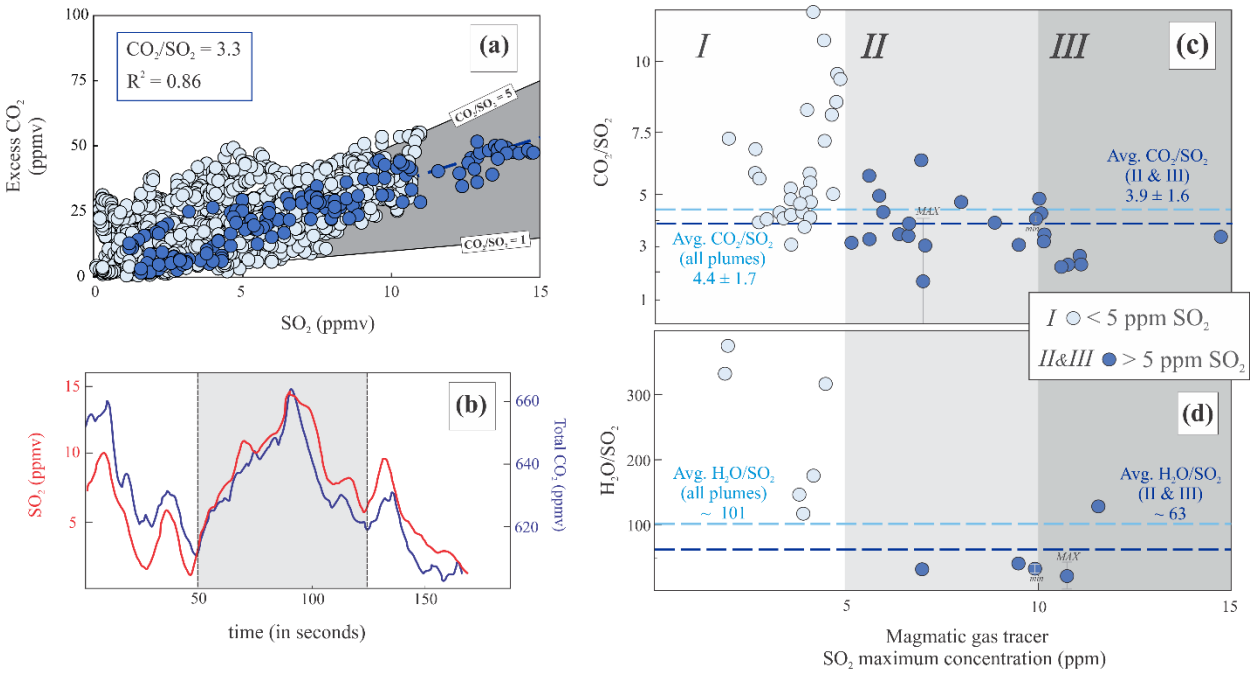

Figure 4.2: (a) Nevado del Ruiz CO_2 versus SO_2 (ppmv) scatterplot showing an example of an acquisition window with all data in light blue and individual data points used to determine the slope of the best fitting linear regression line (dotted dark blue line, $R^2 = 0.86$). Gray area demarks the field of $5 \geq CO_2/SO_2 \geq 1$; (b) Acquisition window showing the concentration time series of SO_2 and excess CO_2 (after atmospheric background subtraction) in ppmv. Gray area corresponds to the time window selected to calculate CO_2/SO_2 ratio shown in (a). (c and d) CO_2/SO_2 and H_2O/SO_2 versus SO_2 maximum concentration (in ppm) shown for all plume categories, from I ($0 < SO_2 < 5$ ppm; light blue data points) to II and III ($5 < SO_2 < 15$ ppm; dark blue data points). To single out the "magmatic" CO_2/SO_2 and H_2O/SO_2 ratios, Category I type plumes were not considered in the average estimates marked by the dark blue dashed line. The average of our entire data set is represented by the light blue dashed line.

In July to December 2017, Category III measurements showed slightly higher CO_2/SO_2 ratios (mean, 3.2 ± 0.1) than in previous observational periods (Fig. 4.3b). Category I and II plumes' CO_2/SO_2 averages remained higher than observed in denser (Category III) plumes, with 5.5 ± 3.2 and 4.3 ± 2.4 averages, respectively (individual CO_2/SO_2 ratios and daily means are shown in the time series of Fig. 4.3). Magmatic H_2O signals, when distinguishable from the atmospheric background, yielded widely variable H_2O/SO_2 ratios (32–377) in July–December 2017, but Category II and III plumes converged to averaged magmatic CO_2/SO_2 and H_2O/SO_2 ratios of 3.9 ± 1.6 and 63 ± 45, respectively (Fig. 4.2d). From the data above, the time-averaged plume composition in 2017 was thus estimated at 91.7 mol% H_2O, 6.0 mol% CO_2, 1.8 mol% SO_2, 0.2 mol% H_2S and 0.2 mol% H_2.

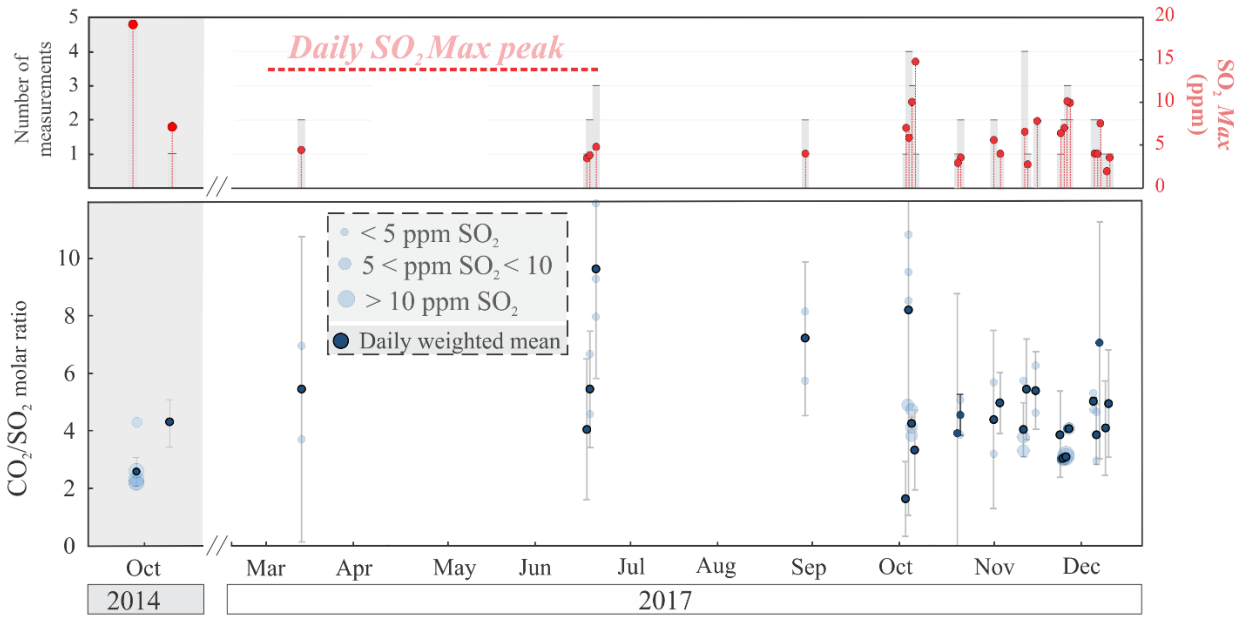

Figure 4.3: (a) Light grey bars indicate the number of compositional measurements used to calculate weighted daily means, while red closed circles represent the maximum SO_2 peak concentration (in ppm) recorded for each day. (b) CO_2/SO_2 time series for Nevado del Ruiz (October 2014 and March–December 2017); light blue bubble sizes are proportional to the maximum SO_2 concentration (in ppm) recorded for any given MultiGAS measurement, while dark blue closed circles symbolize weighted daily CO_2/SO_2 averages.

4.4.1.2. Galeras

Three emission sources, Paisita, Chavas, and the central crater, have been actively degassing at Galeras since 2014. Our results identify large temporal (at each site) and spatial (from one site to another) variations in gas composition (Table 4.1b). All daily CO_2/SO_2 averaged ratios, and associated errors, are shown in the time series of figure 4.4a.

The first MultiGAS survey in October 2014 at Galeras was restricted to the Paisita fumarole only. This yielded a CO_2/SO_2 ratio average of 6.0 ± 1.2 (Figs. 4.4a and 4.4b, in green). Sulfur dioxide was the prevalent S species (H_2S/SO_2 molar ratios of 0.6 ± 0.1), and the H_2O/CO_2 ratio averaged

at ~24, yielding an averaged plume composition of ~74.3 mol% H_2O, 21.0 mol% CO_2, 3.0 mol% SO_2, 1.6 mol% H_2S, and 0.1 mol% H_2.

From February to July 2016, despite the high SO_2 concentrations recorded in the gas plume (as high as 74 ppmv), CO_2/SO_2 molar ratios at Paisita increased to 14.2 ± 1.1 (6-month-period average; Figure 4.4a). This increase was even more pronounced in March 2017, when the CO_2/SO_2 ratio increased at both Paisita (Fig. 4.4b, in olive drab) and the central crater (87.3 ± 17.4 and 93 ± 6.2, respectively; Figure 4a, inset). Conversely, Chavas exhibited lower CO_2/SO_2 of 5.4 ± 0.8, similar to those observed at Paisita in 2014 (Fig. 4.4).

Volcanic gas measurements in July 2017 confirmed a high CO_2/SO_2 ratio signature at all emission sources (Paisita, 38.5 ± 2.7; central crater, 33.6 ± 13.6; Chavas, 41.7 ± 0.9 on 13 July; central crater, 33.6 ± 8.0 on 14 July) as plotted in the inset of Figure 4.4a (Fig. 4.4b shows the scatterplot of CO_2 versus SO_2 in orange for Paisita in July for comparison with previous measurements). High H_2O/SO_2 ratios were also observed at all vents (154.7 ± 2.4, 97.8 ± 0.1, and 264.3 ± 16.0 for Paisita, Chavas, and the central crater, respectively), suggesting a SO_2-poor composition, which is

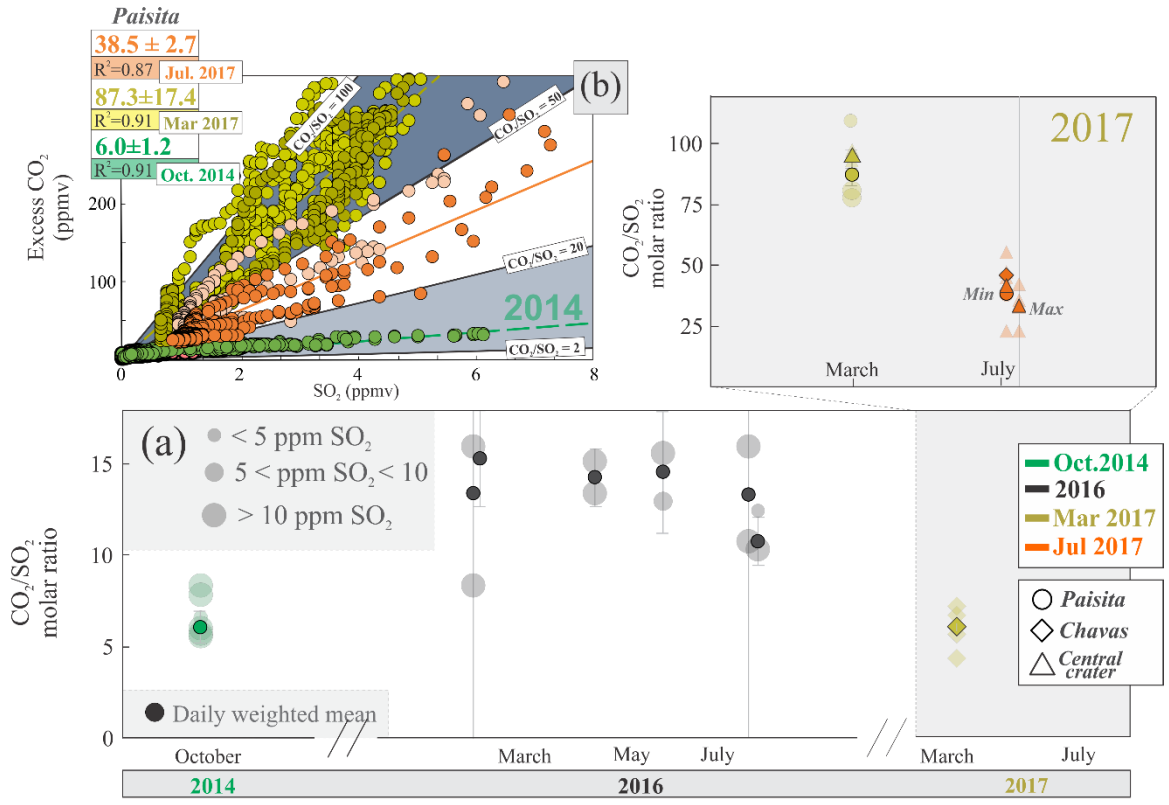

Figure 4.4: Galeras: (a) CO_2/SO_2 time series for Galeras (October 2014, in green; February–July 2016, in dark gray; March 2017, in olive drab; and July 2017, in orange). Light gray area delimitates the 2017 period, with inset from March to July, and shaded red bubble sizes are proportional to the maximum SO_2 amount (in ppm) recorded by each MultiGAS measurement, while dark colors symbolize weighted daily CO_2/SO_2 averages. (b) CO_2 versus SO_2 (ppmv) scatterplots of concentration ratios at Paisita from October 2014 (green), March (olive drab), and July (orange) 2017, with respective least squares regression lines.

also consistent with a sensible increase in the H_2S/SO_2 ratios (0.6 in 2014 to as high as 2.3 in 2017). Based on these ratios, the plume compositions in July 2017 were derived at 74.3 mol% H_2O, 24.5 mol% CO_2, 0.5 mol% SO_2, 0.8 mol% H_2S, and 0.1 mol% H_2 (Paisita); 56.8, 41.8, 0.7, 0.7, and 0.1 (Chavas); and 86.6, 12.6, 0.3, 0.4, and 0.1 (central crater; Table 1b).

4.4.1.3 Puracé

Measurements in the lateral fumarole of Puracé (135 °C) yielded an in-plume CO_2/SO_2 ratio average of 14.0 ± 2.3 during the measurements performed on 23 March 2017 (Table 1c). The H_2O/CO_2 ratio was low (average 10.7 ± 2.8), and the in-plume composition was estimated at 91.3 mol% H_2O, 7.7 mol% CO_2, 0.6 mol% SO_2, 0.3 mol% H_2S, and 0.2 mol% H_2. A few low-temperature peripheral gas emissions were also analyzed, yielding the following gas compositions: (i) Agua Herbiendo (59 °C), 30.1 mol% H_2O, 69.0 mol% CO_2, and 0.9 mol% H_2S; (ii) Poco Azul (85 °C), 50.5 mol% H_2O, 49.0 mol% CO_2, and 0.5 mol% H_2S; and (iii) San Juan de Puracé (34 °C), 89.9 mol% H_2O, 9.1 mol% CO_2, and 1.0 mol% H_2S. These fumaroles are thus enriched in CO_2, as typical of low-temperature gas discharges at the periphery of active volcanoes.

Daily averaged composition estimates and associated errors (±1σ of the daily mean) for Nevado del Ruiz, Galeras, and Purace are reported individually in Tables 1a–1c.

4.4.2. SO_2 Fluxes

On each of our MultiGAS observation days (Fig. 4.3), the Nevado del Ruiz scanning-DOAS NOVAC system was regularly in operation and outputted the daily averaged SO_2 fluxes listed in Table 2a and graphically illustrated in Figure 4.5a. In 2014, for both days of acquired MultiGAS data (21 and 22 October), the SO_2 flux averaged 33 and 13 kg/s, respectively (Table 2a). From March to December 2017, the SO_2 flux ranged between 3 and ~35 kg/s, with an estimated weighted SO_2 flux average of ~8 kg/s (arithmetic mean of ~13 kg/s; see section 3.3 for details on average estimates). For comparison, measurements made on 1 and 4 July 2017 between 7 and 9 a.m. GMT −5 using the dual UV camera system, although restricted to acquisition windows limited to short periods of cloud-free conditions (~6 and ~18 min, respectively), yielded SO_2 fluxes of 21 ± 7 and 11 ± 3 kg/s (Table 2a1). These were higher and more variable than the daily averaged NOVAC-based SO_2 fluxes for the two days (4.0 and 4.4 kg/s for 1 and 4 July, respectively), despite the similar average plume speed estimates used to retrieve SO_2 outputs from both methods (~9.4 m/s for NOVAC and ~8.5 m/s for the UV camera), implying that UV camera observations may have captured short-lived phases of elevated degassing. Still, the averaged SO_2 flux for the two UV camera measurements (~16 kg/s) is well within the range of the NOVAC SO_2 outputs in 2017 (Fig. 4.5).

The SO_2 flux oscillated between ~ 5 and 6 kg/s at Galeras (NOVAC) during our 2014 MultiGAS survey (Table 2b). In 2016 (February to July), the SO_2 flux ranged between 3 and 9 kg/s (average of ~5 kg/s), and, in 2017, no SO_2 was detected from NOVAC, suggesting a drop in SO_2 emissions that is well consistent with our MultiGAS-based compositional data (cf. section 4.1.2). However, the near-vent dual UV camera measurements performed on 21 March were well able to detect the

SO_2 emissions from the volcano and to distinguish the individual SO_2 contributions from Paisita, Chavas, and the central crater (Fig. 4.6). Acquisition windows with clear atmospheric background for all three sources were again restricted in time (11–14 min in temporal intervals between 7 and 8 a.m. GMT −5) but allowed the estimation of weighted SO_2 fluxes of 0.4 ± 0.4 ($<0.1_{[min]}$–$1.29_{[max]}$), 1.3 ± 0.6 ($<0.1_{[min]}$–$2.2_{[max]}$), and 0.8 ± 0.5 ($0.7_{[min]}$–$1.20_{[max]}$) for Paisita, Chavas, and the central crater, respectively (Table 4.2b1). Due to highly variable wind conditions during the acquisition period, our reported weighted means consider only fluxes estimated from plume speed values within 1σ of the mean. Values outside of this range are likely to overestimate SO_2 flux outputs and are uncharacteristic of the overall degassing pattern of all three individual subaerial discharges. The total SO_2 flux was thus 2.5 ± 1.5 kg/s, slightly lower than the 2014–2016 NOVAC records.

On 23 March 2017 the NOVAC scanning DOAS at Puracé derived an SO_2 flux of 0.1 ± 0.1 kg/s (Table 2c). The SO_2 flux remained low throughout the course of this investigation (March to December 2017).

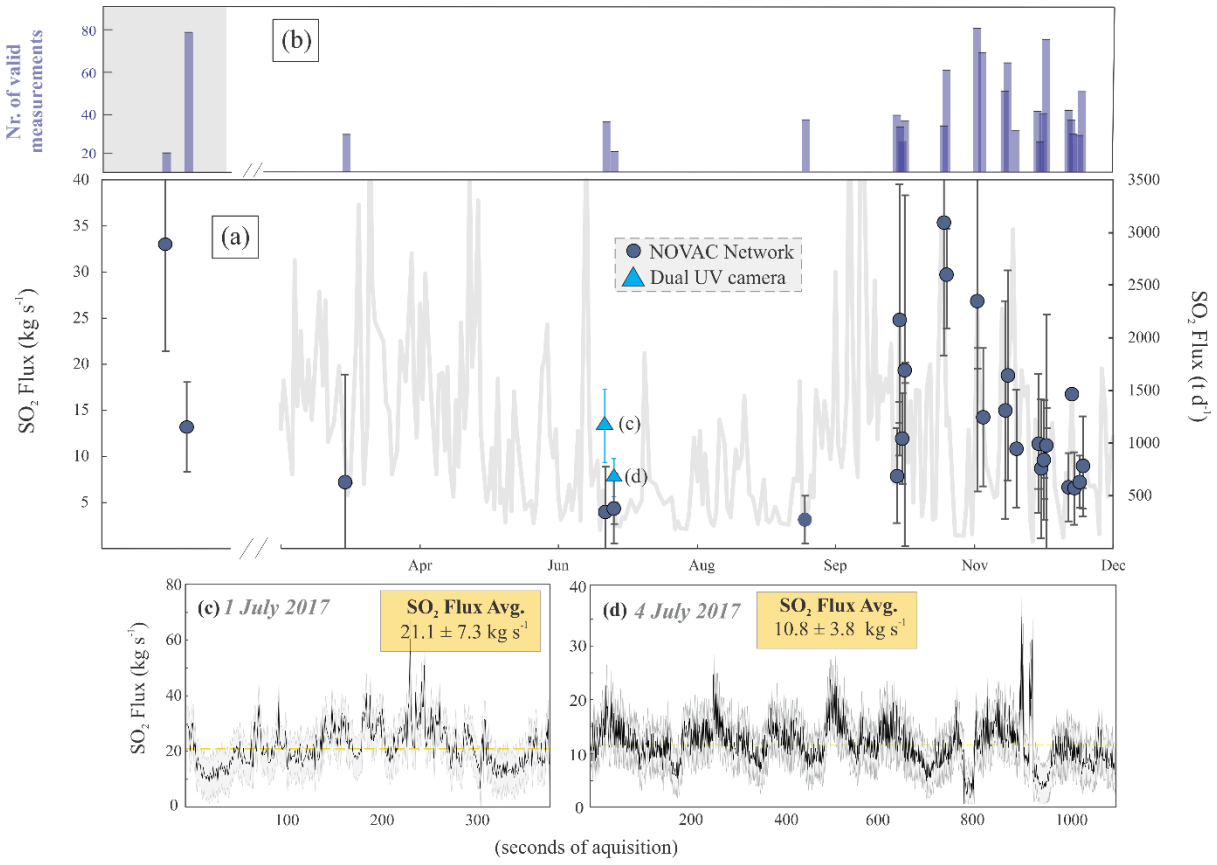

Figure 4.5: Nevado del Ruiz: (a) SO_2 flux (in kg/s and t/day) time series. Closed circles in dark blue represent daily SO_2 flux means to which blue bars in (b) indicate the number of valid measurements used in each daily average estimate; in (a)March–December (2017) SO_2 flux time series is shown in light gray, and measurements obtained using the dual UV camera system on 1 and 4 July 2017 as blue triangles, with respective acquisition time series (in kg/s) show on (c) 1 and (d) 4 July;. Gray area in (c) and (d) represents the estimated SO_2 flux ± 1σ, with acquisition flux average marked in yellow.

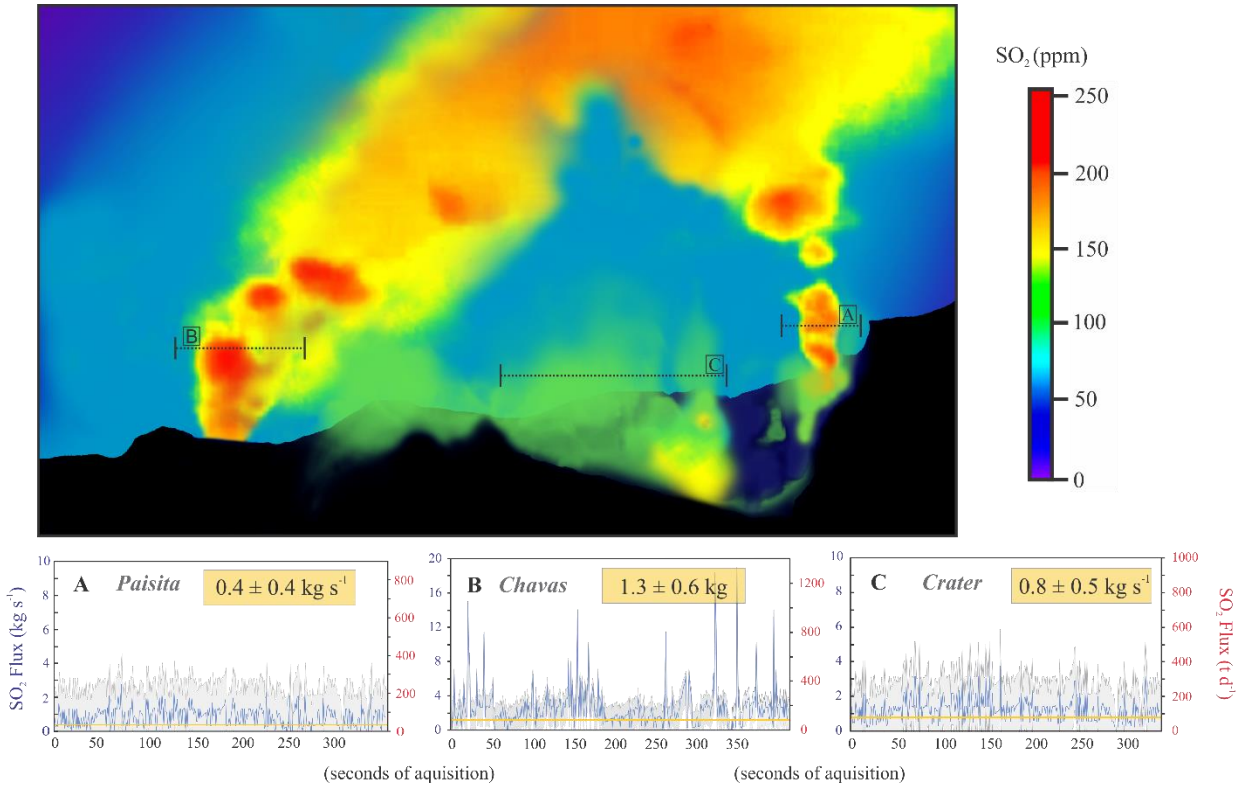

Figure 4.6: Dual UV camera SO_2 flux retrievals from (a) Paisita, (b) Chavas, and (c) the central crater. Pseudo color image of the fumarolic gas from the three different sources, with dashed line cross sections delimiting the area used to calculate the integrated column amounts of SO_2 using the Vulcamera software (Tamburello, Kantzas, McGonigle, and Aiuppa, 2011). Blue lines in (a)–(c) represent the acquired SO_2 flux time series (± 1σ; in light gray), with acquisition time averages marked in yellow.

4.5. Discussion

4.5.1. Magmatic versus Hydrothermal Gas Compositions

Our measurements here supply new information to the (currently limited) existing knowledge on the volcanic gas signature of the CAS-NVZ. The gas results for the three volcanoes are summarized and illustrated in the CO_2-S_T*5-H_2O/10 triangular plots of Figure 4.7 and 4.8.

To the best of our knowledge, our observations represent the first ever results obtained for the major element composition of the Nevado del Ruiz volcanic plume, the strongest source of SO_2 in the NVZ (Carn et al., 2017). Previous volcanic gas information on the volcano was limited to a few analyses of low-temperature (82–103 °C) hydrothermal steam vents and fumaroles collected in the crater area and along the volcano's flanks in the months following the lethal 13 November 1985 eruption (Giggenbach et al., 1990; Fig. 4.7a and 4.8). However, according to Giggenbach et al. (1990), the compositions of these low-temperature fumaroles may have been only partially representative of the original magmatic gas signature, owing to potential scrubbing of S (and Cl) during hydrothermal gas-water interactions. Our 2014–2017 plume compositions, in contrast,

being fed by high-temperature vent degassing activity from the Arenas crater, are likely more representative of the magmatic conditions at Nevado del Ruiz. The “magmatic” nature of the 2014–2017 plumes is supported by their S-rich compositions (Figure 4.7a), well within the typical magmatic arc gas range (Aiuppa, Fischer, et al., 2017), and by the prevalence of SO_2 over H_2S (H_2S/SO_2 ratios < 0.2; Fig. 4.8). These SO_2-rich compositions are clear evidence of sustained shallow magma circulation (and degassing) underneath the Arenas crater, as supported by repeated episodes of seismic activity presumably related to active dome emplacement and growth at the summit crater, events closely monitored by the local observatory in Manizales (SGC-OVSM). By averaging our gas data from all categories (I to III), we infer a time-averaged 2014–2017 gas plume composition of 91.7 ± 33.8, 6.0 ± 1.0, and 2.0 ± 1.5 mol% for H_2O, CO_2, and S_T ($\pm 1\sigma$). This is only slightly less H_2O rich and more CO_2-S_T rich (e.g., more magmatic in nature) than are the average fumarole compositions of Giggenbach et al. (1990), which reported averages of 95.6, 2.4, and 1.5 mol% for H_2O, CO_2, and S_T, respectively. Both data sets show a similar spread of compositions around the average (see Fig. 4.7a). Chemical variability in the Giggenbach et al. (1990) data set likely reflects variable extents of S scrubbing during hydrothermal processing (and/or meteoric-hydrothermal water addition) in the low-temperature manifestations studied. In contrast, hydrothermal processing is unlikely at the open-vent plume degassing conditions reported here, and the 2014-2017 data scatter are more likely to have been caused by a combination of (i) real temporal variations in degassing dynamics (e.g., variations in melt gas bubble content and gas-melt separation pressure) and/or (ii) the different extents of atmospheric dilution in measured plumes (highlighted by the compositional dependence on SO_2 MAX illustrated in Fig. 4.2 and 4.3). We argue that the Category I plume data (dilute plume conditions, SO_2 MAX <5), for which more S-poor compositions (e.g., higher CO_2/S_T and H_2O/S_T) are observed, do likely overestimate the real magmatic signature, due to less accurate corrections of background CO_2 and H_2O contents and/or because of additional gas sources. Therefore, we infer the magmatic CO_2/S_T and H_2O/S_T ratios at 3.9 ± 1.6 and 63 ± 45 by averaging Category II and III data only (Figures 2c, 2d, and 7).

In contrast to the magmatic signature of the Nevado del Ruiz plume(s), measurements taken at both Puracé (Figure 7b) and Galeras (Figure 7c) imply a more hydrothermal nature of the emitted gases. The Puracé gases, in particular, are S depleted relative to the Nevado del Ruiz magmatic field, implying some extent of hydrothermal processing (S scrubbing). Even the hottest of the Puracé fumaroles (fumarola lateral, T = 135 °C) has CO_2/S_T ratio of 14.0 ± 2.3, a factor of ~3 higher than in the “magmatic” Nevado del Ruiz gas. Hydrothermal processing in this fumarole is also supported by the higher H_2S/SO_2 (0.7) and H_2/SO_2 (0.3) ratios (the H_2/SO_2 ratio averaged <0.2 at Nevado del Ruiz). Thus, although the presence of SO_2 in the gas confirms some extent of magmatic gas supply to the system (Maldonado et al., 2017), still hydrothermal reactions appear to play a decisive control on the composition of the emitted gases. This is even more so for the low-temperature, CO_2-rich (up to ~90 mol% of CO_2 at San Juan de Puracé) hydrothermal fumaroles located on the volcano's periphery, in which any magmatic SO_2 has been scavenged by percolating meteoric and hydrothermal fluids and eventually converted into H2S during hydrothermal reactions (Sturchio et al., 1993). Here CO_2/S_T ratios range from ~30 to 55.

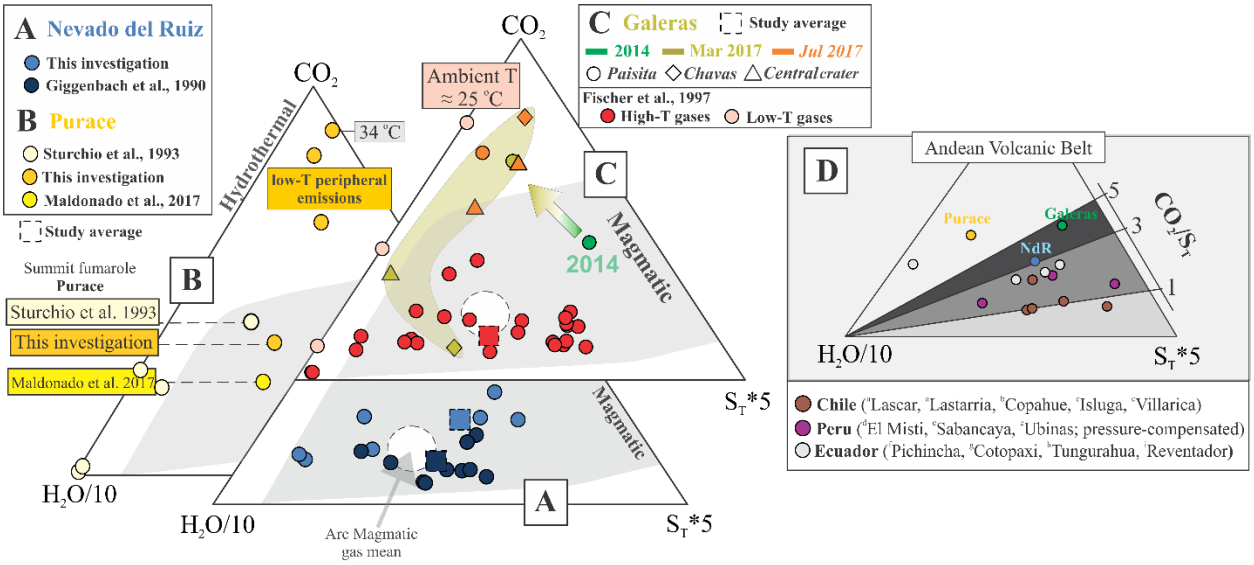

Figure 4.7: (left) Ternary diagrams showing normalized gas composition for (a) Nevado del Ruiz (in blue), (b) Puracé (in yellow), and (c) Galeras (in red) considering H_2O/10-CO_2-S_T*5 (S_T [SO_2 + H_2S]). Closed circles represent data collected throughout this investigation, whereas square symbols represent reference literature studies for each volcano (Giggenbach et al., 1990 for Nevado del Ruiz; Sturchio et al., 1993 for Puracé; and Fischer et al., 1997 for Galeras). Compositional averages are plotted in dark closed circles (this study) and dark squares (literature). Global magmatic arc-gas samples define the gray area characterized by S-rich gases, with correspondent arc-gas mean estimated by Aiuppa, Fischer, et al. (2017). Red area in (c), plotting along the H_2O-CO_2 axis, marks the compositional shift toward more S-depleted, hydrothermal gases in Galeras from 2014 to 2017. (right) Ternary diagrams showing high-temperature volcanic gas compositions along the Andean Volcanic Belt. Estimated averages from this study are given in triangles, with reference literature averages for Colombia represented in squares. Other arc segments are plotted as follows: (i) In white Ecuador (Guagua Pichincha (Fischer and Chiodini, 2015); Cotopaxi [Hidalgo et al., 2017]; Tungurahua and Reventador (Aiuppa et al., 2019)); (ii) in dark gray Peru (El Misti [Moussallam et al., 2017], Sabancaya and Ubinas [Moussallam, Tamburello, et al., 2017]); and (iii) in light gray Chile (Lascar and Lastarria, (Tamburello et al., 2014); Copahue (Tamburello et al., 2015); Isluga and Tacora (Schipper et al., 2017); Villarica (Aiuppa et al., 2019)). Noticeable trends in CO_2/S_T plotting along the S_T-CO_2 show along-arc trends in volcanic gas compositions for the different segments (yellow graded areas represent, from the bottom, CO_2/S_T = 1, 2, and 5). Note that low-temperature systems such as Guagua Pichincha and Puracé plot near the H_2O-CO_2 axis region due to the S-depleted nature of gas emissions.

Interestingly, our 2014–2017 observations also reveal a hydrothermal gas signature for Galeras, which contrasts with the magmatic (S_T-rich) gas signature reported during intense, high-temperature (up to >600 °C) degassing in the late 1980s to mid-1990s (Fischer et al., 1997; see Figure 4.7c). In particular, the Galeras gases in 2017, when the most detailed surveys took place, plot close to the H_2O-CO_2 axis (Fig. 4.7c), and their hydrothermal signature is confirmed by a time-averaged composition of 77.4 ± 10.2 mol% H_2O, 21.6 ± 3.0 mol% CO_2, and 0.9 ± 0.1 S_T (here excluding the more "magmatic" composition measured in Chavas in March 2017 of mol% of 97.0 ± 2.4, 1.6 ± 0.2, and 1.0 ± 0.1 for H_2O, CO_2, and S_T, respectively). These are far more S depleted relative to the typical magmatic arc gas signatures reported by Fischer et al. (1997) for the 1988–1995 period (mean composition 94.4, 3.6, and 1.9 mol% of H_2O, CO_2, and S_T). The hydrothermal signature of the Galeras gases is also well consistent with the more reducing redox conditions (H_2S/SO_2 and H_2/SO_2 >1; Table 1b) relative to Nevado del Ruiz gas (see also Figure 8,

where the majority of the Galeras samples fall within the "hydrothermal-dominated" field determined by Stix and de Moor, 2018, for arc gases from Central American Volcanic Arc).

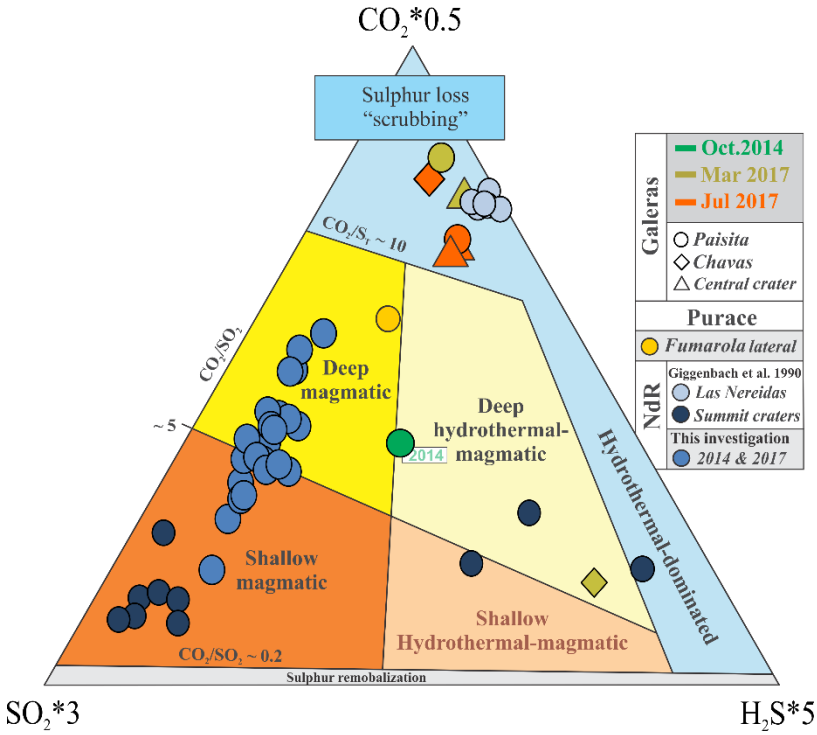

Figure 4.8: Ternary diagram of SO_2*3-CO_2-H_2S*5 showing hydrothermal-magmatic gas compositions from Nevado del Ruiz (Giggenbach et al., 1990, and this study; in blue), Galeras (2014–2017), and Purace (2017, in yellow). The diagram is adapted from Stix and de Moor (2018). Colored composition fields are based on Aiuppa et al. (2014) and de Moor et al., 2016, 2017. Source boundaries are estimated with key gas ratio values reported for Central American Volcanic Arc volcanism.

To better understand the mechanisms controlling the hydrothermal nature of Galeras gases, we integrated our SO_2 flux and CO_2/S_T data (2014–2017) with previous gas information reported for the 1988–1995 period of volcanic unrest at Galeras (Fischer et al., 1997; Zapata et al., 1997; Figure 9a). In its recent history, Galeras has exhibited a wide range of SO_2 fluxes, with emission peaks between 1989 and 1990 (yearly averages of ~19 kg/s, or >1,600 t/day), followed by a general decline between 1991 and 1993 (yearly averages of 3.0–6.6 kg/s, or 260–572 t/day) and then a more sustained drop in the two years that followed (yearly average ~2 kg/s, or ~262 t/day, between 1994 and 1995; Zapata et al., 1997; Fig. 4.9a). Our new results show that between 2014 and 2017, the SO_2 flux has systematically remained <10 kg/s, with the majority of the recorded fluxes ranging between 3 and 6 kg/s (~300 to 500 t/day). This suggests a reduced magmatic gas supply relative to the 1989-1990 degassing unrest, when the CO_2/S_T ratios were consistently (and systematically) the lowest (e.g., more magmatic in nature; Fischer et al., 1997; see Fig. 4.9a). The lowest SO_2 fluxes on our records were measured in 2017, when no reliable SO_2 flux was derived by the NOVAC scanning DOAS, and low fluxes (~2.5 kg/s) were consistently measured by our more

proximal UV camera observations (Fig. 4.6). Contemporarily, the highest CO_2/S_T ratios were also measured from fumarolic discharges in Galeras (Fig. 4.4 and 4.9a).

We thus conclude that a reduced magmatic gas transport, combined with a more intense S scrubbing in the shallow hydrothermal system, was the most likely factor governing the observed gas compositional contrast between 2017 and 1989–1990 (Fig. 4.9a). Variable extents of magmatic S scrubbing in the shallow hydrothermal system may also explain the chemical heterogeneities observed between the different Galeras emission sources in 2017 (Paisita, Chavas, and the central crater). Our vent-resolved SO_2 flux observations in March clearly show that most S-depleted gas compositions at Paisita (CO_2/SO_2 ratio of 87.3 ± 17.4) corresponded to the lowest SO_2 fluxes (~0.4 kg/s), while somewhat more magmatic CO_2/SO_2 ratios (5.4 ± 0.8) were simultaneously observed at Chavas, the most actively degassing vent at that time (~1.3 kg/s).

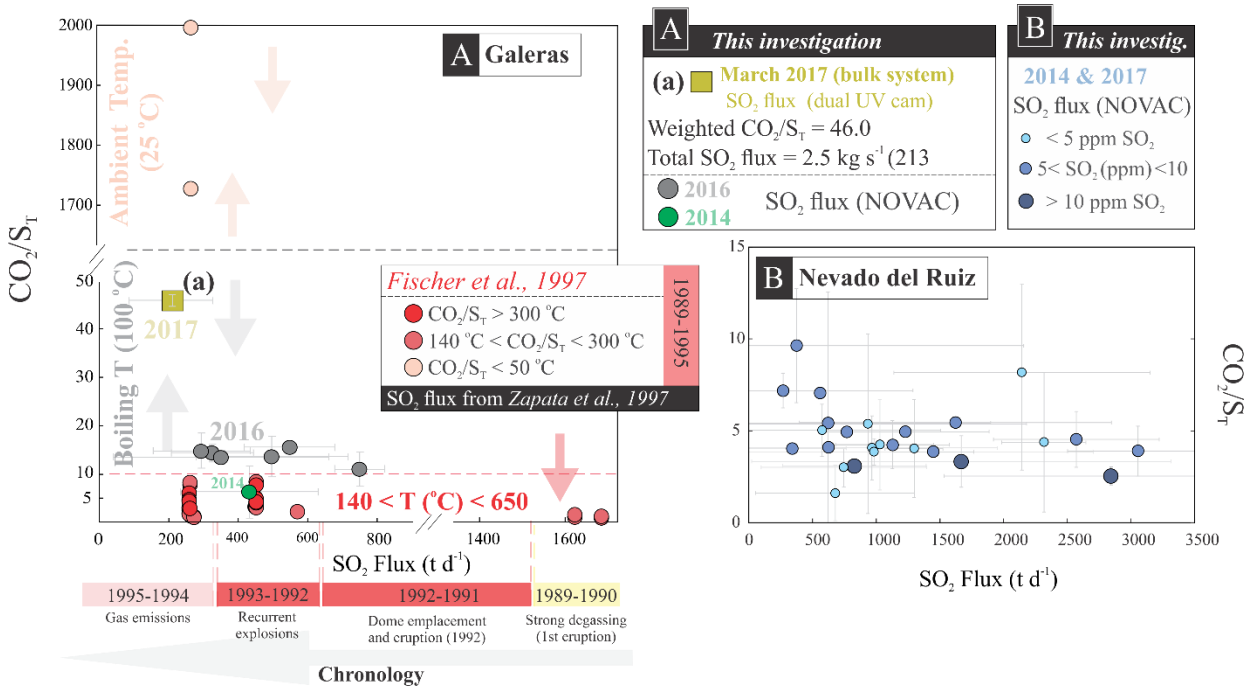

Figure 4.9: (a) Galeras: CO_2/S_T versus SO_2 flux (t/day) from 1989 to 1995 (CO_2/S_T from Fischer et al., 1997, and SO_2 flux data from Zapata et al., 1997), in different shades of red representing different gas temperature ranges. February–July 2016 data in gray (SO2 flux records from NOVAC) and 2017 data in olive drab square SO2 flux estimates from dual UV camera system); 1989–1995 activity chronology at Galeras is given below (a) (from Zapata et al., 1997). (b) Nevado del Ruiz: CO_2/ S_T versus SO_2 flux (t/day), in blue. Categories I to III are distinguishable by different circle sizes, and darker tones of blue for higher SO_2 concentrations.

Our 2014–2016 SO_2 fluxes were in the same range as in 1991–1993, yet the gas CO_2/S_T ratios were sizably higher, especially in 2016 (Figure 9a). We ascribe this compositional difference to the significantly different vent temperatures observed in 2014–2016 (fumaroles close to boiling temperatures) and those reported between 1991 and 1993 (140–650 °C). Lower vent temperatures imply more intense S scrubbing along the vent feeding chimneys (Aiuppa, Fischer, et al., 2017), thus contributing to a more hydrothermal gas signature compared to the magmatic (S_T-rich)

compositions observed during intense, high-temperature degassing (Fischer et al., 1997; see Figure 4.7c). Sulfur dioxide fluxes and CO_2/S_T data are also shown for Nevado del Ruiz in Figure 4.9b.

4.5.2. Gas Fluxes and Implications for the CAS Volatile Budget

Carbon dioxide and other volatile emissions can be derived for each of the three volcanoes by combining the co-acquired SO_2 fluxes (Tab. 4.2) and volcanic gas CO_2/SO_2 ratios (Tab. 4.1). The uncertainties reported in this section are expressed as the standard error of the regression analysis and subsequent error propagation; error on inferred flux propagates error on the SO_2 fluxes and x/SO_2 ratios.

At Nevado del Ruiz, we establish a CO_2 flux time series (Fig. 4.10) by using in tandem, for each measurement day, the daily averaged CO_2/SO_2 ratios (Fig. 4.3) and SO_2 flux estimates (Figure 5). The so derived daily averaged CO_2 fluxes range from ~9 to 139 kg/s (arithmetic mean, 43 ± 30) and have associated errors of 40% to >100%. These large uncertainties reflect the large inter-daily variability of both CO_2/SO_2 ratios and, especially, that of SO_2 fluxes, possibly caused by (i) the nonstationary nature of degassing at Nevado del Ruiz that consists of intermittent large pulses of SO_2 release interspersed within phases of milder and more continuous SO_2 degassing (e.g., Dinger et al., 2018; Malinconico, 1987), and (ii) the complex wind field patterns at the volcano's height that produce erratic changes in plume transport direction and speed (these being hard to quantify and taken into account in flux calculations). Here we attempted to minimize the effect of a time-variable atmospheric plume dispersion, by applying a set of filtering parameters that only scans the captured ≥85% of the gas plume that were selected for daily average estimates. Still, the daily variability of our NOVAC-based SO_2 fluxes remain large (39% and above).

In view of the above, we find it more prudent to derive the long-term SO_2 and CO_2 emission budgets for Nevado del Ruiz by deriving weighted flux averages based on the standard deviations of each daily measurement (Fig. 4.5 and 4.10). Doing so, the daily gas fluxes with lower variability are assigned a proportionally higher weight in the mean flux calculation (note that for CO_2, the daily averaged fluxes with >100% relative uncertainty are not used in the calculation). From this method, we derive a time-averaged SO_2 flux weighted mean of ~8 kg/s, well below the arithmetic mean flux of 14 kg/s and at the lower range of the daily SO_2 fluxes reported (~$3_{[min]}$–$35_{[max]}$ kg/s; Table 2). Similarly, we estimate a weighted CO_2 flux average of ~23 kg/s, which is ~50% lower than the arithmetic mean (~43 kg/s). The same procedure leads to deriving H_2O, H_2S, and H_2 fluxes of ~330, 0.6, and 0.05 kg/s, from which we infer a time-averaged total volatile flux (TV flux) for Nevado del Ruiz in 2014–2017 of ~363 kg/s (~31,300 t/day). In comparison with other persistently active arc sources, for example, Aiuppa et al. (2008) estimated a TV flux for Mount Etna of ~243 kg/s (or ~21,000 t/day), while Bani et al. (2018) reported TV flux estimates of ~172 kg/s for Dukono. Despite the big uncertainties associated with studies of this nature, such comparisons do provide strong evidence that Nevado del Ruiz is, in fact, one of the strongest volcanic arc gas point sources globally.

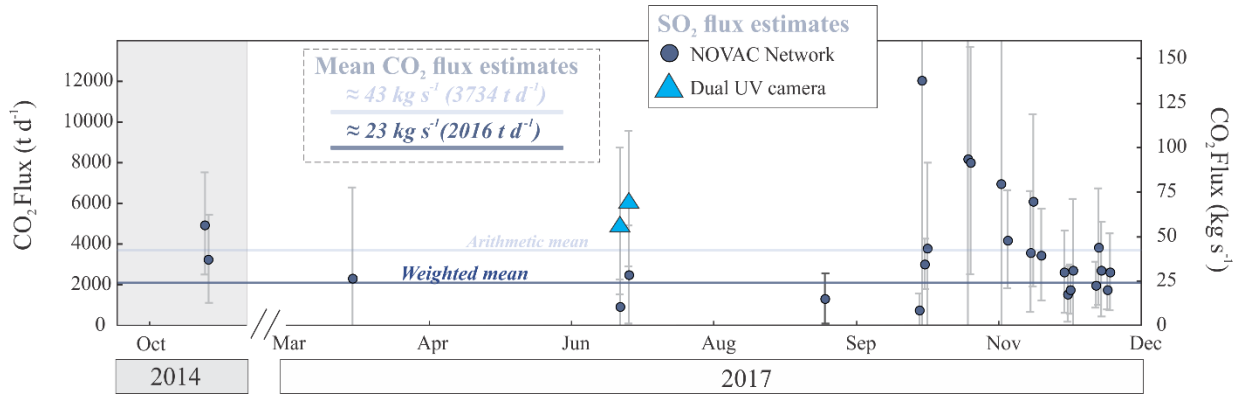

Figure 4.10: CO_2 time series for Nevado del Ruiz (in kg/s and t/day) for October 2014 and from March to December 2017. Note that CO_2 flux estimates are restricted to days in which volcanic gas compositions were acquired. Weighted mean was calculated using only CO_2 flux measurements whose error is constrained within 100% of the average. Estimates of CO_2 fluxes combining CO_2/SO_2 with the dual UV camera portable system are represented as triangles as a reference, and the arithmetic mean including all estimates is given also as a comparison. Errors (σ) are expressed as the standard error of the regression analysis and subsequent error propagation on the SO_2 fluxes and x/SO_2 ratios.

Within the CAS, Galeras and Puracé volatile budgets are here characterized, although with a lower level of detail (Tables 4.2b and 4.2c, respectively). At Puracé, we only have compositional data for one measurement day (23 March 2017; Table 4.1c). By scaling this by the NOVAC-based daily averaged SO_2 flux of ~0.1 kg/s (or 9 ± 4 t/day), we assess the H_2O and CO_2 fluxes at 6 ± 1 and 1 ± 0.2 kg/s respectively. The TV flux from summit subaerial discharges (fumarola lateral) is thus estimated at 7 kg/s (or 600 t/day TV flux), to which both H_2S and H_2 contribute ≪0.1 kg/s. This is a factor ~10 less than the TV flux reported by Maldonado et al. (2017) of 73 kg/s (or ~6340 t/day) derived in 2016, who yet used a much higher SO_2 flux of ~2 kg/s (208 t/day). Clearly, the volatile emissions from Puracé are not stationary over time, and simultaneous composition and flux records are required.

At Galeras, both compositions and fluxes have repeatedly been measured in 2014–2017. The majority of the SO_2 flux records are from the scanning NOVAC instrument and are thus representative of the bulk plume. Between 2014 and 2016 our compositional measurements focused on the Paisita summit fumarole (cf. section 3), whose vigorous degassing clearly prevailed over any other summit fumarolic volatile discharge over that period. Our 2014–2016 volatile flux estimates (Tab. 4.2) are thus based on the assumption that the Paisita fumarole was representative of the bulk plume composition. In 2017 a large vent-to-vent chemical variability was observed, and thus, the volatile fluxes for Paisita, Chavas, and the central crater are independently evaluated (Tab. 4.2) using the vent-resolved SO_2 flux results obtained with the UV camera on 21 March 2017 (Fig. 4.6). From these, and from the co-acquired compositional data (Table 1), the weighted bulk volatile flux average (2014–2017) for Galeras is estimated at ~76 kg/s (or ~6,543-t/day TV flux; Table 3). It is important to note that our average estimates (Table 3) are weighted based on the daily uncertainties of gas composition (x/SO_2) and SO_2 fluxes reported for each day. Therefore, we here report a TV flux that is unsurprisingly much closer to the values reported in 2014 than to those of 2017, as a result of more favorable measurement conditions (especially in situ composition

measurements favored by less diluted gas plumes) due to the system's more persistent degassing (see section 4.2) at the beginning of this study. According to our calculations, a recent (2014–2017) time-averaged CO_2 output from Galeras of ~30 kg/s, more than a factor of 2 larger than the 1989–1995 time-averaged CO_2 output of 12 kg/s (Zapata et al., 1997) clearly indicates that the volcano remains a significant volcanic CO_2 source even during the ongoing period of quiescence and hydrothermal degassing (Fig. 4.11).

The cumulative CO_2 flux contribution from Nevado del Ruiz, Galeras, and Puracé is thus estimated at ~54 kg/s (or ~4,701 t/day; Fig. 4.11). Nevado del Huila (e.g. Pulgarín et al., 2001), another relevant subaerial emission source in the CAS, has been persistently degassing over the last decades, especially during its most recent eruptive period (2009–2012) when it emitted ~862 t/day of CO2 (Aiuppa et al., 2019). We here use these estimations to infer a total volcanic CO_2 flux from the four most actively degassing CAS subaerial volcanoes at approximately 5,563 t/day. In perspective, this corresponds to more than 50% of present-day (2005–2015) total volcanic CO_2 emissions from the active volcanoes of the Andean Volcanic Belt (derived at ~10,000 t/day from data in Aiuppa et al., 2019). Notably, Nevado del Ruiz and Galeras together contribute ~35% to the subaerial volcanic CO_2 emission budget in the Andean Volcanic Belt and are thus larger CO_2 sources than any other active volcano in Ecuador (Hidalgo et al., 2016, 2018), Peru (Moussallam et al., 2017; Moussallam, Tamburello, et al., 2017), and Chile (Tamburello et al., 2014).

4.5.3. Along-Trench CO_2/S_T Variations and Volatile Recycling

Our results above provide novel information on the geochemical cycle of C, and other volatiles, through subduction zones (e.g., the fraction of slab-derived C being recycled through subaerial degassing along the CAS). Plank and Langmuir (1988) first investigated the chemical nature of the sediments subducting underneath the Colombian trench and reported approximately 50% carbonate in the bulk core. A recent update by Plank (2014) on bulk concentration data for this arc segment confirms the C-rich nature of these sediments (predominantly siliceous oozes and limestones), with CO_2 and H_2O bulk sediment concentrations of 25.26 and 5.27 (wt%), respectively. From this, we estimate that about 6.19×10^{12} g C/year are being subducted through slab sediments underneath the CAS (von Huene and Scholl, 1991; Jarrard, 2003; Syracuse and Abers, 2006).

However, other C sources (e.g., sedimentary organic C) may play a significant role in the remobilization of C, and such contributions can be distinguished based on observed $CO_2/^3He$ ratios and $\delta^{13}C$ isotopic signatures (Sano and Marty, 1995). To the best of our knowledge, $\delta^{13}C$ isotope characterization of Nevado del Ruiz has only been reported for thermal and surface waters related to the hydrothermal system of the volcano (Sturchio et al., 1988). These low-temperature media (below boiling) show isotopic signatures as light as −11.4‰, which likely reflect various extents of isotope fractionation and/or mixing of magmatic and organic components. At Pandiaco mineral spring (Galeras) low-temperature gas discharges (consisting of almost pure CO_2; see Sano et al., 1997) also yield isotopic signatures more organic in nature ($\delta^{13}C$ values as negative as −9.16‰) with negligibly small mantle Carbon contribution. For temperature ranges similar to those of

Nevado del Ruiz thermal waters and Pandiaco (Galeras), Purace also show $\delta^{13}C$ isotopic values as low as −11.5‰ (Sturchio et al., 1988). Although this data has proved crucial to our understanding of hydrothermal systems, it is most likely not representative of the magmatic end-member of these volcanic systems. On the other hand, high-temperature crater samples (up to 350 °C) reported by Sano et al. (1997) for Galeras consistently fall within mid-ocean ridge basalt range (5‰ ± 3‰). In addition, high-temperature fumarole data consistently displaying $CO_2/^3He$ ratios (average 2.3×10^{10} from Sano and Williams, 1996, and Sano et al., 1997) 1 order of magnitude greater than the mid-ocean ridge basalt range ($2 \pm 1 \times 10^9$; see Marty and Tolstikhin, 1998) possibly reveal the addition of slab-derived carbon to the mantle component. The same authors attribute up to 79% of the C to be derived from limestone (including slab carbonate), which suggests that slab-derived C represents indeed a very considerable portion of total C in the system. Moreover, unusually high (for arc volcanoes) $^3He/^4He$ ratios reported for high-temperature gas emissions (350 °C) in Galeras (as high as 8.8 Ra; see Sano et al., 1997) also suggest a minor role of the crustal component in the Galeras gas emissions.

Therefore, based on our estimates in section 5.2, we infer that subaerial degassing volcanoes along the CAS are currently releasing a small fraction (roughly 30%, or 2.0×10^{12} g C/year) of the carbon being subducted in this region. This mismatch between C inputs at trench and C outputs at the Colombian trench is most likely larger if considering other C sources, as discussed above. However, our reports contribute additional information to earlier calculations made for other arc segments (e.g., de Moor et al., 2017; Hilton et al., 2002) and implies (i) a limited C recycling efficiency in the slab (due to high slab carbonate stability (see recent discussion by Keleman and Manning, 2013); (ii) that C is primarily recycled by forms of degassing other than

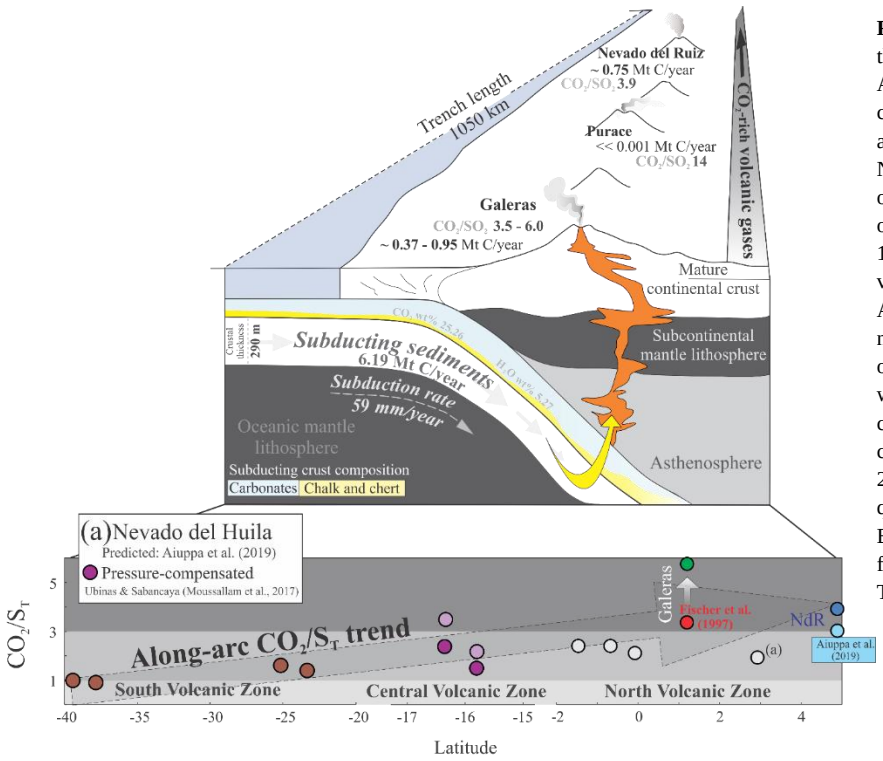

Figure 4.11. Schematic figure showing the nature of the sediments subducting underneath the Colombian Arc Segment (CAS), with respective sediment composition. Estimated carbon fluxes (in Mt C/year) and gas compositions estimated in here are given for Nevado del Ruiz, Puracé, and Galeras. The quoted CO_2 output range for Galeras is based upon a combination of 2014–2017 (this study) and 1989 1995 (Zapata et al., 1997) results. The bottom plot illustrates the along-arc variations in gas CO_2/S_T ratio signature in South America. For Galeras, we report the more magmatic-in-nature CO_2/S_T ratio (green circle; October 2014) obtained throughout this investigation and compare it with the composition of high temperature gases collected during the 1989–1995 period of unrest (red circle; Fischer et al., 1997; Aiuppa, Fischer, et al., 2017). For Nevado del Ruiz, the original CO_2/S_T ratio quoted in Aiuppa et al. (2019) is shown for comparison. Both pressure-compensated and uncorrected CO_2/S_T for Sabancaya and Ubinas (Peru; Moussallam, Tamburello, et al., 2017) are given for comparison.

plumes/fumaroles at central volcanoes (e.g., soils and/or groundwater; Chiodini et al., 1998; Tamburello et al., 2018); or (iii) that significant carbon sequestration occurs in the forearc crust, as suggested by Barry et al. (2019).

The data set of Plank (2013) also identifies substantial along-arc variations in the mineralogy and chemistry of sediments subducting underneath the Andean Volcanic Belt. In particular, it is shown that the CO2 content of the subducting sediments decreases southward along the arc, from 25.26 wt% in the NVZ (Colombia), 24.53 wt% in the CVZ (Peru), to 0–1.5 wt% in the Chilean segment of the arc (Fig. 4.10). Our novel gas compositional data for Nevado de Ruiz, combined with available magmatic gas information for Galeras (Fischer et al., 1997), and other strongly degassing volcanoes in the Andes (see legend of Fig. 4.7 for data provenance), allow us to more fully characterize the along-arc variations in the gas CO_2/S_T ratio, as illustrated in figure 4.11. Interestingly, we find a systematic along-arc trend in the magmatic gas CO_2/S_T ratio, which decreases from ~5 in Colombia, ~2 in the CVZ (Moussallam et al., 2017; Moussallam, Tamburello, et al., 2017), to ~1 in southern Chile (Tamburello et al., 2015), thus matching the north-to-south decrease in the sediment CO_2 contents, described above. This observation provides additional experimental evidence for earlier indications from a global data set (Aiuppa, Fischer, et al., 2017; Aiuppa et al., 2019) that slab sediment composition plays a decisive control on the CO_2/S_T ratio signature of arc magmatic gases. We ultimately propose that although the C recycling efficiency along the CAS is likely to be low (see above), sediments subducted at the Colombian trench are so C enriched to impart a high CO_2/S_T ratio signature to the magmatic gases degassed in the overlying volcanic arc.

4.6. Conclusions

We reported on the composition and flux of gases emitted along the CAS of the NVZ between 2014 and 2017, measuring in situ volcanic gas compositions using a MultiGAS and estimating SO_2 fluxes by using scanning UV spectrometers and UV cameras. Despite the wide range in gas composition and flux values observed, mostly due to variables associated with degassing dynamics and measurement difficulties at such extreme conditions, data here reported stress the importance of the ongoing efforts to quantify subaerial volatile (especially CO_2) emissions from arc volcanism. This study shows that Nevado del Ruiz and Galeras together contribute about 20% to the total subaerial CO_2 emissions of the volcanic arc (~2,017 t/day), clearly reinforcing the importance of newly reported data in the context of global arc volatile emissions. Furthermore, combining this with our updated estimates of subaerial CO_2 emissions rates for Puracé (84 t/day) and the current estimates of ~860 t/day for Nevado del Huila, our work shows that this segment of the arc is responsible for one third of the total subaerial CO_2 of the entire Andean trench, when accounting for the strongest, most persistently degassing volcanoes along the arc. We therefore suggest a strong correlation between subducted sediment compositions at this segment (25.26 CO_2 wt%; 1.50 CO_2 wt% at SVZ in comparison) with here highlighted CO_2/S_T northward increase (Nevado del Ruiz and Galeras ~4–6), once again validating the study of volcanic gas chemistry and arc-scale trends in volatile composition as a powerful tool to investigate processes of volatile input

and recycling into the mantle wedge via the subducted slab. We estimate that about one third (~2 Mt C/year) of the C being subducted (~6.19 Mt C/year) gets resurfaced through subaerial volcanic gas emissions in Colombia (NdR ~0.7 Mt C/year). Finally, newly established temporally resolved volcanic gas time series for Nevado del Ruiz and Galeras set a crucial background in gas-related monitoring parameters (e.g., CO_2/SO_2, proven to be a powerful monitoring tool especially for CO_2-rich volcanic systems) and will hopefully help the ongoing efforts to predict transitions from quiescence to periods of volcanic unrest at such hazardous volcanoes.

4.7. Acknowledgments

We are deeply grateful to all the Servicio Geológico Colombiano staff and Observatorios Vulcanológicos y Sismológicos of Manizales, Popayán, and Pasto personnel for their continuous logistical and scientific support throughout this investigation. Initial funding for producing the NOVAC data set here presented was provided by the European Commission FP5 (DORSIVA project) and FP6 (NOVAC project), and the operation of the NOVAC network is funded through initiatives of the Volcano Observatories and support from the Volcano Disaster Assistance Program of the United States Geological Survey (SGS). We would also like to acknowledge the crucial support from the Alfred P. Sloan Foundation (Deep Carbon Observatory/DECADE project; UniPa-CiW subcontract 10881-1262) and the MIUR (under grant PRIN2017-2017LMNLAW) for funding a large portion of this project. This manuscript has benefited from constructive reviews from Felipe Aguilera, Maarten de Moor, and one anonymous reviewer. The new data set generated in this study is available at the EarthChem data repository (https://doi.org/10.1594/IEDA/111393).

Chapter 4 – Table(s)

Table 4.1: (a-c) X/SO_2 molar ratios measured by MultiGAS and gas composition of Nevado del Ruiz (a), Galeras (b) and Puracé (c) with error represented as 1σ from the weighted daily mean.

Table 4.2: (a-c) Inferred flux range of each species is based on an SO_2 flux estimates from the NOVAC Network. Errors are expressed as the standard error of the regression analysis and subsequent error propagation, error on inferred flux propagate error on the SO_2 fluxes and gas ratios. Tables 2A.1 (Nevado del Ruiz) and 2B.1 (Galeras) show SO_2 flux values acquired using the dual UV camera system.

Table 4.3: Weighted TV Flux averages for Nevado del Ruiz, Galeras and Puracé. Note that averages are calculated based on daily uncertainties of both composition (x/SO_2; daily uncertainties reported in Tab. 4.1 [a-c]) and SO_2 flux measurements (daily uncertainties reported in Tab. 4.2 [a-c]).

Date	Molar ratio CO_2/SO_2	Error (1σ)	Molar ratio H_2S/SO_2	Error (1σ)	Molar ratio H_2/SO_2	Error (1σ)	Molar ratio H_2O/SO_2	Error (1σ)	SO_2 *Max*	Composition (mol%)									
										SO_2	(1σ)	CO_2	(1σ)	H_2S	(1σ)	H_2	(1σ)	H_2O	(1σ)
Table 1°. Nevado del Ruiz																			
21 Oct 14	2.6	0.5	0.12	<0.01	0.08	<0.01	26	10	11.0	3.4	n/d	8.6	1.7	0.4	0.0	0.3	0.0	87.3	34.2
22 Oct 14	4.2	1.5	0.11	0.01	0.07	0.02	---	---	3.9	---	---	---	---	---	---	---	---	---	---
29 Mar 17	5.4	5.3	0.14	<0.01	0.45	0.21	323	48	4.4	0.3	n/d	1.7	1.6	0.0	0.0	0.1	0.1	97.9	14.5
1 Jul 17	4.1	2.5	0.20	<0.01	0.21	<0.01	---	---	3.4	---	---	---	---	---	---	---	---	---	---
2 Jul 17	5.4	2.0	0.19	<0.01	0.18	<0.01	---	---	3.8	---	---	---	---	---	---	---	---	---	---
4 Jul 17	9.6	3.8	0.18	<0.01	0.17	<0.01	---	---	4.8	---	---	---	---	---	---	---	---	---	---
11 Sep 17	7.2	2.8	0.14	<0.01	0.18	<0.01	164	41	4.0	0.6	n/d	4.2	1.6	0.1	0.0	0.1	0.0	95.1	237.2
14 Oct 17	1.6	1.3	0.12	<0.01	0.20	0.1	---	---	7.0	---	---	---	---	---	---	---	---	---	---
15 Oct 17	8.2	7.1	0.13	<0.01	0.24	<0.01	---	---	6.0	---	---	---	---	---	---	---	---	---	---
16 Oct 17	4.3	0.2	0.13	<0.01	0.12	<0.01	----	---	10.0	---	---	---	---	---	---	---	---	---	---
17 Oct 17	3.3	1.4	0.12	<0.01	0.09	<0.01	127	38	14.8	0.8	n/d	2.5	1.1	0.1	0.0	0.1	0.0	96.6	28.8
31 Oct 17	3.9	4.9	0.10	<0.01	0.19	0.2	---	---	2.9	---	---	---	---	---	---	---	---	---	---
1 Nov 17	4.5	0.7	0.14	<0.01	0.21	0.01	---	---	3.5	---	---	---	---	---	---	---	---	---	---
12 Nov 17	4.4	3.1	0.10	0.01	0.21	0.10	---	---	5.6	---	---	---	---	---	---	---	---	---	---
14 Nov 17	5.0	1.1	0.14	<0.01	0.21	0.08	---	---	4.0	---	---	---	---	---	---	---	---	---	---
22 Nov 17	4.0	0.9	0.14	<0.01	0.11	<0.01	---	---	6.6	---	---	---	---	---	---	---	---	---	---
23 Nov 17	5.5	1.8	0.16	<0.01	0.20	0.09	---	---	2.7	---	---	---	---	---	---	---	---	---	---
26 Nov 17	5.4	1.4	0.12	<0.01	0.12	<0.01	---	---	8.0	---	---	---	---	---	---	---	---	---	---
4 Dec 17	3.9	1.5	0.15	0.02	0.21	0.04	---	---	6.4	---	---	---	---	---	---	---	---	---	---

5 Dec 17	3.0	0.0	0.13	0.01	0.16	0.02	---	---	7.0	---	---	---	---	---	---	---	---	---	---	---
6 Dec 17	3.1	0.0	0.13	<0.01	0.19	<0.01	41	22	10.1	2.2	n/d	6.9	0.0	0.3	0.0	0.4	0.0	90.2	48.3
7 Dec 17	4.1	0.0	0.13	<0.01	0.14	<0.01	32	23	9.9	2.7	n/d	10.8	0.0	0.3	0.0	0.4	0.0	85.9	60.3
15 Dec 17	5.0	0.2	0.13	<0.01	0.17	<0.01	---	---	7.5	---	---	---	---	---	---	---	---	---	---	---
16 Dec 17	3.9	1.4	0.15	<0.01	0.24	<0.01	---	---	4.0	---	---	---	---	---	---	---	---	---	---	---
17 Dec 17	7.1	4.1	0.13	0.02	0.19	0.03	377	102	1.9	0.3	n/d	1.8	1.1	0.0	0.0	0.1	0.0	97.8	26.5
19 Dec 17	4.1	1.7	0.18	<0.01	0.33	<0.01	---	---	3.5	---	---	---	---	---	---	---	---	---	---	---
20 Dec 17	4.9	1.9	0.14	<0.01	0.25	<0.01	---	---	4.6	---	---	---	---	---	---	---	---	---	---	---
Table 1B. Galeras																				
17 Oct 14	6.0	1.2	0.55	0.04	0.04	0.01	26	13	61.6	3.0	n/d	21.0	4.0	1.6	0.1	0.1	<0.1	74.3	36.0
26 Feb 16	13.4	5.4	---	---	---	---	---	---	27.3	---	---	---	---	---	---	---	---	---	---	---
29 Feb 16	15.3	4.2	---	---	---	---	---	---	56.5	---	---	---	---	---	---	---	---	---	---	---
27 Apr 16	14.2	1.3	---	---	---	---	---	---	73.6	---	---	---	---	---	---	---	---	---	---	---
31 May 16	14.6	1.9	---	---	---	---	---	---	15.1	---	---	---	---	---	---	---	---	---	---	---
13 Jul 16	13.3	3.7	---	---	---	---	---	---	10.8	---	---	---	---	---	---	---	---	---	---	---
18 Jul 16	10.8	1.5	---	---	---	---	---	---	10.6	---	---	---	---	---	---	---	---	---	---	---
21 Mar 17																				
Paisita	87.3	17.4	1.6	0.2	---	---	412	71.1	5.4	0.2	n/d	21.0	4.2	0.3	0.1	---	----	78.4	13.5
Chavas	5.4	0.8	2.3	0.2	1.2	0.4	327	8	5.1	0.3	n/d	1.6	0.2	0.7	0.0	0.4	0.1	97.0	2.4
Central Crater	93.8	6.2	2.4	0.4	3.1	0.6	1951	486	4.9	0.1	n/d	4.8	0.3	0.1	0.0	0.2	0.0	94.9	23.7
13 Jul 17	38.5	2.7	1.5	0.0	---	---	155	2		0.5	n/d	24.5	1.7	0.8	0.0			74.2	1.2

Paisita									6.3								---	---		
Chavas	41.7	0.9	0.9	0.1	---	---	98	<0.1	4.7	0.7	n/d	41.8	0.9	0.7	0.1	---	---	56.8	0.0
Central crater	33.6	13.7	1.2	0.1	---	---	264	16	3.0	0.3	n/d	12.6	5.1	0.4	0.0	---	---	86.6	5.3
14 Jul 17																				
Central crater	33.6	8.0	1.3	0.2	---	---	131	31	2.2	0.6	n/d	25.1	6.0	0.8	0.1	---	---	73.5	17.3
Table 1C. Puracé																				
23 Mar 17	14.0	2.3	0.4	0.2	0.3	0.2	165	47	14.4	0.6	n/d	7.7	1.9	0.2	0.1	0.2	0.1	91.3	25.7
Hydrothermal springs																				
									Agua Herbiendo	---	---	30.1	3.8	0.9	0.0	---	---	69.0	11.3
									Poco Azul	---	---	50.5	12.7	0.5	0.1	---	---	49.0	17.3
									San Juan de Puracé	---	---	89.9	8.5	1.0	0.2	---	---	9.1	3.6

Table 2A. Nevado del Ruiz – Volatile flux estimates derived from SO_2 flux daily averages (NOVAC Network)

Date	H_2O in kg s^{-1} (t d^{-1})	σ	CO_2 in kg s^{-1} (t d^{-1})	σ	SO_2 in kg s^{-1} (t d^{-1})	σ	H_2S in kg s^{-1} (t d^{-1})	σ	H_2 in kg s^{-1} (t d^{-1})	σ
21 Oct 14	238 (20582)	144 (12449)	58 (4893)	29 (2492)	33 (2843)	15 (1312)	2.1 (180)	1.0 (83)	(8)	(3)
22 Oct 14	---	---	38 (3291)	25 (2157))	13 (1129)	7 (623)	0.8 (68)	0.4 (38)	(2)	(2)
29 Mar 17	654 (56536)	1060 (91589)	27 (2328)	51 (4389)	7 (623)	12 (1005)	0.5 (47)	0.9 (75)	(9)	(15)
1 Jul 17	---	---	11 (953)	15 (1312)	4 (342)	5 (423)	0.4 (37)	0.5 (45)	(2)	(3)
2 Jul 17	---	---	---	---	---	---	---	---	---	---
4 Jul 17	---	---	29 (2488)	28 (2392)	4 (376)	4 (329)	0.4 (37)	0.4 (32)	(2)	(2)
11 Sep 17	143 (12359)	377 (32553)	15 (1329)	14 (1224)	3 (269)	3 (226)	0.2 (20)	0.2 (17)	(1)	(1)
14 Oct 17	---	---	9 (755)	9 (788)	8 (678)	5 (444)	0.5 (44)	0.3 (29)	(4)	(3)
15 Oct 17	---	---	139 (12042)	147 (12691)	25 (2143)	15 (1274)	1.8 (153)	1.1 (91)	(16)	(9)
16 Oct 17	---		35 (3004)	14 (1239)	12 (1029)	5 (422)	0.8 (69)	0.3 (28)	(4)	(2)
17 Oct 17	690 (59611)	711 (61458)	44 (3820)	47 (4096)	19 (1668)	19 (1647)	1.2 (104)	1.2 (102)	(5)	(5)
31 Oct 17	---	---	95 (8192)	125 (10771)	35 (3055)	14 (1246)	2.0 (170)	0.8 (69)	(18)	(25)
1 Nov 17	---	---	93 (8019)	64 (5521)	30 (2570)	20 (1722)	2.2 (188)	1.5 (126)	(17)	(11)
12 Nov 17	---	---	81 (6983)	85 (7304)	27 (2316)	21 (1783)	1.4 (120)	1.1 (93)	(15)	(14)
14 Nov 17	---	---	49 (4195)	28 (2385)	14 (1230)	8 (649)	1.1 (92)	0.6 (48)	(8)	(5)
22 Nov 17	---	---	42 (3600)	34 (2955)	15 (1297)	12 (1021)	1.6 (96)	0.9 (76)	(4)	(3)
23 Nov 17	---	---	70 (6080)	48 (4180)	19 (1623)	11 (986)	0.7 (141)	1.0 (86)	(10)	(8)
26 Nov 17	---	---	40 (3460)	26 (2231)	11 (934)	6 (555)	0.5 (58)	0.4 (34)	(3)	(2)
4 Dec 17	---	---	30 (2609)	23 (2009)	11 (983)	8 (651)	0.9 (80)	0.6 (54)	(7)	(4)
5 Dec 17	---	---	18 (1544)	16 (1354)	9 (746)	8 (654)	0.6 (50)	0.5 (44)	(4)	(3)
6 Dec 17	110 (9476)	95 (8184)	20 (1765)	14 (1196)	10 (830)	7 (562)	0.7 (57)	0.5 (39)	(5)	(3)
7 Dec 17	102 (8816)	148 (12760)	31 (2707)	40 (3425)	11 (967)	14 (1223)	0.7 (64)	0.9 (81)	(4)	(5)

15 Dec 17	---	---	23 (1990)	13 (1107)	7 (575)	4 (320)	0.5 (41)	0.3 (23)	(3)	(2)
16 Dec 17	---	---	44 (3844)	33 (2839)	17 (1448)	11 (928)	1.4 (119)	0.9 (76)	(11)	(7)
17 Dec 17	689 (59571)	458 (39561)	32 (2726)	27 (2296)	7 (562)	4 (340)	0.5 (39)	0.3 (24)	(3)	(2)
19 Dec 17	---	---	20 (1761)	11 (984)	7 (625)	3 (242)	0.7 (58)	0.3 (22)	(6)	(2)
20 Dec 17	---	---	30 (2617)	22 (1881)	9 (771)	5 (471)	0.7 (58)	0.4 (35)	(6)	(4)

Table 2A.1 Nevado del Ruiz – Volatile flux estimates derived from SO_2 measurements (dual UV camera system)

1 Jul 17	---	---	59 (5076)	41 (3542)	21 (7)	1823 (632)	2 (195)	1 (67)	(12)	(4)
4 Jul 17	---	---	72 (6185)	38 (3275)	11 (934)	4 (329)	1 (91)	0 (32)	(5)	(2)

Table 2B. Galeras – Volatile flux estimates derived from SO_2 flux daily averages (NOVAC Network)

Date	H_2O in kg s^{-1} (t d^{-1})	σ	CO_2 in kg s^{-1} (t d^{-1})	σ	SO_2 in kg s^{-1} (t d^{-1})	σ	H_2S in kg s^{-1} (t d^{-1})	σ	H_2 in kg s^{-1} (t d^{-1})	σ
17 Oct 14	38 (3287)	13 (1090)	21 (1784)	7 (591)	5.0 (436)	1.4 (118)	1.5 (126)	0.4 (36)	(0.6)	(0.2)
26 Feb 16	---	---	53 (4592)	30 (2573)	5.8 (500)	2.3 (195)	---	---	---	---
29 Feb 16	---	---	67 (5796)	32 (2768)	6.4 (550)	2.5 (215)	---	---	---	---
27 Apr 16	---	---	37 (3229)	15 (1291)	3.8 (330)	1.5 (129)	---	---	---	---
31 May 16	---	---	35 (3000)	14 (1233)	3.5 (300)	1.4 (117)	---	---	---	---
13 Jul 16	---	---	38 (3256)	18 (1553)	4.1 (356)	1.6 (138)	---	---	---	---
18 Jul 16	---	---	64 (5544)	28 (2393)	8.7 (748)	3.5 (306)	---	---	---	---
21 Mar 17	No plume registered by the NOVAC network									
13 Jul 17	No plume registered by the NOVAC network									
14 Jul 17	No plume registered by the NOVAC network									

Table 2B.1 Galeras - Volatile flux estimates derived from SO_2 measurements (dual UV camera system)

21 Mar 17

Paisita	50 (4346)	47 (4078)	26 (2249)	25 (2122)	0.4 (37)	0.4 (35)	0.4 (32)	0.4 (30)	---	----
Chavas	120 (10340)	55 (4779)	5 (420)	2 (203)	1.3 (112)	0.6 (52)	1.6 (138)	0.8 (65)	(4.3)	(1.4)
Central Crater	---	---	52 (4456)	29 (2524)	0.8 (69)	0.5 (39)	1.0 (88)	0.6 (51)	(6.8)	(1.3)
System Total	170 (5991)	103 (8856)	82 (7124)	56 (4844)	2.5 (216)	1.5 (125)	3.0 (259)	1.7 (146)	(11)	(2.7)

Table 2C. Puracé - Volatile flux estimates derived from SO2 flux daily averages (NOVAC Network)

23 Mar 17	4.7 (406)	2.4 (207)	0.9 (84)	0.5 (41)	0.1 (8.8)	0.04 (3.7)	0.02 (2.1)	0.01 (1.1)	(0.09)	(0.05)

Table 3. TV Fluxes

	H_2O **in kg s^{-1} (t d^{-1})**	**CO_2** **in kg s^{-1} (t d^{-1})**	**SO_2** **in kg s^{-1} (t d^{-1})**	**H_2S** **in kg s^{-1} (t d^{-1})**	**H_2** **in kg s^{-1} (t d^{-1})**
Nev. Del Ruiz	157 (13586)	23 (2017)	7.8 (672)	0.6 (52)	(3.4)
TVF	189 (16330), in kg s^{-1} (t d^{-1})				
Galeras	40 (3457)	30 (2600)	4.2 (365)	1.4 (119)	(0.7)
TVF	76 (6543), in kg s^{-1} (t d^{-1})				
Puracé	4.7 (406)	1.0 (84)	0.1 (8.8)	0.02 (2.1)	(0.09)
TVF	5.8 (502), in kg s^{-1} (t d^{-1})				

0

CHAPTER 5

Volcanic gas monitoring: a 3-year report on volcanic gas compositions and fluxes from the highly unstable Nevado del Ruiz (Colombia)

Abstract. This chapter reports on volcanic gas compositional time-series obtained at Nevado del Ruiz (Colombia) from 2017 to 2019. Daily acquisitions of volcanic gas plume composition through a permanent MultiGAS station installed near the summit of the volcano consistently recorded SO_2 concentrations above the instrument noise (>0.2 ppmv), but only about 23% of daily acquisitions recorded SO_2 levels ≥ 5 ppm. These yield CO_2/SO_2 averages of ~3.9 (SO_2 concentration > 5 ppm) and ~3.2 in plumes with SO_2 concentration > 10 ppm. Similarly, we estimate CO_2/SO_2 plume averages of 4.6 and 3.7 and 5.4 and 3.9 for 2018 and 2019, respectively. On the other hand, by averaging daily SO_2 outputs from the 5 operating NOVAC stations around the volcano, we estimate average fluxes of ~1847, ~2016 and ~2024 t/day for 2017, 2018 and 2019, respectively. These volcanic gas composition records support continuing near-surface lava extrusion and dome building, with predominantly SO_2-rich (H_2S/SO_2 ~0.01) gas emissions and typical magmatic H_2O/CO_2 average gas ratios of ~24 (2018) and ~27 (2019). The latter are estimated in acquisitions windows during which SO_2 concentrations were the highest (and plume signal was easiest to constrain) and therefore may be considered as degassing pulses associated with the shallow magma reservoir. Real-time volcanic gas data continues to be carefully analyzed and interpreted in a collaborative effort with local volcanologists and observatories to mitigate volcanic risk at Nevado del Ruiz volcano.

5.1. Introduction

Lon-term monitoring of volcanic systems provides crucial insights on their eruptive potential through studies of gas compositions and emission rates, thermal output, seismic unrest, or geodetic anomalies over timescales ranging from hours to years. The past decades have seen rapid improvements in gas monitoring capabilities, mostly thanks to technological advances (MultiGAS; Aiuppa et al., 2005; Shinohara et al., 2005) that allow measuring volcanic CO_2/SO_2 gas ratios at high temporal resolution to track pre-eruptive degassing of magmas, and interpreting and predicting transition from quiescence to volcanic eruption (Edmonds, 2008; Oppenheimer et al., 2014; Fischer and Chiodini, 2015).

These high temporal resolution gas measurements initially focused on Italian volcanoes, where the first permanent MultiGAS networks were installed (Aiuppa et al., 2009, 2010a, 2010b), and where a peculiar CO_2-rich magmatism (Métrich et al., 2004; Kamenetsky et al., 2007) makes gas CO_2/SO_2 ratios a particularly suitable monitoring parameter (Aiuppa et al., 2017). However, the approach has proven capable of detecting shifts in volcanic gas compositions also at predominantly CO_2-poor volcanoes, such as that occurring in the southern segment of the SVZ (CO_2/SO_2~1; Aiuppa et al., 2017). For instance, at Villarica (2847 m a.s.l.), the westernmost of three large

stratovolcanoes that trend NW-SW obliquely perpendicular to the Andean chain along the Mocha-Villarrica Fault, Zone, Aiuppa et al. (2017) showed that paroxysmal activity on March 3, 2015, was preceded by approximately one month of anomalously high CO_2/SO_2 ratios in the volcanic gas plume, recorded by a permanent MultiGAS stations installed on the volcano summit.

In the Andes, volcanic hazards can vary largely in nature and may include lava and pyroclastic flows, lahars, debris flows resulting from sector collapse, tephra falls, and others. A rhyolite explosive eruption of Cotopaxi at 4500 BP caused melting of the summit glacier, generating the largest known lahar in the Northern Volcanic Zone of the Andean Volcanic Belt. Similarly, on November 13, 1985, lahars generated by melting of the summit snow and ice cap during a relatively small eruption (VEI 3) of the Nevado del Ruiz volcano in Colombia produced the deadliest volcanic event recorded in the Andes, which is estimated to have killed more than 20.000 people (Thouret et al., 1990).

Currently, the Colombia Geological Survey (SGC) operates 3 volcano observatories across the country. The observatory located in Pasto, near the Ecuadorian border, monitors Galeras and other active volcanoes such as Cumbal and Azufral. Further north, in the Cauca region, the Popayán observatory is responsible for the monitoring of volcanoes in the central segment, such as Nevado del Huila, where in 2017 a system reactivation originated damaging mudflows that affected several neighboring communities, and Purace. The present work was developed in collaboration with the *Observatorio Vulcanológico y Sismológico* of Manizales (OVSM) that monitors Nevado del Ruiz and other volcanic centers in the northern segment.

Here we report on variations in volcanic gas compositions ratios measured in-situ using a permanent multi-component gas analyzer (MultiGAS) station and SO_2 fluxes measured by scanning differential optical absorption spectrometer (DOAS) from the NOVAC network, which then combined provide constrains on CO_2 degassing rates from 2017 to 2019 at Nevado del Ruiz.

5.2 Volcanological setting

Below the NVZ, 12-20 Ma Nazca oceanic lithosphere is being subducted at an angle of 31-45° at about a rate of 7 cm/yr and a dip of 25-30° (Gutscher et al., 1999a). Volcanic centers here are divided into north, central and south segments. Volcanoes in the northern and central segments are located in the Cordillera Central east of the central depression, while those in the southern segment, such as Nevado del Ruiz, also occur within the Cauca-Patria depression and in the Cordillera Occidental.

Nevado del Ruiz (4º50-55'N, 75º15-2O'W, ~5311 m a.s.l.) marks the beginning of Northern volcanism, following a break in subduction angle, which decreases to the north below the Bucaramanga flat-slab segment (see Fig. 3.1; Pennington, 1981; Hall and Wood, 1985; van der Hilst and Mann, 1994). Along another seven so far-identified volcanic centers, it is part of the Ruiz-Tolima volcanic zone, which is confined to the northern 90 km-long and 20 km-wide sectors of the NVZ. The Nevado del Ruiz volcano lies at the intersection of the *Palestina* fault system with the regional fault system (Perignon et al., 1988).

5.3. The evolution of the magmatic system of Nevado del Ruiz

The evolution of the Nevado del Ruiz Volcanic Complex is described in more detail in the following chapter. The present-day active volcano was built over the last 150,000 years, inside the older Ruiz summit crater or collapse caldera. In recorded history, Ruiz had two notable eruptive events. In 1595, three Plinian eruptions killed 636 people when a lahar swept down the nearby river valleys; and in 1845, mudflows flooded the upper valley of the *Lagunillas* River, killing more than 1,000 people. The modern volcano consists of a truncated cone with elongated lava flows projecting towards the northeast, west-northwest, and east-southeast. The summit appears flat and is covered by an ice cap. The highest dome (Farallon) on the northwest part of the summit overhangs the active Arenas crater that can be seen degassing in figures 5.1b and 5.1c.

5.3.1 The 1985 eruption

The chronology of the principal scientific and governmental actions in the leading up of the November 13, 1985 eruption of Nevado del Ruiz, Colombia were reported in detail by Hall (1990). It is relevant to note that the first indication of anomalous activity prior to the 1985 eruption was the intensification of fumarolic activity in the main Arenas crater. This was reported by the authors to have begun towards the end of November 1984, approximately one year before the catastrophic eruption of 13 November 1985. During that year, the reawaking of Nevado del Ruiz that first started with anomalously high gas emissions and increased fumarolic activity in the main crater, was followed by persistent seismic tremors, large gas columns, occasional phreatic eruptions, such as the one that occurred just two months prior to the eruption, on September 11 (Hall, 1990). Occasional ash could columns could also be seen prior to the main VEI 3 eruptive event that took place on November 13, 1985. Two explosive events followed by widespread ash-fall were reported initially on that day, just a few hours before the two major explosions that were accompanied by the formation of pyroclastic flows and lahars on the summit and upper flanks. As a result of this catastrophic event, lahars arrived in Armero on the *Rio Lagunillas*, overrunning the entire city of 35,000 inhabitants, and causing approximately 23,000 deaths.

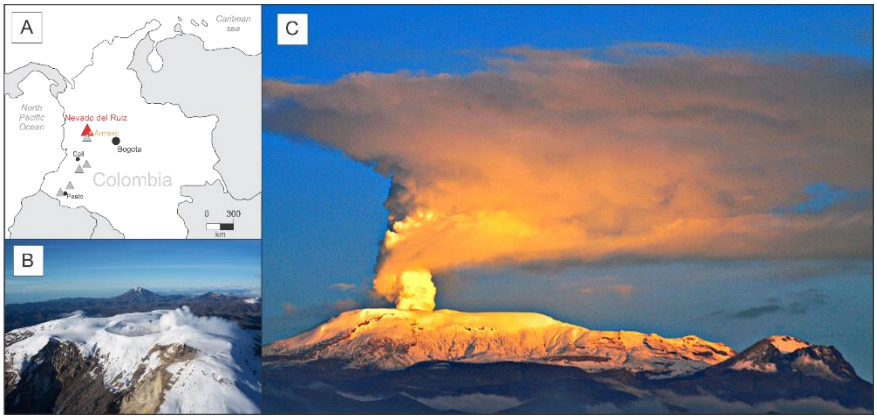

Figure 5.1: (a) Colombia map showing the location of the most active volcanoes in Colombia (in grey) and Nevado del Ruiz in red; in yellow the location of the city of Armero, destroyed in the 1985 eruption. (b) Arenas crater, Nevado del Ruiz. (c) vertical gas plume from Arenas crater, Nevado del Ruiz (photos are courtesy of Jhon Makario Londoño, SGC-OVSM)

5.3.2 Current activity

After the deadly lahars of November 1985 described above, the monitoring network was significantly implemented at Nevado del Ruiz. Until 1991, persistent volcanic activity at Nevado del Ruiz continued with intermittent ash emissions and significant seismic activity. This was followed by approximately 20 years of no explosive activity and/or ash emission reports. In September 2010, a significant increase in the number of seismic events lasted until early 2012 when volcanic activity level increased significantly. Through overflights and daily monitoring of the volcano, the local observatory reported an explosion on 22 February, long-period seismic events during March, and a dramatically increase between in SO_2 emissions between March and June 2012. Several ash emissions from the summit were observed during April-June 2012. An ash plume that rose to 11 km altitude on 29 May caused ash-fall in over 20 communities to the NW and closures at three nearby airports.

The five years that preceded the installation of the MultiGAS station were marked by persistent gas and ash emissions and continuous tremor. Although the weather in the region makes for difficult satellite observations, the local observatory (OVS Manizales) continuous to report columns of ash up to 1 km until today.

5.4. Methodology

Sulfur dioxide emissions from Nevado del Ruiz have been recorded daily since 2012 by scanning UV spectrometer systems installed through the Network for the Observation of Volcanic and Atmospheric Change project briefly described in the previous chapter (Galle et al., 2003, 2010). This network includes 5 different scanning locations, *Bruma* (4.899; -75.334, 4878 m a.s.l.), *Alfombrales* (4.877; -75.353, 4458 m a.s.l.), *Azufrado/Olleta* (4.893; -75.354, 4909 m a.s.l.), *Inderena/El Camion* (4.958; -75.366, 4016 m a.s.l.) and *Recio 3* (4.85883; -75.325472, 4665 m a.s.l.) that provide plume scans at virtually all wind directions (Fig. 5.2). The NOVAC scanning mini-DOAS (differential optical absorption spectroscopy; Johansson et al., 2009) instruments scan the sky continuously during daylight hours to measure the integrated absorption of UV light by SO_2 in the plume. These are then combined with meteorological information to derive daily statistics of total SO_2 emissions (see 4.3.3 for more details on measurement procedure). Plume height is either obtained from triangulation by two stations or it is assigned a fix height of 500 meters, based on average plume heights registered by the local observatory over the years. Effects of the variability of this parameter on our SO_2 flux dataset are discussed below. Wind speed and direction are acquired from local meteorological models from IDEAM (http://www.ideam.gov.co/). Daily SO_2 flux estimates were combined here with contemporarily obtained CO_2/SO_2 gas ratios (converted from molar ratios to mass based on concentration ratios) measured by a permanent gas monitoring station first installed in July 2017 (MultiGAS; see description below) to derive CO_2 flux budgets from 2017 to 2019.

Gas compositions were acquired daily by a permanent MultiGAS station (Aiuppa et a., 2005; Shinohara et al., 2005; see 4.3.1 for details on sensors and calibration procedures) installed at *Bruma*, on the southwest flank of the volcanic edifice (4.899; -75.334, 4878 m a.s.l.) The station was powered by lead batteries and solar panels, the operational of which was partially limited by constant cloud coverage and/or ash fall, despite the immense efforts by SVG-OVSM to routinely clean and maintain the exposed equipment. The inlet gas filter (1 µm) was protected from ash fall by a 30 cm-diameter funnel (Fig. 5.2).

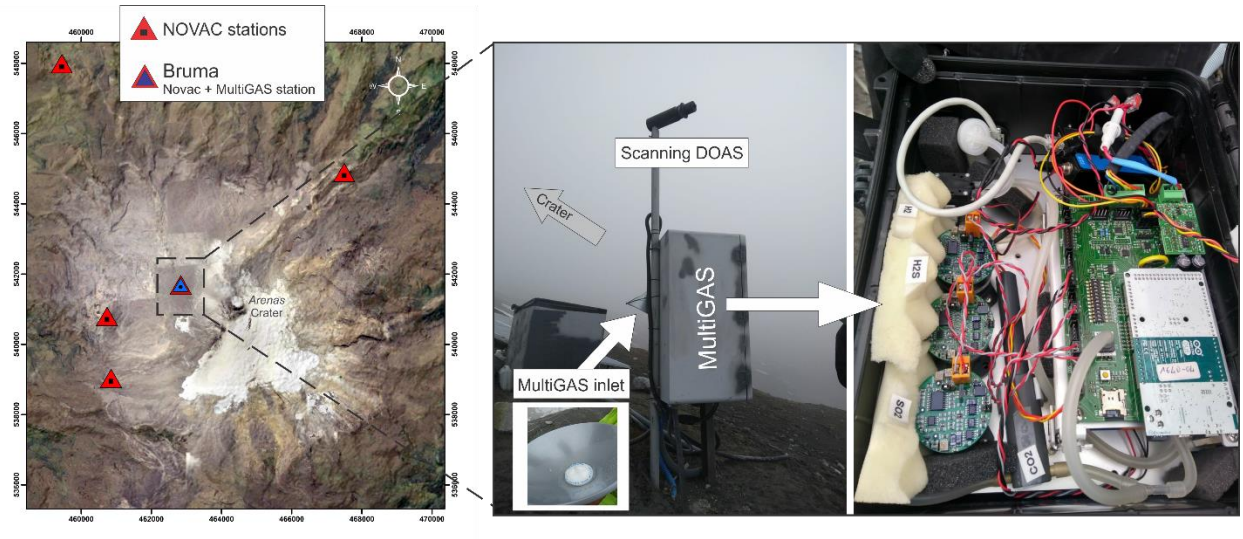

Figure 5.2: From left to right: Location of scanning NOVAC and MultiGAS stations around the Arenas crater at Nevado del Ruiz; Photo of Bruma (Nevado del Ruiz) showing the installed MultiGAS and scanning DOAS; Right, internal display of MultiGAS instrument showing the electric components of the gas sensing unit, including SO_2, H_2S and H_2 electrochemical sensors and CO_2 spectrometer.

In-plume gas data was acquired every 6 hours, for 30 minutes, at 0, 6, 12, 18 GMT. Each measurement was preceded by instrument warmup (3 min) and 2 min of ambient air flow to flush residual volcanic gas that remained trapped within the circuit, as described in the previous chapter. Inplume gas concentrations of SO_2, H_2S, CO_2, and H_2O were measured at 1 Hz frequency with data telemetered to *Observatorio Vulcanológico y Sismológico de Manizales* (OVSM) in near real time. Volcanic gas CO_2/SO_2 time series reported here, as well as molar x/SO_2 and H_2O/CO_2 were derived from linear regression through the concentration of volatile species in the plume and are independent on mixing with air (e.g., Aiuppa et al., 2007, 2009, 2014).

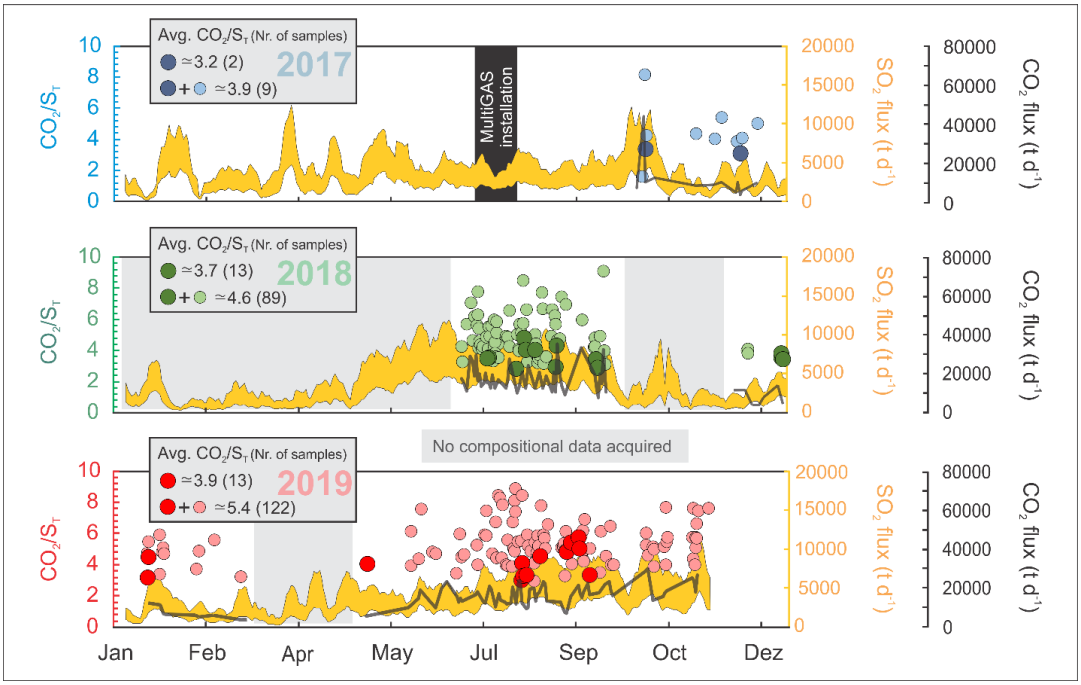

Figure 5.3: 2017, 2018 and 2019 NOVAC SO_2 flux time series in yellow represent maximum and average daily SO_2 flux values. Darker circles represent CO_2/S_T calculated from concentrated plumes (>10 ppm SO_2) whereas lighter symbols represent plumes with SO_2 concentrations comprised between 5 and 10 ppm. Dark like represents estimated CO_2 fluxes, from contemporary SO_2 flux values and CO_2/S_T ratios. Grey areas mark periods when the MultiGAS station was not operational.

5.5. Results and Discussion

5.5.1 Degassing dynamics and volatile output

We report here on SO_2 flux records (2017-2019) from 5 NOVAC stations around Nevado del Ruiz (Fig. 5.2). By averaging daily SO_2 outputs from the 5 operating NOVAC stations, we estimated average fluxes of ~1847, ~2016 and ~2024 t/day for 2017, 2018 and 2019, respectively (Fig. 5.3). Annual averages show small variations, especially between 2018 and 2019 (until October) when both data sets averages differ by only 8 t/day. Four out of 5 stations yield somewhat similar yearly averages ranging from ~2910 (*Bruma*) to ~4031 t/day (*Azufrado/Olleta*), thus attesting for the uninterrupted degassing and somewhat unvarying activity at *Arenas'* summit crater. The southern-most scanning station, however, show significantly lower SO_2 outputs, from ~901 t/day in 2017 to 1088 t/day in 2019. These may possibly contribute to significantly lower overall averages estimates for the 3-year window reported above, considering the discrepancy between flux outputs from this station and the other 4 station averages over the same observation period.

The SO_2 flux dataset that has been assembled over the years by the OVSM highlights a dependence on the wind patterns. Figure 5.3 shows that, between the months of May and October, the estimated plume direction is generally toward the west, allowing for ideal scanning geometries for 4 out of the 5 stations (located on the west side of the volcano). This ultimately translates into higher estimated fluxes comparing to periods during which the plume may become undetected in more than one scan (due to unfavorable transport directions).

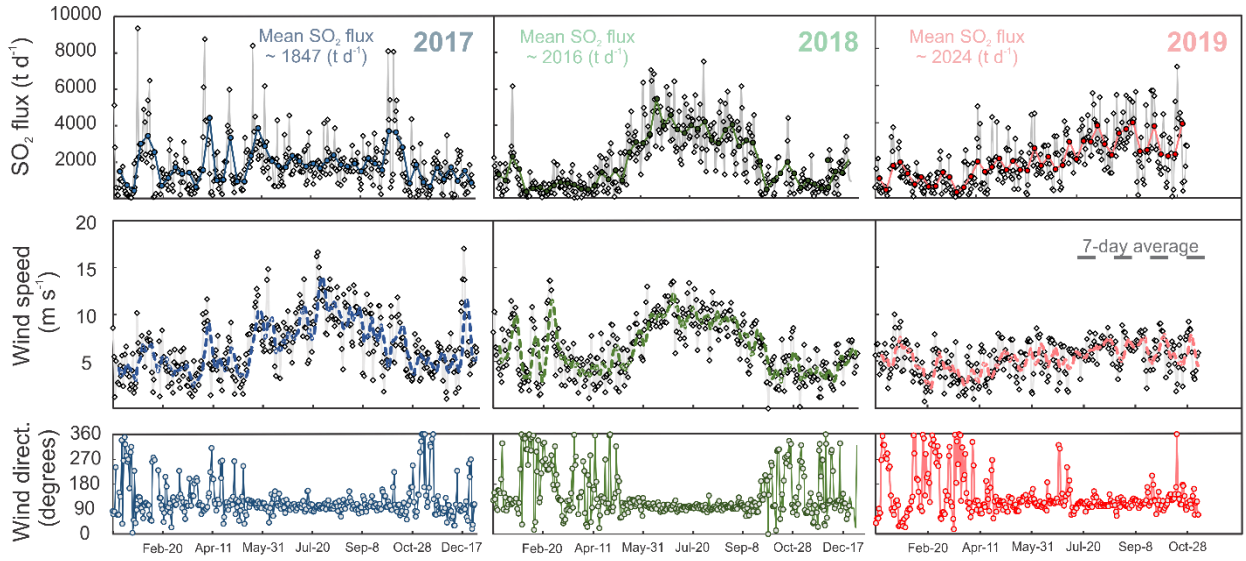

Figure 5.4: NOVAC SO_2 time years for the years 2017 (blue), 2018 (in green) and 2019 (in red). Dashed lines represent 7-day averages of the SO_2 flux and wind speed time series.

5.5.2. Plume volcanic gas compositions

Downwind in-plume volcanic gas compositions have been acquired every day since July 2017. We here report on results from July 2017 to October 2019 but focus in detail on the 2018-2019 period as 2017 results have already been described in detail in the previous chapter.

Apart from periods when the station was not fully operational (see previous sections), our dataset is also noticeably limited to days in which wind direction favored the southwest sector of the volcano, where *Bruma* is located. For instance, between 2018 and 2019, 1725 acquisitions (30-min each) were successfully transferred via telemetry from Bruma to OVSM, and subsequently processed at UNIPA. Approximately 67% of these acquisitions registered SO_2 concentrations above the instrument noise (>0.2 ppmv), but only about 23% recorded SO_2 levels ≥ 5 ppm (the minimum concentration threshold here considered above which the plume is sufficiently "dense" to allow for compositional and CO_2 flux estimates; Fig. 5.3). As briefly discussed in the previous chapter, aged plumes (~200 to 600 seconds; see previous chapter) are often a problem when it comes to atmospheric dilution and mixing, especially for species with high background concentrations such as CO_2 (~400 ppm in atmosphere).

Taking all the above into consideration, we successfully calculated a total of 9, 89 and 122 CO_2/SO_2 ratios in 2017, 2018 and 2019, respectively. Our average estimated CO_2/SO_2 ratios for 2017 are 3.9 (for plumes with SO_2 concentrations > 5 ppm; see Fig. 5.3) and 3.2 for plumes restricted to SO_2 concentrations > 10ppm (cat. III, see chapter 4). In the same order, we estimated CO_2/SO_2 plume averages of 4.6 and 3.7 and 5.4 and 3.9 for 2018 and 2019, respectively. After correcting for SO_2 interferences on the H_2S sensor's readings (~13%), the H_2S concentrations were consistently detected below 1 ppm and yielded H_2S/SO_2 ratios ranging from 0.01 0.04 in 2018 and 2019, confirming the nearly total absence of reduced S in the gas plume. Average H_2/SO_2 and

H_2O/SO_2 ratios were estimated at 0.13 and ~26, in plumes with SO_2 concentrations of ≥5 ppm. From these compositional measurements, we estimated a 2018-2019 averaged in-plume composition of 83.9 mol% H_2O, 12.3 mol% CO_2, 5.5 mol% SO_2, 0.1 mol% H_2S, and 0.8 mol% H_2 between (Table 5.1). Uncertainties in gas ratios measured by the MultiGAS are reported in table 7.1 and are far lower than the large variations reported in our time series.

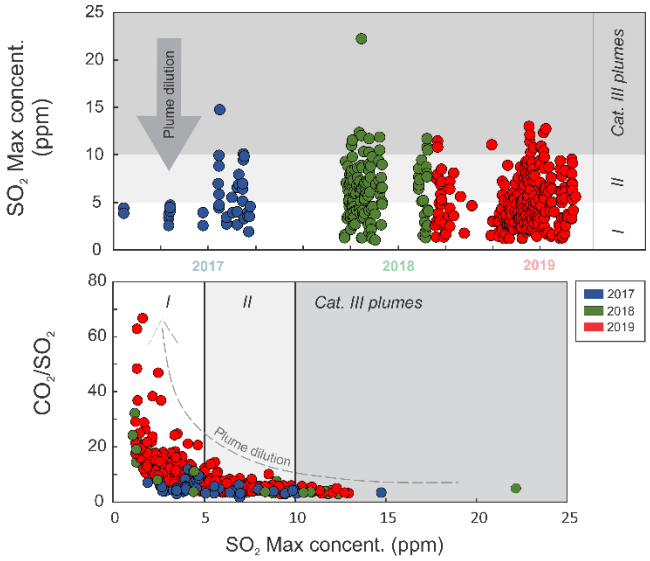

Figure 5.5: SO_2 plume concentrations and dependence of gas CO_2/SO_2 ratios on maximum SO_2 concentration measured by the MultiGAS instrument.

Table 5.1. Volcanic gas ratios and compositions from the Nevado del Ruiz plume (2018 – 2019).

2018	x/SO_2 molar ratios								Plume composition				
dates	CO_2	1σ	H_2S	1σ	H_2	1σ	H_2O	1σ	H_2O	CO_2	SO_2	H_2S	H_2
7 Aug	2.8	0.3	0.032	0.01	0.11	0.03	21.0	5.1	84.1	11.3	4.2	0.13	0.44
28 Aug	3.0	0.4	0.020	0.01	0.12	0.01	25.1	7.3	85.4	10.2	3.5	0.07	0.41
28 Aug	4.3	1.2	0.012	0.01	0.13	0.01	28.0	6.3	83.6	13.0	3.1	0.04	0.40
19 Sept	3.5	0.2	0.040	0.02	0.14	0.01	36.8	7.3	88.8	8.3	2.5	0.10	0.34
20 Sept	2.9	0.4	0.020	0.01	0.13	0.005	32.1	10.2	88.7	8.1	2.8	0.06	0.36
28 Dec	3.6	1.3	0.030	0.02	0.13	0.01	20.4	4.3	81.1	14.3	4.1	0.12	0.52
29 Dec	3.5	0.7	0.020	0.01	0.11	0.002	26.1	5.2	85.1	11.2	3.4	0.07	0.36

2019													
19 Jan	3.2	0.3	0.03	0.01	0.15	0.02	28.2	3.2	86.7	9.7	3.2	0.09	0.46
19 Jan	4.5	0.7	0.03	0.02	0.13	0.01	27.3	6.2	82.9	13.6	3.1	0.09	0.39
31 Jul	3.0	0.1	0.03	0.01	0.13	0.10	25.3	2.8	85.8	10.2	3.5	0.10	0.44
3 Aug	3.4	0.3	0.02	0.02	0.12	0.12	20.4	3.7	82.0	13.4	4.2	0.09	0.48
26 Aug	5.4	0.9	0.02	0.01	0.10	0.02	28.7	6.2	81.4	15.4	2.9	0.09	0.28
30 Aug	5.0	1.3	0.03	0.02	0.11	0.05	18.4	2.4	74.9	20.4	4.2	0.12	0.45

5.5.3. Shallow magmatic degassing during dome extrusion

From 2017 to 2019, volcanic gas compositions have consistently shown a near-total absence of sulfur as H_2S in the gas phase of the Nevado del Ruiz plume (Fig 5.6 A). This attests for the magmatic nature of volcanic gas emissions that have been registered at Nevado del Ruiz since 2015, when a series of unusual seismicity patterns, characterized by discrete episodes of short duration, revealed the ascent of new high-viscosity magma to the surface (SGC - OVS Manizales). Our volcanic gas composition records supports persistent near-surface magma degassing, perhaps sustained by continuous lava extrusion and dome building, discharging a predominantly SO_2-rich (H_2S/SO_2 ~0.01) gas with typical magmatic H_2O/CO_2 (average) gas ratios of ~24 (2018) and ~27 (2019; Fig. 5.6b). The latter ratios were estimated in acquisition windows during which SO_2 concentrations were the highest (and, consequently, the plume signal was easiest to resolve from background), and therefore may be considered as representative of degassing from a shallow magma reservoir, as described above.

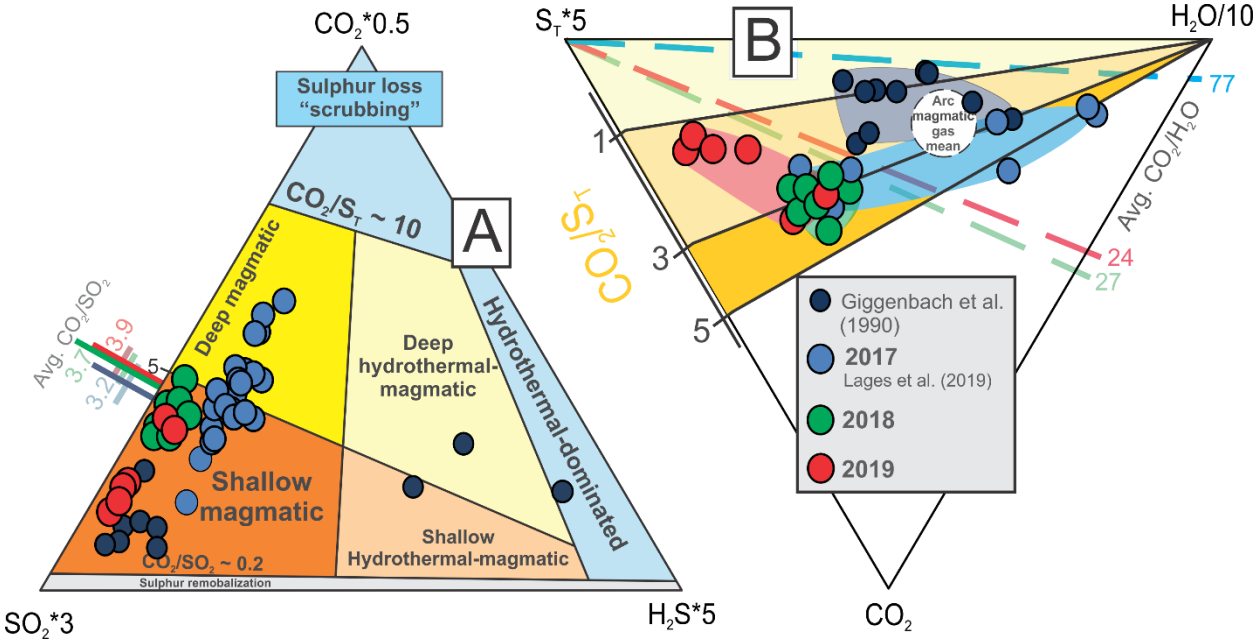

Figure 5.6: (a) Ternary diagram of SO_2*3-CO_2-H_2S*5 showing the magmatic gas nature of Nevado del Ruiz gas; (b) Ternary diagrams showing normalized gas composition for Nevado del Ruiz (2018 – 2019). The 2019 is the least hydrous and most H_2S-poor, and thus the most magmatic in nature.

5.5.4. Significance of CO_2 flux measurements

Our long-term observations of degassing patterns at Nevado del Ruiz suggest that the NOVAC network captures substantial intra-daily and seasonal oscillations in SO_2 outgassing. We caution that the SO_2 (and, indirectly, CO_2; Fig. 5.7) budgets described (Fig. 5.4) are obtained by simply averaging daily NOVAC outputs from 5 stations, while the dataset presented in the previous chapter 4 was based on more accurate post-processing of daily spectra information (see 4.3.3. for details on post-processing procedures).

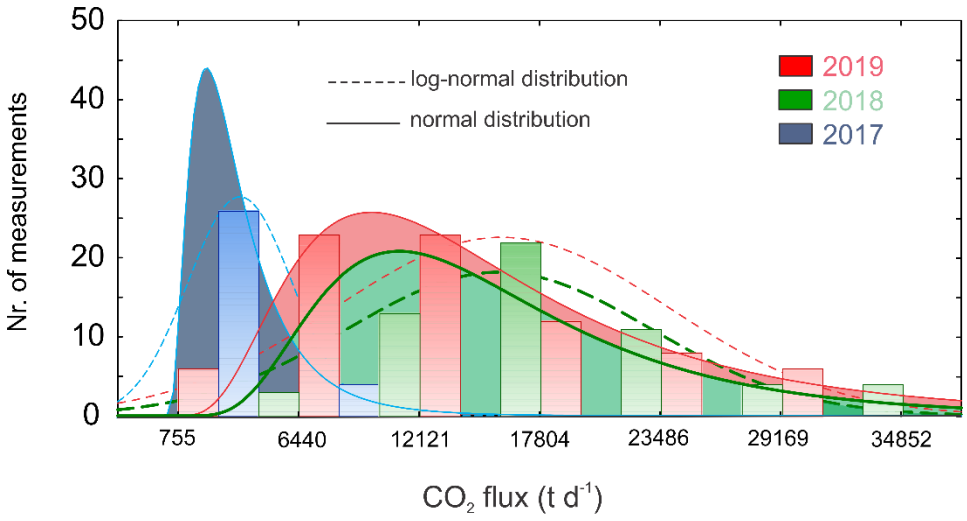

Figure 5.7: CO_2 flux range distributions for the 3 years here reported (2017-2019). Log-normal distribution and normal distribution of CO_2 fluxes are given as comparison.

One major difference between the two methods is the assumed plume heights assigned to each daily flux estimate. In the post-processed results of Chapter 4, plume height was derived from triangulation using two or more stations, whereas data reported in this chapter are based on using a fixed plume height of 500 m (this "typical" plume height is based on long-term observations by the local observatory). This, in addition to uncertainties in derived plume speeds, may be one of the contributing factors to the significant differences between automatic (observatory-based, this chapter) and reprocessed (Chapter 4) SO_2 flux estimates for 2017 (Fig. 5.8). A comparison of the two datasets (2017 to June 2018; the period over which rigorous post-processing was carried out), demonstrates relative differences normally between 50 and 100%, with the automatic SO_2 flux data generally overestimating the more solid reprocessed dataset (Fig. 5.8).

With these limitations in mind, we yet conclude that our first-order SO_2 flux estimates are accurate enough to allow resolving changes in degassing regime on a multi-year basis (Fig. 5.7). We show in particular, that the 2018-2019 CO_2 fluxes are statistically higher than the 2017 fluxes, which may indicate increasing supply of deeply sourced magma/gas to the shallow plumbing system. This observation needs to be critically tested and eventually confirmed by additional monitoring in the years to come.

5.5. Conclusion

Geochemical monitoring of volcanic gas emissions as precursors to eruptions remains a difficult task. Establishing extensive time series (years) of volcanic gas compositions can help in the interpretation of degassing patterns and provide crucial information on the transition between

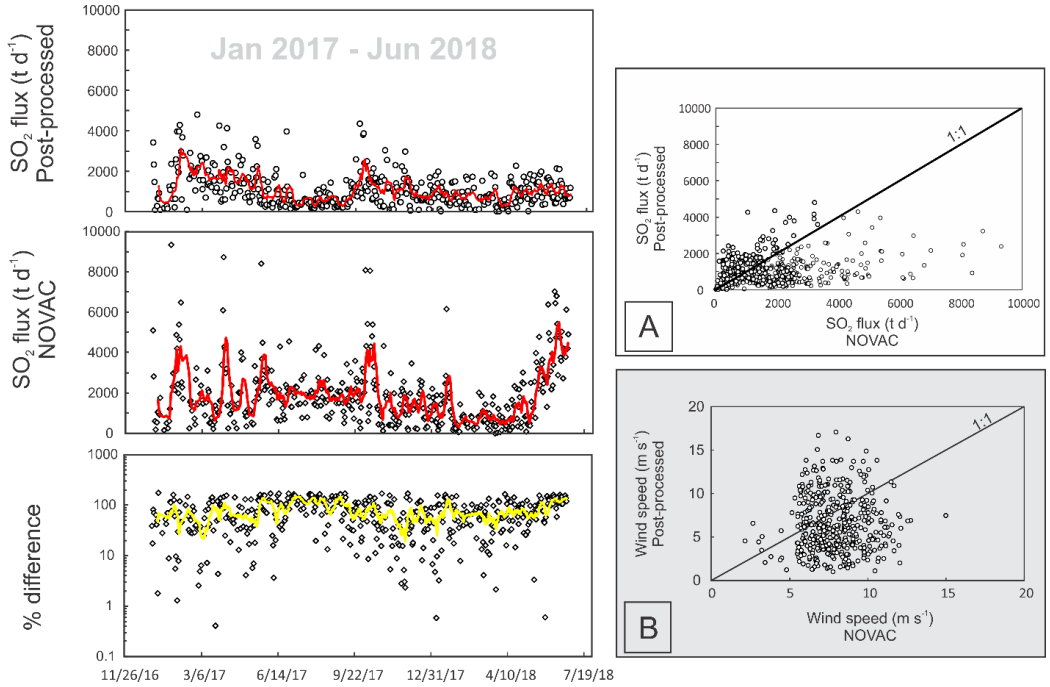

Figure 5.8: Comparison between SO_2 flux data filtered from the NOVAC network following the procedures described in Chapter 4 and daily NOVAC SO_2 flux outputs. Red and yellow lines represent 7-day averages in the dataset.

prolonged quiescent to periods of volcanic unrest leading up to major eruptions. This is particularly important for highly hazardous volcanoes, such as Nevado del Ruiz, where past eruptions have destroyed entire neighboring communities.

The dataset presented here attests for continuous unrest of Nevado del Ruiz volcanic system since 2015 and provides clear evidence for shallow magma continuously feeding volatiles to the surface via the *Arenas* summit crater. Risk associated with near-crater areas remains high, which presented this study with the challenge of monitoring the volcanic plume from afar. Furthermore, data reported here provides crucial background of volcanic gas compositions and volatile fluxes for this volcanic system during a period of continuous seismic unrest and occasional ash emissions, which may be foresee periods of higher volcanic unrest.

Throughout this investigation, we demonstrate that the automatically processed SO_2 flux data shared through the NOVAC network, while successfully resolving major shifts in volcanic degassing rates, may possibly lead to overestimating SO_2 (and indirectly CO_2) fluxes. Nonetheless, the high SO_2 (far higher than any other actively degassing volcano in the Andean Volcanic Belt) and CO_2 (confirmed by the robust CO_2/SO_2 dataset here reported) 2018-2019 emissions compare well with, or are even higher than, the previously reported 2017 results (Lages et al., 2019; see chapter 4 of this dissertation), and confirm Nevado del Ruiz has one of the strongest arc volatile sources worldwide.

5.5.1 Implications for hazard detection

The Nevado del Ruiz *Arenas* crater has been strongly degassing since 2015, providing the opportunity for acquisition of robust time series of both plume compositions and volatile fluxes. These, extensively discussed throughout this chapter, can provide insightful information on changes of the volcanic system over time. Above all, this dataset aims at contributing to an improvement volcanic hazard assessment and risk mitigation associated with Nevado del Ruiz. To do so, further work on quantitatively modelling shifts in volcanic emission rates and compositions needs to be developed, in order to better interpret the nature of the variations in extensive volcanic gas time-series. Nonetheless, we believe that the volcanic gas monitoring network developed over the past 3 years is greatly contributing to monitoring of one of the most hazardous volcanoes in the Andean Volcanic Belt, as real-time gas composition data continues to be carefully analyzed and discussed with local volcanologists and observatories.

5.6. Acknowledgments

This investigation has been made possible through the collaboration between the University of Palermo and the *Servicio Geológico Colombiano - Observatorio Vulcanológico y Sismológico de Manizales* to which we are deeply grateful for their continuous logistical and scientific support throughout. Initial funding for producing the NOVAC data set here presented was provided by the European Commission FP5 (DORSIVA project) and FP6 (NOVAC project), and the operation of the NOVAC network is funded through initiatives of the Volcano Observatories and support from

the Volcano Disaster Assistance Program of the United States Geological Survey (SGS). We would also like to acknowledge the crucial support from the Alfred P. Sloan Foundation (Deep Carbon Observatory/DECADE project; UniPa-CiW subcontract 10881- 1262) and the MIUR (under grant PRIN2017-2017LMNLAW) for funding the field work portion of this work.

CHAPTER 6

Noble gas systematics of the Northern Volcanic Zone arc volcanism from Fluid Inclusions in minerals

Abstract. Trace volatiles like He are key for understanding the lithospheric mantle signature and the complex role of subduction in global geochemical cycles, as well as fluid migration processes governing Noble gas compositional patterns along volcanic arcs. Here, we report on noble gas abundances and isotope signatures of eruptive products from five of the most active volcanoes along the Northern Volcanic Zone (NVZ), as well as updated fumarolic gas data for Galeras (Colombia). Fluid inclusions in olivine phenocrysts from Reventador, Cotopaxi and Tungurahua yield $^{3}He/^{4}He$ (R_C/R_A) values of 7.0-7.4 R_A, within the range of Mid-Ocean Ridge Basalt (MORB, 8±1 R_A) and consistently higher than those of cogenetic orthopyroxenes with lower gas contents (most possibly due to mass-dependent-driven isotope fractionation) and those of free gases previously reported in literature. Mafic olivine phenocrysts from old fissure lavas analyzed for Nevado del Ruiz also yield the highest ever measured $^{3}He/^{4}He$ (8.5 R_A) at this volcano, which is in the range of fumarolic gas data for Galeras (previously reported as high as 8.8 R_A and here measured to a maximum of 8.3 R_A). Therefore, our dataset shows a substantial discrepancy between the consistently measured isotope signature of eruptive products from the Ecuadorian arc segment (~7.2 R_A) and values reported for the Colombian part of the NVZ (~8.5 R_A). Previous studies into whole-rock trace element of lavas erupted from these volcanic centers suggest minor variations along the main magmatic arc. Instead, this study proposes that significant disparities in crustal thickness (from <35 km at the northern-most part of the segment, to >50 km at the Ecuadorian arc segment) may factor largely into the variability recorded on our data set. Therefore, melting and/or assimilation of crustal lithologies (U- and Th-rich) may be the predominant process of contamination of MORB-like fluids at volcanic arc settings characterized by exceptionally thick continental crusts.

6.1. Introduction

Due to their inert behavior and large isotope ratio variability among the different Earth's reservoirs, noble gases such as He, Ne and Ar have long been considered optimal tracers of complex migration processes of magmatic fluids from the Earth's mantle to the atmosphere, hydrosphere and crust (e.g., Porcelli and Wasserburg, 1995a; Farley and Neroda, 1998; Ozima and Igarashi, 2000; Porcelli et al., 2001; van Keken et al., 2002; Ballentine et al., 2002; Moreira, 2013). These volatiles can be primordial in origin, trapped in the mantle since planetary accretion, produced in-situ, or they may be recycled, re-injected into the mantle via material originally at the surface through the subduction process (e.g., Jackson et al., 2013; Kobayashi et al., 2016; Smye et al., 2017). Seismic tomography studies point out that oceanic plates can be subducted well below the 670 km discontinuity down to the core-mantle boundary (e.g., van der Hilst et al., 1997; Bijwaard and Spakman, 1998; Fukao et al., 2001), and numerical modelling of mantle convection patterns (van Keken and Ballentine, 1999) cast doubt upon the likelihood of maintaining a deep region of the mantle isolated over geological timescales. Studies of noble gases transport into the mantle along subduction arcs have shown $^{3}He/^{4}He$ isotope variations ranging from 10.1 to 0.01 Ra (Hilton et al., 2002; Sano and Fischer, 2013). While $^{3}He/^{4}He$ > 9.5 Ra reported by Jean-Baptiste et al. (2016)

in Vanuatu has been attributed to the contribution of the incipient plume at the westernmost edge of the Pacific super-plume (Montelli et al., 2006), $^{3}He/^{4}He$ << Mid-Ocean Ridge Basalt (MORB, 8±1 R_A, Graham, 2002; Graham et al., 2014) are either a result of (i) the subducted slab component, including the altered oceanic crust, oceanic sediment and basement; (ii) shallow derived He resulting from interactions between the rising magma and the continental crust overlying the volcanic arc (Sano and Wakita, 1985a; Sano and Fischer, 2013); and/or (iii) the influence of continental crust subducted beneath volcanic arcs (e.g., Southern Italy; Hilton et al., 2002).

It is therefore crucial, in order to access along-arc variations in MORB-type $^{3}He/^{4}He$ ratios, to account for space, time, and nature variability of available samples. The geographic control on $^{3}He/^{4}He$ signatures has been attributed two either magma aging or interaction with surrounding country rock (e.g. Marty et al., 1989; Hilton et al., 1993a; Van Soest et al., 1998; Notsu et al., 2001), as both processes can contribute with the addition of the radiogenic helium component to mantle-derived melts and therefore decrease $^{3}He/^{4}He$ (<< MORB), such as those observed in hydrothermal fluids. We must also consider that the use of standard sampling techniques for noble gas extraction from high-temperature fumaroles requires direct access, often out of reach depending on different risk assessments at hazardous volcanic areas. In other cases, instead, surface manifestations of volcanic gas emissions are inexistent. Several studies have attributed the occurrence of hydrothermal areas surrounding the main volcanic centers to the geometry and extension of its plumbing system that may partially dominate the interactions between the heat source at depth (magma) and shallow aquifers and groundwater.

In addition to the geographically-controlled intra-variability on $^{3}He/^{4}He$ signatures around individual volcanic centers, time-dependent He isotope mixing between primitive and more radiogenic end members appears to be common in many active volcanoes (Sano and Fischer, 2013). In fact, there are several examples worldwide that testify on temporal fluctuations in $^{3}He/^{4}He$ that correlate well with changes in volcanic activity, including Mt. Etna (Caracausi et al., 2003; Rizzo et al., 2006; Paonita et al., 2012, 2016) and Stromboli, in Italy (Capasso et al., 2005; Rizzo et al., 2009, 2015a), Mount Ontake, in Japan (Sano et al., 2015), Santorini, in Greece (Rizzo et al., 2015b), and Turrialba, in Costa Rica (Rizzo et al., 2016). This attests that He isotope signatures measured at the surface might be affected by processes happening deep in the magma chamber, such as the input of new magma prior to periods of higher levels of volcanic activity. For all the above, and due to the fact that some arc volcanoes remain unsampled to date, mostly due to their remote location, inaccessibility, or high level of volcanic activity, arc-scale studies of noble gas compositional trends (Hilton et al., 2002; Sano and Fischer, 2013) have fallen short of conclusive, especially due to the impossibility of a systematic approach derived from the widely heterogeneous data sets existing to date. Nonetheless, despite the limitations of global reviews to establish a consistent and coherent noble gas data base for arc-related volcanism, mostly due to the factors discussed above, Hilton et al. (2002), Sano and Fischer (2013), Oppenheimer et al. (2014) and Mason et al. (2017) argue that arc-scale correlations between isotope tracers do provide evidence of slab and crustal contributions to volatile emissions through arc volcanism.

This investigation provides new information on the nature of such correlations and discuss the processes governing significant along-arc variations in noble gas compositions. Moreover, here we attempt to improve the Northern Volcanic Zone current database and report on new noble gas data constrains on the magmatic sources of Tungurahua, El Reventador and Cotopaxi (Ecuador), and Galeras and Nevado del Ruiz (Colombia), five of the most active volcanoes in the entire Andean Volcanic Belt.

6.2 Geodynamic and geological setting

The Andes are a continental volcanic arc formed by the subduction of the Nazca Plate 12-20 Ma aged slab (Jarrard, 1986) beneath the South American Plate at a rate of about 56 mm/yr (Trenkamp et al., 2002). This volcanic chain extends for over 7000 km along the western margin of South America, and volcanism there occurs in four separate regions, the Northern (NVZ), Central (CVZ), Southern (SVZ), and Austral (AVZ) Volcanic Zones. The Northern Volcanic Zone (Ecuador and Colombia) is defined by a narrow volcanic arc (Fig. 1) located above the Benioff zone that clearly defines a steep subduction slab (Ojeda and Havskov, 2001) that exhibits lateral variations in the dip angle, from ~20°-35° north of the Carnegie Ridge (Pennington, 1981) to ~25° beneath Ecuador (Guillier et al., 2001). The flatter subduction angle causes the volcanic arc in Ecuador to widen and split into two cordilleras, the Western Cordillera and the Eastern Cordillera, dominated by dacitic and andesitic products, respectively (Hall et al., 2008; Hall and Mothes, 2008). Instead, active volcanism in Colombia generated the andesitic magmas that form the aligned active volcanic centers located along the Central cordillera, and the Cenozoic intrusions at both Central and Western Andean Cordilleras, as well as the Cauca-Patia graben.

6.3. Petrological and eruptive background

Volcanic arc trenches such as the Ecuador-Colombia Trench (ECT) originate from variable inputs from the partial melting of the subducting slab, subducted sediment input, the overlying mantle, and the continental crust (Hickey et al., 1986; Hildreth and Moorbath, 1988; Tatsumi, 1989). The Andean Volcanic Belt (AVB) represents one of the most famous examples of the formation of andesites along continental margins. However, it has been shown experimentally (Nicholls and Ringwood, 1972; Mysen et al., 1974) and with natural samples (Reubi and Blundy, 2009) that the majority of andesites are not primary melts. Instead, andesitic magmas form as the product of differentiation processes such as fractional crystallization, crustal assimilation and magma mixing. These processes not only impart chemical and textural signatures on the resulting lavas and eruptive products (Panter et al., 1997; Schiano et al., 2010; Garrison et al., 2011; Lee and Bachmann, 2014), but can also alter in various degrees the isotope signature of deeply degassing, uncontaminated magmas.

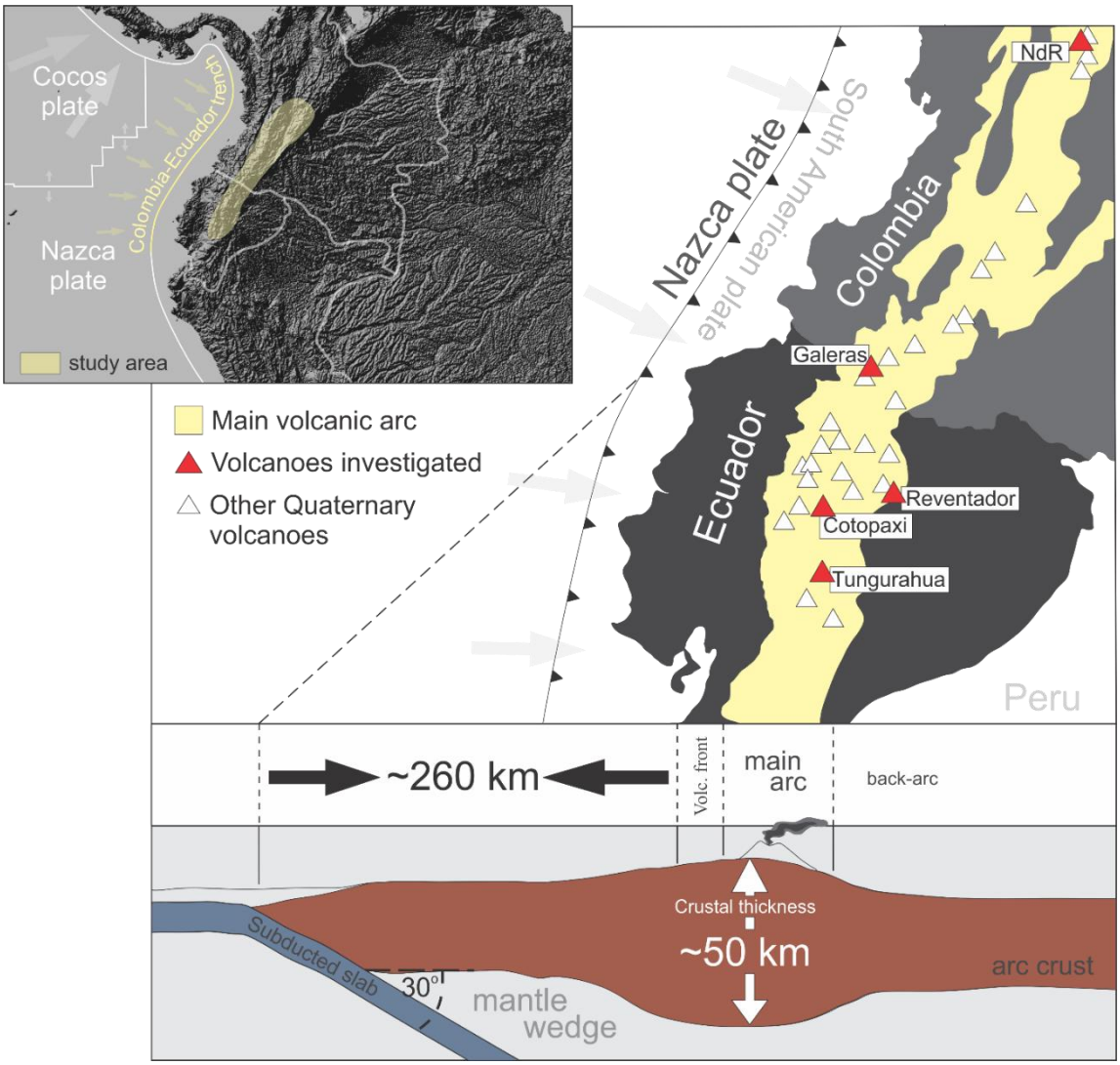

Figure 6.1: On the left: geological setting of the Northern Volcanic Zone (adapted from Bryant et al., 2006), showing the distribution of Quaternary volcanoes along the main magmatic arc (in light yellow). Volcanoes included in this study are highlighted in red. On the upper left corner, arrows indicate the subduction direction of the Nazca and Cocos tectonic plates, overlapped on 50-meter resolution DEM map. Average dip angle of 30° for the subducting slab is from Guillier et al. (2001), and crustal thickness data (50 km) is a minimum value proposed in previous studies by Prévot et al. (1996) and Guillier et al. (2001) for the Ecuador segment.

6.3.1. Colombia

6.3.1.1. Nevado del Ruiz

The Nevado del Ruiz Volcanic Complex (NRVC) is located in the department of Caldas, central Colombia, near the northern end of the Northern Volcanic Zone (Thouret et al., 1990). The NRVC history can be subdivided into four main eruptive stages: (i) the PRE-Ruiz Eruption (~1.8 - 0.97 Ma); (ii) the First Ruiz Eruption that occurred ~0.2 Ma; (iii) The Intermediate Ruiz Eruptive Period that corresponds to the formation of resurgent lava-domes and minor eruption centers near to the

caldera ring; and lastly (iii) the Second Ruiz Eruptive Period, that included effusive-to explosive activity. A summit caldera, formed around the end of the second eruptive period, has now been filled by numerous composite lava domes that characterize the present-day Nevado del Ruiz. Over the past 11 ka years, this volcano has explosively erupted andesitic to dacitic magmas, with lavas and pyroclastic flows restricted to an andesitic to dacitic compositional range (about 40% dacites and 60% andesites; Vatin-Pérignon et al., 1990). Despite the complex eruptive history of this volcanic complex, its geochemical evolution suggests a common magmatic source over time (see Vatin-Pérignon et al., 1990). In this study we focused on the Fissure lavas of *La Esperanza*, located in the northern-most sector of the volcanic complex, a segment believed to be structurally controlled by the *Villamaría–Termales* fault system (Martínez et al., 2014). Due to their stratigraphic placement and apparently moderate glacial involvement this unit has been estimated at ~0,035 – 0,045 Ma. It is, however, unclear if these lavas belong to the Intermediate period, or instead are one of the oldest formations of the Second Eruptive period. The presence of olivine microphenocrysts within microcrystalline-microlytic to moderately intergranular textures, clearly distinguishes these lavas from the majority of the eruptive periods of the volcanic complex. It is estimated that mafic minerals make up to 80% of these lavas, while the estimated average of other eruptive products from CVNR is between 25% and 45%, with feldspar being the most predominant overall (Vatin-Pérignon et al., 1990; Martínez et al., 2014).

6.3.1.2. Galeras

The Galeras Volcanic Complex (GVC) is located approximately 60 km north of the Colombia-Ecuador border. Over the past 1 Ma it has been characterized by caldera-forming eruptions, followed by the construction of new active cones that produced lavas and pyroclastic flows, ranging from basaltic-andesites to dacites (Calvache and Williams, 1997a and b). Its Holocene active cone lies on the eastern side of the volcanic complex, and produced the basaltic-andesite products here considered for analysis and that have been interpreted as possible fissure lavas (Calvache, 1990) that extend for an average length of 1.8 km. Plagioclase and Pyroxene are the main mineral phases in these lavas, but fresh olivine is common (Calvache, 1990). Considering the location of the lava flow outcrops, the author argues that these lavas may have erupted with a high effusion rate in order to travel such long distances. Their well-preserved morphology suggests an approximate age between the pyroclastic flow deposits of 1100 yBP and the major eruption of 1866.

6.3.2. Ecuador

6.3.2.1. El Reventador

A large sector collapse around 19,000 yBP left a prominent 4 km-wide caldera (Aguilera et al., 1988) at El Reventador. Since then, a young, symmetrical, 1 km-high volcanic cone has grown in this amphitheater and is one of the most active volcanoes in the Ecuadorian Andes. After 26 years of quiescence, El Reventador initiated a new period of intense volcanic activity starting with a sub-Plinian event in November 2002 that produced two lava flows effusively emplaced over a two-

month period that followed the reactivation of the system (Samaniego et al., 2008). Petrological analysis of products from the 2002 eruption suggests that there was a single pre-eruptive reservoir with a top at 8 ± 2 km and a base at 11 ± 2 km (Ridolfi et al., 2008; Samaniego et al., 2008). The same authors reported on the geochemical and mineralogical characteristics of the 2002 and later-emplaced 2004-2005 lava flows and inferred silica contents for these products ranging from 53.5 to 62.1 wt.%. The activity persisted over the years and continues to this day. The basaltic andesites to andesites, medium-high K 2009 lava flows analyzed in this study are similar to the compositions reported for the initial 2002 eruptive products (porphyritic, ~25 – 30 vol.% phenocrysts in pyroclastic blocks and ~40 vol.% in lava flows), with a mineral assemblage composed of plagioclase, clinopyroxene, orthopyroxene, amphibole, magnetite, with scarce olivine (Samaniego et al., 2008).

6.3.2.2. Cotopaxi

Cotopaxi, a stratovolcano located ~60 km south of Quito, has exhibited a history of bimodal volcanism, where rhyolitic and andesitic magmas erupt in quick succession, from the same conduit, displaying very limited intermingling (Hall and Mothes, 2008). This alternation between andesitic and rhyolitic periods of activity, without intermediate dacitic products (Garrison et al., 2011), produced the younger flows of Cotopaxi IIB, a series of andesitic scoria falls, lava flows and a single rhyolite eruption. Each eruption cycle has been characterized by a similar eruptive pattern, involving plinian scoria or pumice tephra falls, scoria or pumice pyroclastic flows, blocky-lava flows, and widespread debris flows. From the end of the Colorado Canyon episode 4,000 years ago until the present, Cotopaxi has experienced a continuous series of periodic eruptions, all of which have involved andesitic magmas, with 57–62% SiO_2 (Hall and Mothes, 2008) and phenocryst assemblages that include plagioclase, hypersthene, augite, magnetite, and rare olivine. In the lavas from Cotopaxi IIB olivine is occasionally present in trace amounts, but increases up to 2% (Hall and Mothes, 2008) in the youngest rocks here considered for analysis.

6.3.2.3. Tungurahua

Tungurahua is a stratovolcano located in central Ecuador. Historical records (Martinez, 1932) and chronological data of the eruptive products of Tungurahua (Hall et al., 1999; Le Pennec et al., 2008) reveal that regional tephra fallouts, pyroclastic flows and related debris flows, characterized most eruptions in recent times and blocky lava flows. A recurrence rate of at least one pyroclastic flow-forming eruption per century was for the last millennium, ranking Tungurahua amongst the most active volcanoes of the Northern Andes (Le Pennec et al., 2008). More recent eruptive products, such as pyroclastic flows tephra deposits and lavas have andesitic compositions (58–59 wt% SiO_2; Samaniego et al., 2011) and contain plagioclase (5–15 vol.%), clinopyroxene (2–4 vol.%), orthopyroxene (2–4 vol.%), and magnetite, with trace olivine. This is similar to compositions reported by Samaniego et al. (2011) for the 2006 juvenile blocks from the pyroclastic flow deposits analyzed in this study, which are dark, vesicular, porphyritic (~10–20 vol.% phenocrysts) andesites (57.6–58.9 wt.% SiO_2) and are composed of similar mineral assemblage.

6.4. Methods and analysis

6.4.1 Noble gases in Fluid Inclusions

The element and isotope compositions of He, Ne, and Ar were measured in fluid inclusions (FIs) hosted in the olivine and orthopyroxene phenocrysts at the noble gas laboratory facilities at the *Istituto Nazionale di Geofisica e Vulcanologia* (*INGV*) in Palermo. For olivine and orthopyroxene crystal separation (0.25 to 0.50 mm fractions) from lavas and scoriae layers from Nevado del Ruiz, Galeras, El Reventador, Cotopaxi and Tungurahua, we used sodium polytungstate (SPT) heavy liquid. The individual crystals were then carefully handpicked under a binocular microscope and cleaned in multi-stage ultra-sonic baths (e.g., Di Piazza et al., 2015). For the analysis, the samples were placed inside stainless-steel bowls and loaded onto the crusher. Noble gases trapped inside FIs were released by in-vacuo single-step crushing, which minimizes the contribution of cosmogenic ^{3}He and radiogenic ^{4}He possibly trapped in the crystal lattices (e.g., Hilton et al., 2002). Gas released from the mechanical fragmentation of crystals was cleaned in an ultra-high-vacuum purification line. Helium (^{3}He and ^{4}He) and Ne (^{20}Ne, ^{21}Ne, and ^{22}Ne) isotopes were measured separately by two different split-flight-tube mass spectrometers (Helix SFT-Thermo). The $^{3}He/^{4}He$ ratios are expressed in units of R/R_A (where R_A is the $^{3}He/^{4}He$ of air; 1.39×10^{-6}). The analytical uncertainty of He-isotope ratio measurements (1σ) was <4%, except for the pyroxene from Cotopaxi whose uncertainty is 13.5%. The R/R_A values were corrected for atmospheric contamination based on $^{4}He/^{20}Ne$ (e.g., Sano and Wakita, 1985) and are reported throughout as R_C/R_A values. The analytical uncertainty of the Ne-isotope ratio (1σ) was <1.7% and <4.6% for $^{20}Ne/^{22}Ne$ and $^{21}Ne/^{22}Ne$, respectively. The reported values of both Ne-isotope ratios are corrected for isobaric interferences at m/z values of 20 ($^{40}Ar^{2+}$) and 22 ($^{44}CO_2^{2+}$; Rizzo et al., 2018). Ar isotopes (^{36}Ar, ^{38}Ar, and ^{40}Ar) were analyzed by a multicollector mass spectrometer (GVI Argus) at an analytical uncertainty of $^{40}Ar/^{36}Ar$ <0.5%. A pre-purified air standard subdivided in tanks was used for He, Ne, and Ar elemental and isotopic recalculations. The analytical reproducibility of ^{4}He, $^{3}He/^{4}He$, $^{20}Ne/^{22}Ne$, $^{21}Ne/^{22}Ne$, and ^{40}Ar of standards were <2.4%, <2.6%, <0.4%, <0.5%, and <2.4%, respectively. These values represent the standard deviation of measurements made during >1 year of analyses for He and Ne and ~4 years for Ar, in the same source setting conditions. Typical blanks for He, Ne, and Ar were $<10^{-15}$, $<10^{-16}$ and $<10^{-14}$ mol, respectively. Further details on sample preparation and analytical procedures are available in Di Piazza et al. (2015) and Rizzo et al. (2018).

6.4.2 Dry fumarolic gas sampling and Noble gas isotope analysis

Dry gas samples for the analyses of He, Ne, and Ar were collected in the flanks of the active central crater of Galeras on 14 July 2017. Fumarolic gas from the two steaming vents (of temperatures of 91.3 and 87.5°C) was collected in two-way Pyrex bottles with vacuum valves at both ends. Despite the apparent weak flux and in-situ low temperatures (close to boiling) measurements, the gas was channeled through a stainless-steel tube and propelled several times through the sampling circuit in order to eliminate any possible remains of atmospheric components within the lines.

The concentration and isotope compositions of He, Ne and Ar in fumaroles were measured by admitting the gases into three distinct ultra-high-vacuum (10^{-9}–10^{-10} mbar) purification lines, in which all of the species in the gas mixture, except noble gases, were removed. Prior to the analysis, He and Ne were separated from Ar by adsorbing the latter in a charcoal trap cooled by liquid nitrogen (77 K). He and Ne were then adsorbed in a cryogenic trap connected to a cold head cooled with a He compressor to ≤10 K. He was desorbed at 42 K and admitted into a GVI-Helix SFT mass spectrometer. After restoring the ultra-high vacuum in the cryogenic trap, Ne was released at 82 K and then admitted into a Thermo-Helix MC Plus mass spectrometer. Ar was purified only under getters and finally admitted in a GVI-Helix MC. The analytical uncertainty of He-isotope ratio measurements (1σ) was <0.9%, while that of Ne- and Ar-isotope ratio was <0.1%. The same procedure was adopted for the He, Ne and Ar isotope measurements of the air standards (e.g., Rizzo et al., 2016), whose reproducibility conditions are comparable to those reported for FIs (see Section 4.1). Typical blanks for He, Ne, and Ar were $<10^{-15}$, $<10^{-16}$ and $<10^{-14}$ mol, respectively. Helium isotope ratios are reported in the form of R_C/R_A, where R_C is the air-corrected $^3He/^4He$ ratio of the sample, assessed based on $^4He/^{20}Ne$ ratios:

$$R_C/R_A = [(R_M/R_A)(He/Ne)_M - (He/Ne)_{air}]/[(He/Ne)_M - (He/Ne)_{air}]$$

where subscripts "M" and "air" refer to measured and atmospheric theoretical values, respectively. Argon isotope ratios account for atmospheric-corrected ^{40}Ar, assuming that all ^{36}Ar contained in the gas phase is of atmospheric origin:

$$^{40}Ar^* = {}^{40}Ar_m - [(^{40}Ar/^{36}Ar)_{air} \times {}^{36}Ar_m],$$

where $^{40}Ar^*$ represents the corrected isotope value and *m* indicates the measured value (e.g., Rizzo et al., 2018).

6.5. Elemental and isotopic compositions of He, Ne, and Ar

6.5.1. Fluid inclusions in olivine and orthopyroxene phenocrysts phases

Noble gas abundances and isotope results obtained from single-step crushing olivine and orthopyroxene phenocrysts phases from scoriae layers and lava flows from Colombia (Galeras and Nevado del Ruiz) and Ecuador (Cotopaxi, El Reventador and Tungurahua) are listed in table 1. These yield R_C/Ra values as high as 8.5 R_A (measured in olivine from Nevado del Ruiz), and as low as 2.2 R_A (obtained in FI trapped within orthopyroxene phenocrysts from Cotopaxi; Fig. 6.2). With exception of the former, all $^3He/^4He$ isotope values fall within the typical range found in arc-related FIs and free gases globally (Hilton et al., 2002; Sano and Fischer, 2013; Mason et al., 2017). Pyroxene crystalized after olivine and are invariably more degassed. He abundances ranging from 0.12 - 3.23 $\times 10^{-13}$ mol g^{-1} in orthopyroxene and 1.68 - 17.7 $\times 10^{-13}$ mol g^{-1} in olivine (Fig. 6.3a), show disequilibrium between olivine and coexisting pyroxenes from eruptive products of Ecuadorian volcanoes, which is also reflected on the lower $^3He/^4He$ ratios of orthopyroxenes than those measured in olivine (Fig. 6.3b). Olivine phenocrysts from Galeras and Nevado del Ruiz lavas yield He concentrations ranging from 0.24 - 1.19 ($\times 10^{-13}$ mol g^{-1}), respectively. As a consequence

of high Ar and Ne contents, mostly due to atmospheric-like fluids within the fluid inclusions, $^{40}Ar/^{36}Ar$ isotope ratios ranging from 297.9 to 471.7 (avg. of 328.3 across all samples) measured close to the typical atmospheric isotope signature ($^{40}Ar/^{36}Ar$ = 295.5) and yield similar values to the $^{40}Ar/^{36}Ar$ ratios here reported for fumarolic gases from Galeras central crater (297.0 and 302.1; Fig. 6.2). Our results show Ar isotope ratios lower than those originated at the upper mantle ($^{40}Ar/^{36}Ar$ ~ 40,000; Fischer et al., 2005), but fall within the range typical of subduction-related volcanism (Hilton et al., 2002; Sano and Fischer, 2013; Mason et al., 2017). Moreover, atmospheric contamination also appears reflected in the $^{4}He/^{20}Ne$ ratios here reported, that vary from 2.2 in orthopyroxenes from Cotopaxi (also the lowest $^{3}He/^{4}He$ obtained analytically) and 522.3 (Fig. 6.2), measured in Olivine phenocrysts from El Reventador (atmospheric $^{4}He/^{20}Ne$ = 0.318; mantle air-free gases are generally characterized by values ≥1000; e.g., Rizzo et al., 2018). Olivine phenocrysts also yield systematically higher $^{4}He/^{20}Ne$ ratios than their cogenetic orthopyroxene pairs (Tab. 6.1).

6.5.2. Isotope geochemistry of fumarolic gases

Sampling details and analytical data from fumarolic discharges measured at the central crater of

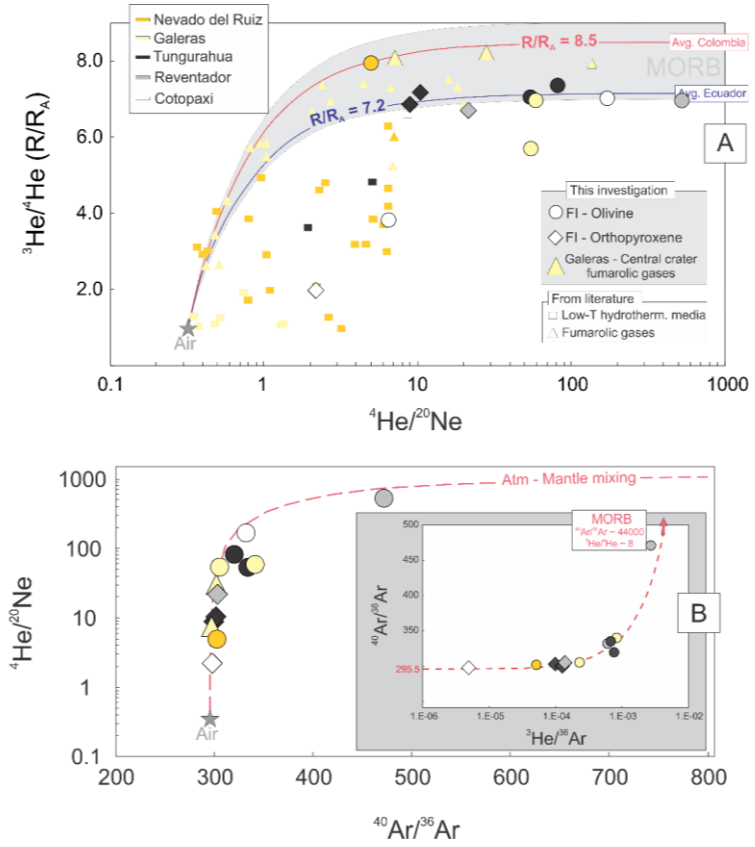

Figure 6.2: A. $^{3}He/^{4}He$ (R/R_A) vs $^{4}He/^{20}Ne$ data from FIs and free gases (low-temperature and fumarolic gases) for all 5 volcanoes. New data is represented by the larger symbols (olivine in circles; diamonds are orthopyroxene; triangles are fumarolic gases from Galeras). Smaller triangles are fumarolic data from literature (Galeras, from Sano and Williams, 1996, and Sano et al., 1997; and Nevado del Ruiz, from Williams et al., 1987), whereas small squares represent data from low-temperature springs around Tungurahua and Cotopaxi (Inguaggiato et al., 2010). Note the $^{3}He/^{4}He$ avg. for Ecuador and Colombia are given as end-members for each arc segment. Blue and red curves describe a binary mixing between air (grey star) and a magma source with He-isotope compositions of 7.0 and 8.5 R_A, respectively; and shaded area represents the MORB range (8±1 R_A). **B.** $^{4}He/^{20}Ne$ vs $^{40}Ar/^{36}Ar$ and $^{40}Ar/^{36}Ar$ vs $^{3}He/^{36}Ar$ (inset) describing the general atm-mantle mixing trends of the data reported for FIs and fumarolic gases.

Galeras are provided in table 2. The high R_C/R_A values (8.3 and 8.2 R_A, and $^{4}He/^{20}Ne$ of 7.3 and 29.6, respectively) are in agreement with values reported by Sano and Williams (1996) and Sano et al. (1997) for nearby fumarolic discharges (Fig. 6.2). Argon isotope values also showed very low variability between the two near sites, with $^{40}Ar/^{36}Ar$ of 297.9 ± 0.1 and 302.1 ± 0.2,

respectively. Figure 6.2 shows the new isotope geochemistry data from fumarolic gases and FIs integrated with existing literature data for all 5 volcanoes studied (Ecuador and Colombia).

6.6. Discussion

In order to access local and regional isotope signature variations along the Northern Volcanic Zone it is crucial to validate and interpret all isotopic results by taking into account the various processes that have the potential to mask the geochemical characteristics of the source of magmatism underlying the Northern-most segment of the Andean Volcanic Belt. Here we integrate new isotope results with previously reported Noble gas data for this volcanic arc region.

6.6.1. Atmospheric contamination

Due to their high concentration in atmosphere, light noble gases such as Ar are more susceptible to atmospheric contamination. In subduction-related volcanism Ar-isotope ratios are systematically low and close to theoretical relative abundances in the atmosphere (Hilton et al., 2002; Martelli et al., 2014; Di Piazza et al., 2015; Rizzo et al., 2015, 2016; Robidoux et al., 2017; Battaglia et al., 2018). This is even more pronounced when compared to those from intra-plate or ridge environments (e.g., Burnard et al., 1997; Moreira et al., 1998; Ballentine et al., 2005; Rizzo et al., 2018; Boudoire et al., 2018). Figure 6.2a compares our new results to those reported in the literature for high- and low-temperature free gases and shows that variable extents of air contamination affected nearly all the isotope ratios reported. Similarly, $^{40}Ar/^{36}Ar$ values are well below the theoretical mantle ratio ($^{40}Ar/^{36}Ar$ up to 44,000; Burnard et al., 1997; Moreira et al., 1998) or typical mantle-derived samples (e.g., Kaneoka, 1983; Ozima and Podosek, 1983; Allègre et al., 1987), suggesting atmospheric-like fluids to be deeply ingrained in the bulk chemistry of the inclusions studied (Fig. 6.2a). The general atmosphere-MORB trend (along the theoretical binary mixing line; Sarda et al., 1988 and Moreira et al., 1998 at $^{21}Ne/^{22}Ne = 0.06$ and $^{20}Ne/^{22}Ne = 12.5$) of figure 6.4 is also shown to clearly demonstrate the overall chemistry of FIs here studied. As many authors have suggested over the years (e.g., Gurenko et al., 2006; Rizzo et al., 2018), this may indicate mantle contamination at depth from the dehydration of atmospheric Ar from subducting oceanic crust. Due to simple mass balance, the overall atmospheric-like fluids seem to exert almost negligible effects on the helium isotope signatures, especially those measured in FIs.

6.6.2. Post-eruption ^{4}He in-growth and diffusion-controlled isotope fractionation

With the exception of the lavas from Nevado del Ruiz volcano, no samples analyzed have been dated beyond 2 ka, the oldest being perhaps the lavas flows belonging to the Post-Colorado Canyon Andesitic Activity from Cotopaxi that occurred between 1,880-1,195 yBP (Hall and Mothes, 2008). Despite the fact that lava flows here analyzed for Galeras have not been dated, well-preserved morphology allows an approximate age to be assigned, between 1100 yBP and 1866 (one of the youngest major eruptions; Calvache, 1990).

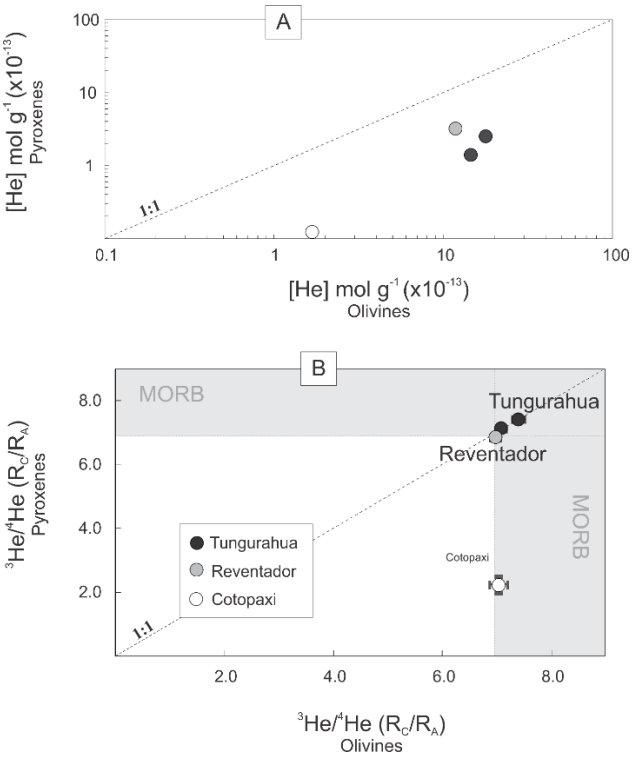

Figure 6.3: A. He characteristics of cogenetic olivine and orthopyroxene phenocrysts from Ecuador. **A.** He concentrates of pyroxenes are plotted against concentrations in cogenetic olivine; the 1:1 line is shown for reference in both. **B.** $^{3}He/^{4}He$ (R_C/R_A) ratios of orthopyroxenes are plotted against ratios of their cogenetic olivine. Note that both axes are in logarithmic scale, and that $^{3}He/^{4}He$ ratios of olivine are consistently higher than those of their cogenetic orthopyroxenes. This is especially highlighted for Cotopaxi in which the lowest R_C/R_A values was obtained (2.2 in Opx).

Therefore, a post-eruption ingrowth of radiogenic ^{4}He seems an unlikely explanation for the below-MORB $^{3}He/^{4}He$ values here reported in olivine phenocrysts from Galeras A and B (5.7 ± 0.1 and 6.9 ± 0.2, respectively) peripheral fissure vents (Fig. 6.5). On the other hand, Hilton et al. (1993) noted that a release of matrix-sited helium is possible if the sample is crushed for an extended time, and it may be inefficiently extracted by simple vacuum crushing (see Scarsi, 2000 for details).

Figure 6.4: Neon isotope systematics from fluid inclusion data for all five volcanoes. The red dashed line represents binary mixing between air and a MORB mantle as defined by Sarda et al. (1988) and Moreira et al. (1998) at $^{21}Ne/^{22}Ne$ = 0.06 and $^{20}Ne/^{22}Ne$ = 12.5, whereas the green indicates binary mixing between air and the OIB domain of the Galapagos Islands as determined by Kurz et al. (2009) at $^{21}Ne/^{22}Ne$ = 0.032 and $^{20}Ne/^{22}Ne$ = 12.5. Shaded red area the delimitates the general $^{21}Ne/^{22}Ne$ vs $^{20}Ne/^{22}Ne$ trend of our data set.obtained (2.2 in Opx).

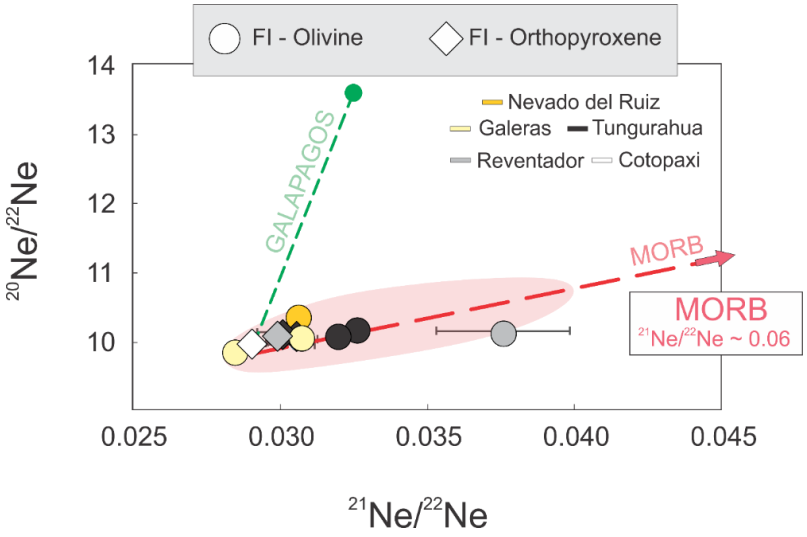

However, and despite the fact that olivine phenocrysts from Nevado del Ruiz (see section 3.1.1 for samples provenience) coincidentally yield the highest $^{3}He/^{4}He$ value and the lowest ^{4}He

concentration among olivine phenocrysts here analyzed, we suggest a negligible contribution of cosmogenic components, such as ^{3}He, to the total He content of these inclusions, with isotope ratios obtained within the range of intra-segment $^{3}He/^{4}He$ ratios here reported for fumaroles of Galeras (and also reported by Sano et al., 1997).

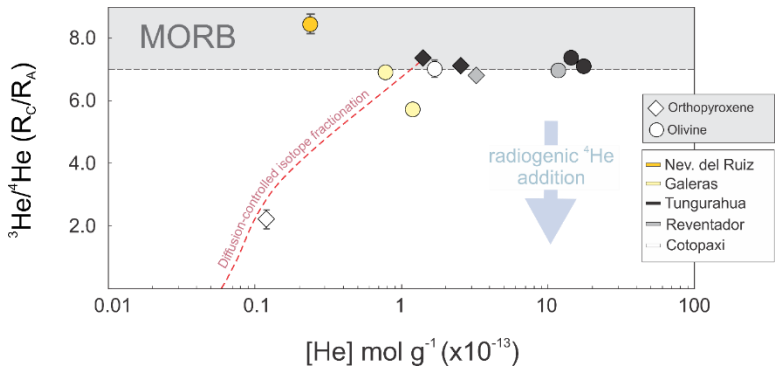

Figure 6.5: $^{3}He/^{4}He$ (R_C/R_A) ratios are plotted as a function of He concentrations in FIs (mol g^{-1}) from olivine and orthopyroxene phenocryst. The grey area shows the 8±1 MORB range, and the red dashed line represents the profile of diffusion-controlled fractionation assuming as an end-member a R_C/R_A of 7.2 (Ecuador).

At surface conditions, however, a strong pressure gradient of volatiles exists between the fluid inclusion and the external atmosphere, which can ultimately lead to diffusional losses of noble gases (Sobolev and Chaussidon, 1996), especially at high temperatures (Hauri, 2002). It is beyond the scope of this article the discussion of diffusion mechanisms of He as a function of temperature (see Hart, 1984), though is important to reiterate that such processes have the potential to modify intrinsic He characteristics in the gas bubbles, particularly because He is theoretically more prone to respond to fractionation processes than other noble gases due to the large mass difference between ^{3}He and ^{4}He and the theoretical relationship between mass and diffusion coefficients (D is inversely proportional to the square root of the atomic mass; see Rama and Hart, 1965; Craig and Lupton, 1976; Hart, 1984). The ^{3}He should therefore diffuse 15% faster than ^{4}He, which has been shown to be broadly consistent with experimentally determined ^{3}He and ^{4}He diffusivities in olivine and basalt glasses (Trull and Kurz, 1993, 1999). Therefore, it is possible that fractionation of helium isotopes may have occurred inside phenocrysts during storage within sub-solidus magmas. Moreover, the least SiO_2-rich samples found along the NVZ are usually associated with lavas that represent, in the case of Galeras and Nevado del Ruiz, rare episodes of effusive activity contrasting with the predominantly explosive, more SiO_2-rich evolution of northern volcanic complexes. Nevertheless, it is rather assumed that other erupted products, such as ash and other tephra deposits, show better preservation of volatile signatures than lavas, mostly based on the assumption that the cooling rate determines whether inclusions preserved in host minerals are glassy (Roedder, 1984; Shinohara et al., 2003). Therefore, the slower cooling experienced by lavas may allow for inclusions to crystallize, leading to subsequent volatile loss by diffusion or cracking of the inclusion host (Wallace, 2005).

Despite all the above, predominantly MORB-like $^{3}He/^{4}He$ isotope signatures suggest that diffusive fractionation plays a minor role in our newly reported results. Differences in the chemistry of FIs obtained in orthopyroxene and olivine, in part expected due to the lower effective

closure temperature and pressure of pyroxenes (that continue to exchange helium with the magma after olivine had been closed) are not observed systematically (Fig. 6.5). Furthermore, He/Ar* ratios obtained in phenocrysts and fumarolic gases show MORB-like production ranges (Marty, 2012), with no significant differences across the dataset. Here the exception appears to be the orthopyroxenes from Cotopaxi that yield He/Ar* significantly lower than our data set average (0.7; avg. 2.0) and $^{3}He/^{4}He$ of 2.2 ± 0.3 Ra (data set avg. = 7.2 R_A; Fig. 6.6). Changes in pressure and temperature during magma ascent and storage are evident in the mineral textures, and inclusions of olivine in the basaltic andesite orthopyroxene indicate that olivine was an early crystallizing phase, and pristine crystals of orthopyroxene and clinopyroxene (not analyzed for noble gas contents) in the andesites are consistent with the subsequent differentiation (Garrison et al., 2011).

For the remaining samples, however, He concentrations and respective R_C/R_A values (Fig. 6.5) show no obvious correlation. For instance, FIs in olivine phenocrysts from Nevado del Ruiz yield He concentrations two orders of magnitude lower than those here reported for olivines from Tungurahua and El Reventador, although $^{3}He/^{4}He$ estimated are 1 R_A unit higher than the previous. More importantly, it remains unclear if the lower R_C/R_A values (5.7 ± 0.1 and 6.9 ± 0.2 Ra) in olivine phenocrysts from Galeras lavas, that appear to follow the diffusion-controlled isotope fractionation profile (see Fig. 6.4), can be explained simply by helium loss from the phenocrysts after volatile trapping, or rather during residence in stationary magma at shallow depths that may have contributed with the addition of radiogenic ^{4}He by assimilation of host rocks (see Section 6.3).

6.6.3. Inferences on local and regional $^{3}He/^{4}He$ isotope signatures

The overprint of noble gas mantle signatures, especially helium, has always appeared quite significant in the northern-most part of the Andean Volcanic Belt. Previous global compilations of helium isotope data (e.g. Hilton et al., 2002; Sano and Fischer, 2013; Oppenheimer et al., 2014; Mason et al., 2017) reported $^{3}He/^{4}He$ averages of 3.2 ± 1.0 R_A and 5.7 ± 2.4 R_A for Ecuador and Colombia, respectively (e.g., Hilton et al., 2002), both far out of the known MORB-range of 8 ± 1 R_A. For instance, an extensive study by Inguaggiato et al. (2010) that reported on the geochemical signature of 56 thermal and cold waters sites, as well as 32 dissolved and 27 bubbling springs, collected north-south along the Ecuadorian arc, obtained a wide range of helium isotope results, from 0.1 and 7.1 R_A. As discussed in the previous section, this is most possibly a result of different extents of fluid-rock interaction as magmatic gas percolates through the crust before it reaches the surface. Such processes can overwhelmingly mask deep mantle noble gas isotope signatures, especially in regions characterized by older, flatter dipping slabs such as in the south of Ecuador (Barazangi and Isacks, 1979; Gutscher et al., 1999). Actively degassing volcanoes, especially those with accessible high-temperature fumarolic fields such as Galeras, Cumbal, Cerro Machin and Purace, have successfully been sampled in the past (Sano and Williams, 1987; Sano et al., 1990; Sturchio et al., 1993; Sano and Williams, 1996; Sano et al., 1997; Lewicki et al., 2000), with maximum $^{3}He/^{4}He$ isotope ratios reported of 8.8, 7.9, 6.8 and 7.1 Ra, respectively. However, for large portions of the arc, helium isotope signatures remained uncharacterized. Here we provided

the first helium isotope constrains on the mantle sources feeding the volcanic systems of Cotopaxi, Tungurahua and El Reventador, for which only peripheral data had been reported in the past Inguaggiato et al. (2010). And despite the low site-to-site variability here reported for Ecuador (when considering the new estimated values for El Reventador, Cotopaxi and Tungurahua; Tab. 3), a segment-scale uncertainty remains due to evident disparities between newly obtained helium isotope signatures for Ecuadorian volcanoes and those of Colombia (Fig. 6.7).

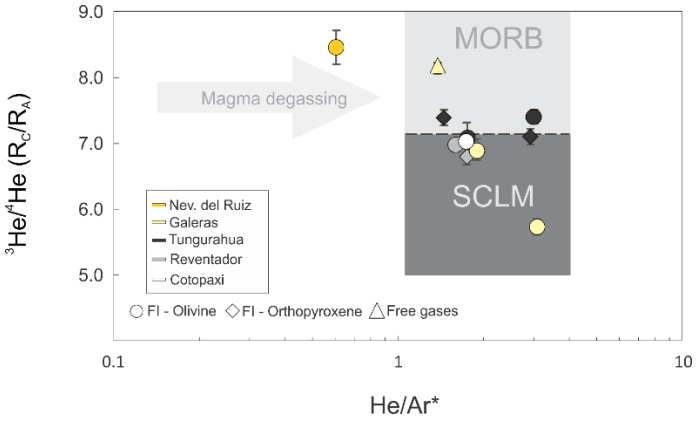

Figure 6.6: Plot of $^{4}He/^{40}Ar^{*}$ vs $^{3}He/^{4}He$ (R_C/R_A) for Ecuador and Colombia FI data; circles are olivines and diamond are orthopyroxenes; free gases are represented with triangles. The straight arrow qualitatively indicates how magma degassing would affect the $^{4}He/^{40}Ar^{*}$ ratio (Marty, 2012).

6.6.3.1. Subduction-related controls on the noble gas chemistry of NVZ fluids

At other volcanic arcs, such as the Central America Volcanic Arc (CAVA), $^{3}He/^{4}He$ variations have been attributed largely to slab/sediment input (Di Piazza et al., 2015; Robidoux et al., 2017; Battaglia et al., 2018), due to pronounced along-arc variations of Ba/La, for example within the Nicaraguan segment (Carr, 1984; Protti et al., 1995). These along-arc variations coincide with changes in the dipping of the subducting slab, whereby the steepest dip in Nicaragua induces intensive metasomatism and melting of a smaller volume of mantle (Carr et al., 1990). This results that the melt generated in the mantle is heavily imprinted with the signature of the subducted slab (e.g., high Ba/La). Furthermore, it has been suggested that anomalous OIB-like signature in the CAVA volcanic front is derived from the interaction of the mantle wedge with the Galapagos Hostpot tracks subducting beneath the arc (Benjamin et al., 2007, Hoernle et al., 2008, Wegner et al., 2010; Gazel et al., 2010;). Abratis and Wörner (2001) suggested that a "slab window" in the subducting Cocos Plate, proposed by Johnston and Thorkelson (1997) allows Galapagos-modified asthenosphere to flow into the Central American subduction system, which may culminate on the high $^{3}He/^{4}He$ ratios (as high as 8.9 R_A in Guatemala; Battaglia et al., 2019) previously reported along CAVA (see also Tassi et al., 2004; Shaw et al., 2006; Di Piazza et al., 2015).

Similarly, Bryant et al. (2006) reported Pb, Sr, and Nd isotopes and trace element evidence for the interaction between melts from the subducting Carnegie Ridge (Galapagos Plume track) and the mantle wedge in the northern Andean volcanic zone in Ecuador. However, such does not appear directly echoed in He isotopes ratios obtained for this arc segment, with $^{3}He/^{4}He$ consistently falling on the MORB lower limit (7 R_A; Ecuadorian $^{3}He/^{4}He$ sample avg. of 7.2 R_A), which may indicate a negligible contribution of hot-spot-related fluids to the noble gas isotope signatures of Ecuadorian volcanoes. Despite, for example, the apparent along-arc northward increase of C-rich

sediment input from the subducted slab (Aiuppa et al., 2017 and 2019; Lages et al., 2019; Fig. 6.7), which culminates in higher CO_2/S_T ratios for Colombian volcanoes (Fig. 6.7), other geochemical tracers, such as change in trace element content and ratios in lavas and eruptive products from individual volcanic systems in Colombia and Ecuador, which show no significant differences, seem to further indicate a trivial contribution of the subducted slab to the noble gas chemical imprint of NVZ fluids. This study therefore suggests that regardless of intra-NVZ segment variations of subduction-related parameters such as slab angle and slab descent rate (Syracuse and Abers, 2006), controls on noble gas geochemistry of Andean fluids may reside at shallower depths. Moreover, and as highlighted by Ancellin et al. (2017), consistently La/Yb >>5 along the NVZ arc segment, contrast with other island and continental arcs of thinner crust, such as southern-most part of the Andean Volcanic Belt in Chile, where La/Yb <5. This seems to suggest a rather prominent crustal role in the isotope chemistry of fluids along this segment of the volcanic trench, and despite the fact that information on crustal thicknesses in the region is limited, Bryant et al. (2006) reported that the north Andean crust that underlies the currently active volcanoes varies systematically from 25 to >50 km in Ecuador. In Colombia, gravity data indicate that the crust is 40 –50 km thick along the axis of the Andes. Nevertheless, Schaefer (1995) found a thin crust (<35 km) and/or an anomalous dense crust around the Nevado del Ruiz (Fig. 6.8), which we suggest correlate with variations in $^3He/^4He$ values along the arc, and ultimately believe to control the extent of isotope variability measured in deep uncontaminated, homogenously degassed, magmatic fluids.

6.6.4. Crustal assimilation of radiogenic ^4He

As previously discussed, $^3He/^4He$ values recorded in orthopyroxenes from Cotopaxi (<< 8 R_A) seem to be univocal of processes of isotope fractionation and extensive helium loss. However, apart from this sample, all $^3He/^4He$ ratios in phenocrysts and fumarolic gases reported (Tab. 6.1 and 2) are significantly higher than orthopyroxenes from Cotopaxi, with most samples lying approximately within MORB range (8 ± 1 R_A). As discussed in the previous sections, the notable exceptions here are the olivine phenocrysts from Galeras A and B, both yielding slightly lower-than MORB R_A values. This is even more emphasized by the discrepancy between the R_A values reported in olivine inclusions and those of fumarolic gases sampled at central crater in July 2017 (8.3 ± 0.1 and 8.2 ± 0.1 R_A; see Tab. 6.2 and Fig. 6.7) and reported by Sano et al. (1997) between 1988-1993 (as high as 8.8 ± 0.6 R_A). Another important observation from our newly reported dataset is that averaged $^3He/^4He$ isotope values for Ecuador and Colombia, when considering the highest measured $^3He/^4He$ (R_C/R_A) ratio differ by 1.5 R_A units (Ecuador ~7.2 R_A; Colombia ~8.5 R_A).

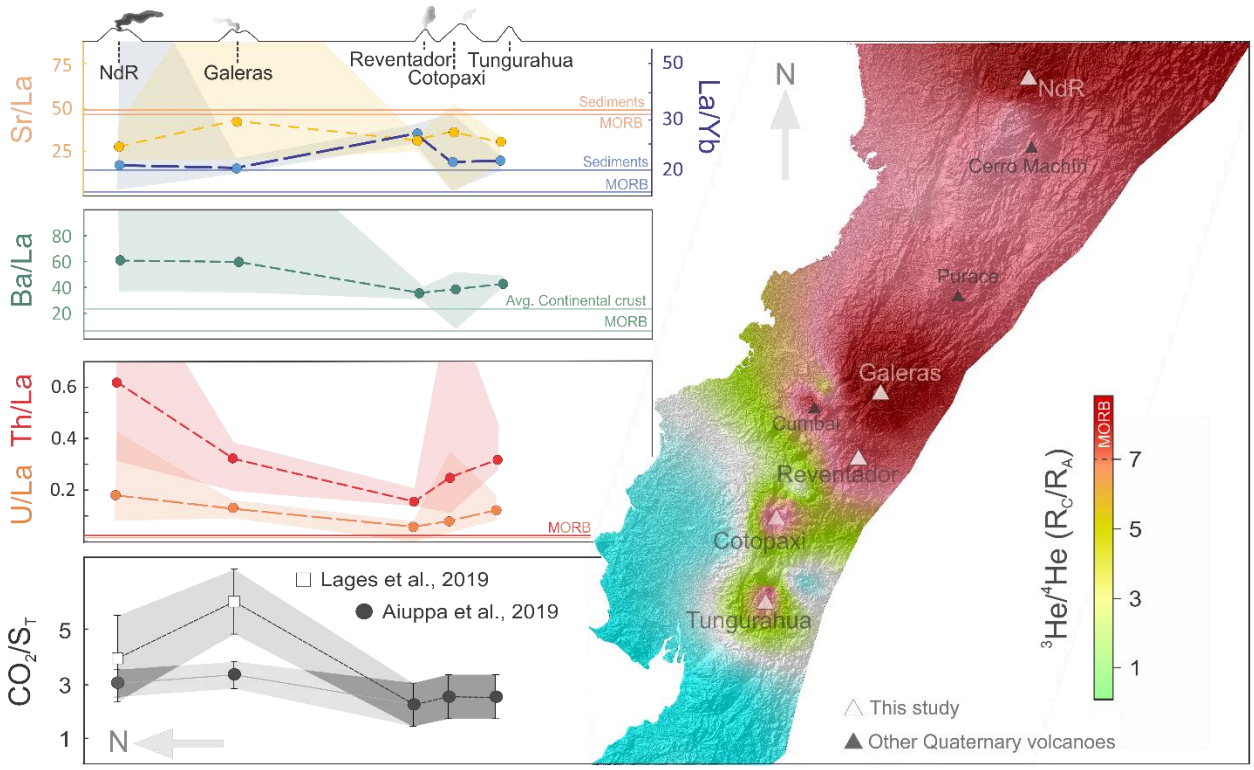

Figure 6.7: On the left: along-arc whole-rock trace element compositions of lavas from Nevado del Ruiz (Perignon et al., 1988), Galeras (Calvache and Williams, 1997a and b), Reventador (Samaniego et al., 2008), Cotopaxi (Garrison et al., 2011) and Tungurahua (Samaniego et al., 2011); shaded areas represent compositional variations between the lowest and highest value reported in literature for a given trace element ratio; at the bottom CO_2/S_T data is from Aiuppa et al., 2019 (in dark) and Lages et al., 2019 (in white); shaded areas represent the uncertainty associated with each volcanic gas measurement; note that CO_2/S_T values for Ecuador (Aiuppa et al., 2019) are predicted using regional/global relationships between the CO_2/S_T ratio of volcanic gases and whole-rock trace element compositions (e.g., Ba/La). On the right: geostatistical interpolation (kriging, Surfer 13 software) of along-arc $^3He/^4He$ reported in table 3; note that only maximum values were considered for each individual coordinate point.

Ecuadorian magmas using different tools (trace elements and Sr-Nd-O isotopes). Most of those studies agree that upper crustal assimilation plays a key role in magma evolution. In fact, partial or bulk assimilation of crustal lithologies by basaltic-andesite magmas is an intuitively reasonable and thermodynamically possible explanation for this phenomenon (e.g., Kerr et al., 1995), especially for magmas extruding in arc regions characterized by exceptionally thick continental crust, such as the overall Ecuadorian arc (>50km) and southern-most regions of Colombia (45-50 km; Feininger and Seguin, 1983; Prévot et al., 1996; Guillier et al., 2001). This relationship between crustal thickness and magma composition (Leeman, 1983; Plank and Langmuir, 1988) results in more evolved eruptive products, as seen throughout the Northern Volcanic Zone. Some of these rocks were investigated by James and Murcia (1984) for Galeras and Nevado del Ruiz (Colombia), that found isotopic evidence of significant ^{18}O-rich crustal component in the petrogenesis of these eruptive products, mostly related to processes happening during magmatic ascent.

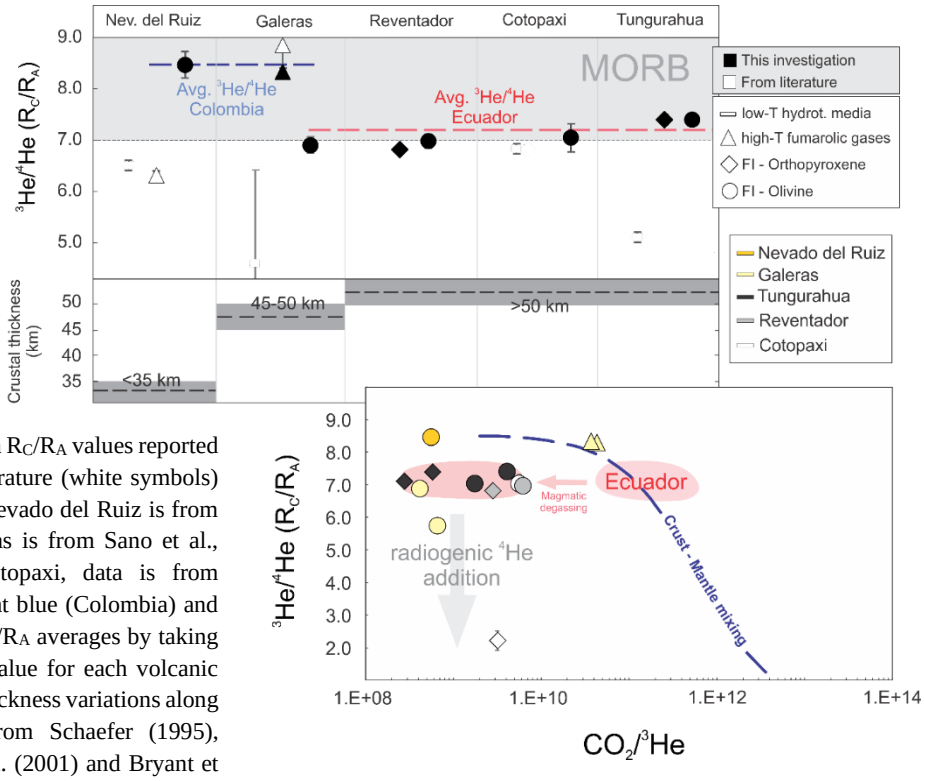

Figure 6.8: At the top: Maximum R_C/R_A values reported in this study (in dark) and in literature (white symbols) for all five volcanoes. Data for Nevado del Ruiz is from Williams et al., 1987; for Galeras is from Sano et al., 1997; for Tungurahua and Cotopaxi, data is from Inguaggiato et al., 2010; Note that blue (Colombia) and red (Ecuador) dashed indicate R_C/R_A averages by taking into account the single highest value for each volcanic system. **At the bottom:** crustal thickness variations along the Northern Volcanic Zone from Schaefer (1995), Prévot et al. (1996), Guillier et al. (2001) and Bryant et al. (2006). Inset: $CO_2/^3He$ systematics of NVZ fluids; Crust-mantle binary mixing line (in blue) assumes an R_A of 8.5 (avg. Colombia).

The extent of fluid contamination by radiogenic crustal components varies substantially depending on a wide range of geochemical and geophysical parameters. For instance, fluids trapped in olivine from Ecuadorian volcanoes yielding lower limit-MORB range $^3He/^4He$ isotope signatures (avg. 7.2 R_A) may be the outcome of crustal assimilation of deep magmatic fluids slowly ascending to shallower sub-reservoir levels, especially along the main volcanic arc where maximal (up to 27%; see Ancellin et al, 2017) lower crust assimilation has been reported. Hildreth and Moorbath (1988) and Annen et al. (2006) advocate processes of accumulation, recycling, fractionation, and assimilation of crustal material in the so-called deep crustal hot zones (Weber et al., 2002) as the dominant agents of magma petrogenesis in this arc region. As for the Eastern Cordillera volcanic centers, such as El Reventador, that are characterized by unradiogenic $^{206}Pb/^{204}Pb$ and $^{207}Pb/^{204}Pb$ compositions (Ancellin et al., 2017), more upper crust contributions are proposed. Therefore, and despite the significant differences between lower and upper crust reservoirs in terms of their U and Th contents (0.2 and 1.2 ppm of U and Th at the lower crust, to 2.7 and 10.5 ppm at shallower crustal levels; Rudnick and Fountain, 1995; Rudnick and Gao, 2003, 2014; see also Hacker et al., 2011), we argue that shallower, crustal processes, either related to stationary magma bodies (magma aging) and/or interaction of fluids with crustal rocks, play a crucial role in the isotope composition of lower $^3He/^4He$ (yet in the MORB range), evidenced in Ecuadorian samples, in comparison to those obtained in olivine phenocrysts from Nevado del Ruiz and measured in fumarolic gases at Galeras.

Nonetheless, if contamination of pristine noble gas compositions happens, to an overwhelming extent, at crustal depths, we may therefore hypothesize a rather homogeneous mantle source for NVZ volcanism. Previous studies have relied heavily on $^{13}C/^{12}C$ and $CO_2/^3He$ to constrain mixing of marine limestones and organic sediments with upper mantle fluids (e.g., Marty and Jambon, 1987; Sano and Marty, 1995; and references therein). The CO_2-poor nature of FIs analyzed in this study, however, did not allow for estimation of $\delta^{13}C$ of individual samples, which constitutes a limiting factor to better constrain the contribution of each volatile source (mantle, slab and crust) to NVZ fluids trapped in olivine and orthopyroxene phenocrysts. Still, lower $CO_2/^3He$ of Ecuadorian samples may be explained by early exsolution of CO_2 from the magma and subsequent entrapment of CO_2-impoverished fluids by crystals forming at shallower depths with variable extents of crustal contamination. Therefore, the dissimilarity of $^3He/^4He$ ratios between Colombia and Ecuador (Fig. 6.8), may be more revealing of magmatic degassing processes (volatile loss during crystallization and shallow fluid entrapment) than of a heterogeneous mantle source beneath the NVZ.

6.7. Concluding remarks

Processes of magmatic fluids ascent and consequent interactions with continental crust makes volcanic arc trenches a challenging geodynamic setting when it comes to characterize the pristine noble gas composition of upper mantle fluids feeding volatiles, including noble gases, to shallower magmatic reservoirs. At regions of remarkably thick crust, like the Andes, such task becomes exponentially more difficult, with very rare petrogenetic examples of uncontaminated mantle products rising to the Earth's surface.

New noble gas data here reported for FIs hosted in olivine and orthopyroxene phenocrysts from 5 of the most persistently active volcanoes in the Northern Volcanic Zone, and updated fumarolic gas data for Galeras has allowed for the characterization the mantle fluids signature source along Northern-most segment of the Andean Volcanic Belt, with a few important remarks:

1. New He isotope data reported for the Ecuadorian arc, and first helium isotope characterization of eruptive products from Reventador, Cotopaxi and Tungurahua (for which only peripheral, low-temperature data had been reported) revealed significantly higher helium isotope signatures (Avg. R_C/R_A ~7.2) to those previously reported in literature (max. 6.8 and 5.1 R_A for Cotopaxi and Tungurahua, respectively; Inguaggiato et al., 2010).

2. The highest $^3He/^4He$ ratio measured in rocks and gases for each individual volcanic system (7.0–8.5 R_A) are consistent with the typical MORB-range expected at arc volcanism (8±1 R_A). Excluding Galeras, for which previous studies had reported R_C/R_A values up to ~8.8 R_A, all values obtained in this study represent the highest R_C/R_A values ever reported for these volcanic systems.

3. A significant discrepancy arises when averaging the highest $^3He/^4He$ from individual volcanic centers from the two arc segments, with an estimated average of ~7.2 R_A for Ecuador and ~8.5 R_A for Colombia. Although the reported constrains fall within the expected MORB range, we argue that a systematic difference exists between both NVZ regions.

4. Whole rock chemistry (e.g., Ba/La, La/Yb) from lavas and other eruptive products show no significant along-arc variations with northward increase in C-rich sediment input (higher CO_2/S_T volcanic gas signatures) and, therefore, we suggest that the input of sediments from the subducted slab play a minor contamination role on deep mantle fluids.

5. Instead, significant regional variations in crustal thickness, and positive correlation between the overlying thickness of continental crust and helium isotope variation suggest that processes masking the pristine composition of deep mantle fluids may occur within the crust, with addition of radiogenic ^{4}He whether as gas percolates through the host rock, or by assimilation of U-Th-rich crustal lithologies as magma reservoirs interact with the host rock.

In summary, this study brings significant contribution to arc-related knowledge of noble gas circulation and crustal assimilation processes happening at trenches of exceptionally thick continental crust. Here, we demonstrate the importance of not limiting ^{3}He/^{4}He mantle constrains to surface gases. However, and in order to better constrain extensive arc segments and understand the role of slab geometry along the Northern Volcanic Zone, future studies must focus on establishing a much more systematic approach to sampling of noble gases at arc volcanoes.

6.8. Acknowledgements

We would like to thank all the staff members from the *Instituto Geofísico — Escuela Politécnica Nacional,* (Quito, Ecuador) for their incredible logistical and technical support throughout our field campaign in Ecuador (Feb. 2017). In particular, we would like to thank Benjamin Bernard for his assistance and scientific advice, and for providing the rock samples from Reventador analyzed in this study. We would also like to thank the *Servicio Geológico Colombiano***,** the volcanological observatories of Pasto and Manizales and their staff for their crucial assistance on fieldwork in Galeras and Nevado del Ruiz. INGV-Palermo provided analytical facilities. We are also grateful to Mariano Tantillo and Mariagrazia Misseri for their support in sample preparation and noble gases analysis of FIs. The fieldwork portion of this work was funded by the DECADE initiative, from Deep Carbon Observatory - Alfred P. Sloan Foundation.

Chapter 6 – Table(s)

Table 6.1: Noble gas abundances and isotope ratios of mafic phenocrysts from Colombia and Ecuador (Northern Volcanic Zone – Andean Volcanic Belt)

Table 6.2: Noble gas compositions of fumarolic gases sampled at the central crater of Galeras, Colombia.

Table 6.3: Helium isotope data compilation for Northern Volcanic Zone Quaternary volcanoes and hydrothermal areas.

Table 1

Noble gas abundances and isotope ratios from mafic phenocrysts from Colombia and Ecuador (Northern Volcanic Zone – Andean Volcanic Belt)

Volcano	Sample ID	Sample details	Rock	Min. phase	Weight (g)	[He] $x10^{-13}$	[Ne] $x10^{-14}$	[^{40}Ar] $x10^{-12}$	[^{36}Ar] $x10^{-15}$	[^{40}Ar*] $x10^{-13}$	CO_2 $x10^{-9}$	$^{4}He/^{20}Ne$	$^{20}Ne/^{22}Ne$	$^{21}Ne/^{22}Ne$	He/Ar^{*}	$^{40}Ar/^{36}Ar$	$^{3}He/^{4}He$ (R/R_A)	$^{3}He/^{4}He$ (R_C/R_A)	$CO_2/^{3}He$ $x10^{9}$
	Colombia																		
Nev. del Ruiz	JCH-04	Fissure lavas	BA	Oliv	0.99	0.24	0.48	1.65	5.46	0.40	0.16	5.0	10.12 ± 0.03	0.0297 ± 0.0005	0.60	302.8 ± 0.1	7.96	8.46 ± 0.26	0.56
Galeras	GA1	Fissure lavas	BA	Oliv	1.07	1.19	0.22	1.25	4.09	0.39	0.62	54.6	9.83 ± 0.04	0.0284 ± 0.0007	3.08	304.9 ± 0.1	5.70	5.73 ± 0.12	0.66
	GA2	Fissure lavas	BA	Oliv	0.79	0.78	0.13	0.30	0.89	0.41	0.31	59.0	9.95 ± 0.08	0.0298 ± 0.0013	1.89	341.9 ± 0.3	6.87	6.90 ± 0.16	0.42
	Ecuador																		
Cotopaxi	COT.LF.1B	Lava flow	A	Oliv	0.19	1.68	0.10	0.87	2.62	0.96	9.26	171.3	10.46 ± 0.18	-	1.75	332.2 ± 0.5	7.03	7.04 ± 0.28	5.64
				Opx	1.12	0.12	0.53	2.19	7.35	0.18	1.14	2.2	9.90 ± 0.02	0.0287 ± 0.0004	0.66	297.9 ± 0.1	2.00	2.22 ± 0.30	3.19
Reventador	REV.BB007 #16	Lava flow	A	Oliv	0.33	11.70	0.22	1.97	4.17	7.34	69.4	522.3	10.15 ± 0.08	0.0376 ± 0.0001	1.59	471.7 ± 0.1	6.97	6.98 ± 0.08	6.13
				Opx	0.44	3.23	1.50	6.67	21.90	1.84	8.63	21.5	9.97 ± 0.03	0.0306 ± 0.0001	1.75	303.9 ± 0.04	6.71	6.80 ± 0.13	2.83
Tungurahua	Tung 1100	Tephra deposits	A	Oliv	0.23	17.70	3.30	8.75	26.20	10.00	31.1	53.8	9.97 ± 0.02	0.0297 ± 0.0002	1.77	333.8 ± 0.2	7.05	7.08 ± 0.09	1.78
				Opx	0.89	2.55	2.88	5.88	19.60	0.87	0.70	8.9	9.98 ± 0.01	0.0294 ± 0.0002	2.92	300.0 ± 0.1	6.87	7.10 ± 0.12	0.28
	Tung 2006	Block PDC	A	Oliv	0.24	14.40	1.77	6.23	19.50	4.79	60.8	81.1	10.02 ± 0.02	0.0310 ± 0.0003	3.00	320.0 ± 0.2	7.37	7.40 ± 0.10	4.11
				Opx	0.87	1.40	1.35	4.33	14.30	0.97	0.84	10.4	9.97 ± 0.02	0.0293 ± 0.0002	1.45	302.3 ± 0.1	7.19	7.39 ± 0.11	0.58

Host rock chemical classification on the basis of SiO_2 contents: A (andesite), BA (basaltic-andesite)

Noble gas and CO_2 concentrations in mol g^{-1}

Mineral phases analyzed: Oliv (olivine), Opx (orthopyroxene)

Table 2

Noble gas compositions of fumarolic gases sampled at the central crater of Galeras, Colombia

Galeras	date	Lat, Long (N, W)	Temp. (°C)	[He] ppm	CO_2 %	$^{40}Ar^*$ ppm	$^4He/^{20}Ne$	He/Ar^*	$^{40}Ar/^{36}Ar$	$^3He/^4He$ [a] (R/R_A)	$^3He/^4He$ [b] (R_C/R_A)	$CO_2/^3He$ $x10^{10}$
Central crater	14 Jul 2017	1.221, -75.360	91.3	2.18	93.41	-	7.29	-	-	8.01	8.33 ± 0.07	3.71
Central crater	14 Jul 2017	1.221, -75.359	87.5	1.93	96.15	1.40	29.63	1.38	302.1 ± 0.2	8.11	8.19 ± 0.07	4.38

[a] $R/R_A = {}^3He/^4He_{(meas.)}/{}^3He/^4He_{(air)}$ [$^3He/^4He_{(air)}=1.4\times10^{-6}$]

[b] R_C/R_A is the air corrected He isotopic ratio based on the $^4He/^{20}Ne$ ratio (Giggenbach et al., 1993).

Note: only $^{40}Ar/^{36}Ar > 300$ are reported in order to avoid overestimation of $^{40}Ar^*$

Table 3

Helium isotope data compilation for Northern Volcanic Zone Quaternary volcanoes and hydrothermal areas.

		Low-T hydrothermal sources $^3He/^4He$ (R_C/R_A)				High-T fumarolic gases $^3He/^4He$ (R_C/R_A)				Fluid Inclusions (Oliv, Opx) $^3He/^4He$ (R_C/R_A)			
Colombia	Latitude	*Max*	Avg.	Nr. samples	Ref.	*Max*	Avg.	Nr. samples	Ref.	*Max*	Avg.	Nr. samples	Ref.
Nevado del Ruiz	4.89	6.4	3.9±1.4	22	1,2	6.3	---	1	1	8.5	---	1	*
Cerro Machín	4.48	5.9	5.2±0.9	2	3	6.75	---	1	4	---	---	n/d	---
Purace	2.31	6.7	4.9±1.3	8	5	7.1	6.4±0.5	4	5,6	---	---	n/d	---
Galeras	1.22	4.6	2.0±1.3	7	7	8.8	7.7±0.9	20	4, 7, *	6.9	6.3±0.8	2	*
Cumbal	0.94	5.5	---	1	8	7.9	6.3±0.9	10	4, 8	---	---	n/d	---
Ecuador													
Reventador	-0.08	---	---	n/d	---	---	---	n/d	---	7.0	6.9±0.1	2	*
Guagua Pichincha	-0.17	3.4	---	1	9	4.1	4.1±0.2	2	p.c.	---	---	---	---
Cotopaxi	-0.70	6.8	---	1	9	---	---	---	---	7.0	4.6±3.4	2	*
Tungurahua	-1.45	2.7	4.6±0.7	2	9	---	---	---	---	7.4	7.2±0.2	4	*
Chimborazo	-1.47	2.1	---	1	9	---	---	---	---	---	---	---	---
Other sites													
Cuicocha	0.29	6.3	---	1	9								
Pululahua	0.01	3.7	---	1	9								
El Pisque Balneario	0.00	4.2	---	1	9								
Balneario Oyacachi	-0.22	2.6	---	1	9								
Jamanco	-0.38	7.1	---	1	9								
Cachiyacu Cueva	-0.41	6.5	---	1	9								
Cachiyacu	-0.41	4.2	---	1	9								
Aguas calientes	-0.44	3.4	---	1	9								
Quilotoa	-0.86	2.1	---	1	9								
S. Vicente	-2.23	0.1	---	1	9								
Jesus Maria	-2.63	0.3	---	1	9								

Max: maximum R_C/R_A value for a given sampling media

Avg: *average of all samples for a given sampling media ± 1 σ*

Ref. 1. Williams et al., 1987; **2.** Sano et al., 1990; **3.** Inguaggiato et al., 2016; **4.** Sano and Williams, 1996; **5.** Sturchio et al., 1993; **6.** Maldonado et al., 2017; **7.** Sano et al., 1997; **8.** Lewicki et al., 2000; **9.** Inguaggiato et al., 2010. *****This investigation; **p.c.** personal communication (unpublished)

CHAPTER 7

Major volatiles and noble gas recycling along the Andean Volcanic Belt (AVB): insights into subduction dynamics, mantle and crustal processes from relative CO_2/S_T abundances and $^3He/^4He$ isotope signatures

Abstract. In this chapter we report on Noble gas chemistry of fluid inclusions in clinopyroxene and olivine phenocrysts from two distinct arc segments of the Andean Volcanic Belt: the Central Volcanic Zone (Peru; Sabancaya, El Misti and Ubinas) and the Southern Volcanic Zone (Villarica). Olivine phenocrysts from Villarica yield R_C/R_A values as high as 6.7 ± 0.1 R_A and as low as 4.0 ± 0.2 R_A. On the other hand, fluid inclusions trapped within clinopyroxenes handpicked from juvenile blocks and andesitic lava flows from Peru gave R_C/R_A values comprised between 2.1 ± 0.2 (Sabancaya) and 6.4 ± 0.2 (El Misti), with maximum values for all 3 volcanoes showing $^3He/^4He$ ratios of 6.0, 6.0 and 6.4 R_A (for Ubinas, Sabancaya and El Misti, respectively). In comparison to previously discussed noble gas data from Northern segments (Colombia and Ecuador), this chapter suggests a clear distinction between $^3He/^4He$ "end-members" along the arc. In Colombia, where crustal thickness reaches values <35 km, values as high as 8.8 R_A have been reported; in Ecuador a decrease in of the $^3He/^4He$ "end-member" of about ~7.2 R_A follows an increase in crustal thickness to values greater than 50 km. In Peru, where continental crust is the thickest (>70km) $^3He/^4He$ values obtained for Sabancaya, El Misti and Ubinas, all yield results lower than 6.5 R_A. Therefore, we suggest that the most viable explanation for the lower $^3He/^4He$ ratios southward may be a result of prolonged diffusive exchange with radiogenic He from the surrounding crust (and associated fluids) occurring as ascends to arc regions of exceptionally thick continental crust.

7.1. Introduction

The morphology of the Andes, as well as the tectonic controls governing active volcanism along the arc are extensively described in the literature (e.g., Stern, 2004), with emphasis on the geochemistry of fluids and subduction dynamics of the Northern Volcanic Zone that have been specifically scrutinized in the previous chapter of this dissertation.

In this chapter we report results obtained following a similar sampling and analytical approach in order to try and expand the constrains on the magmatic signature of Andean fluids, in particular for volcanic centers located in the Central Volcanic Zone (Peru) and in the southern-most part of the SVZ arc segment (Chile). With respect to noble gas studies, Peru still represents an arc region for which limited amounts of data is available. Volcanic gas emissions have been studied by Moussallam et al. (2017a, 2017b) in this region and volcanic gas compositions, fluxes and their interpretation on the overall subduction context of the Andes are discussed in detail in chapter 4. On the other hand, as mentioned previously, noble gas information is close to inexistent in this

portion of the trench. Hilton et al. (2002) reported a single $^{3}He/^{4}He$ of 2.8 R_A which prompted the urgency for more data along this segment of the arc.

This chapter compares data presented in the previous chapter (Ecuador and Colombia, Northern Volcanic Zone) to new noble gas isotope results obtained for Sabancaya, Ubinas and El Misti (Peru, CVZ) and Villarrica (Chile, SVZ), and attempts to correlate the geochemical patterns put in evidence through newly reported noble gas and volcanic gas composition data acquired throughout this PhD investigation.

7.2. Central Volcanic Zone (CVZ)

Volcanoes in the Central Volcanic Zone occur majorly at the Cordillera Occidental. Below the CVZ the <60 Ma Nazca plate lithosphere is being subducted at 7-9 cm/yr, in a direction that varies from 20 to 24° southeast of orthogonal with the trench below the northern CVZ in southern Perú, to 27° northeast of orthogonal with the trench in the southern CVZ of northern Chile. The subducting slab descends at a dip of 25° to a depth of > 400 km (Dorbath et al., 1996). The volcanic front is located in the western Cordillera Occidental, 120 km above the subducted slab and 240-300 km east of the trench, which reaches a maximum depth of 8,055 m below sea level at 23°S. Crustal thickness below the CVZ reach >70 km, and basement ages range from as old as ~2000 Ma below the northern part of the segment in Perú and northernmost Chile and Bolivia, to late Precambrian and Paleozoic below the southern part of this segment in northern Chile and Argentina. The northern end of the CVZ coincides with the locus of subduction of the Nazca Ridge and the Abancay Deflection, while the southern boundary coincides with a seismic discontinuity at 27°S (González-Ferrán et al., 1985) superimposed on a gradual decrease in subduction angle to the south (Cahill and Isacks, 1992).

7.2.1. Sabancaya

The Ampato–Sabancaya volcanic complex comprises two successive edifices. During the Holocene, eruptive activity migrated to the NE and built up the Sabancaya edifice, between 6 and 3 ka. This cone comprises andesitic and dacitic blocky lava flows which were emplaced during at least two eruptive stages (Samaniego et al., 2016). The Ampato–Sabancaya samples display a high-K magmatic trend, ranging from andesites to dacites (57 to 69 wt.% SiO_2), with rare rhyolitic compositions (74–77 wt.% SiO2). Some of the mineralogically suitable samples collected for analysis include lavas from the upper Ampato, that present porphyritic texture, composed by phenocrystals (30 - 60 vol.%) Of plagioclase, biotite, amphibole, clinopyroxene, Fe-Ti oxides and eventually by orthopyroxene and olivine (<2%; Samaniego et al., 2016).

7.2.2. Ubinas

The Ubinas volcano is located ~75 km east of Arequipa in the Western Cordillera of the Central Andean Volcanic Zone. The volcano is built upon a 65 km-thick, mature continental crust that consists of Mesozoic and Cenozoic sedimentary and volcanic formations unconformably overlying a Precambrian basement (Kink et al., 1986; Mégard, 1987). Over the past 500 years, Ubinas

produced mostly tephra with a trend towards more mafic magma compositions in recent times (Thouret et al., 2005; Rivera, 2010). The 2006 and 2014 juvenile blocks here analyzed are dark to gray, dense to poorly vesicular, porphyritic andesites bearing 20–25 vol.% of phenocrysts (300 μm– 1.8 mm), 30–40 vol.% of microphenocrysts (100–300 μm), and 35–50 vol.% of matrix glass. Glomerophenocrysts of plagioclase, clinopyroxene, orthopyroxene, and Fe–Ti oxide are abundant. Both samples show a similar mineral assemblage including plagioclase, clinopyroxene, orthopyroxene and magnetite with scarce amphibole and olivine (Rivera et al., 2013). Olivine phenocrysts occur in the 2006 ballistic blocks, although not sufficient for analysis of Noble gases in fluid inclusions trapped within those phenocrysts.

7.2.3. El Misti

El Misti is a major andesitic volcano located near the city of Arequipa in the northern Central Volcanic Zone. It straddles the western flank of the Western Cordillera, approximately 240 km east of the Peru-Chile trench and ~90 km above the top of the subducting Nazca plate. Plagioclase is by far the most abundant mineral phase followed in abundance by amphibole and pyroxene, while olivine is extremely rare and only occurs in some andesites. Olivine occurs only in mafic andesites and when present is scarce, never exceeding 2 vol.%. Rivera et al. (2017) report subhedral to anhedral olivine crystals with sizes smaller than 400 μm. Misti 2 olivine has a Forsterite composition of Fo76–80 while Misti 3 olivine has a slightly lower magnesium content (Fo70–78) (SEM 1). Subtle normal zoning is present in olivine from both Misti 2 and 3. When compared with olivine from primitive arc magmas (Fo80, Tamura et al., 2000; Ruscitto et al., 2011; Sorbadère et al., 2013) the relatively low-Fo content of the El Misti olivine (Fo70–80) provides evidence against a pure, primary, mantled-derived origin for El Misti rocks (Rivera et al. 2017).

7.3. Southern Volcanic Zone (SVZ)

The northern end of the SVZ coincides with the locus of subduction of the Juan Fernández Ridge and the southern end with the Chile Rise. All along the SVZ, the 0-45 Ma Nazca plate is being subducted below the continent at 7-9 cm/yr in a direction 22-30° northeast of orthogonal with the trench. Subduction angle increases from ~20° at the northern end of the SVZ to >25° further to the south. As a consequence, the distance from the trench to the volcanic front decreases from >290 km in the north to <270 km in the south, and the depth to the subducted slab below the front decreases from 120 to 90 km. Crustal thickness also decreases southwards from >50 km below the northern end of the SVZ to approximately 30-35 km below the southern end. Pre-Andean basement ages range from Paleozoic to early Mesozoic (Munizaga et al., 1988; Nelson et al., 1999).

7.3.1. Villarrica

Villarrica lies at the NW end of the NW – SE-trending, trans-Andean volcanic chain which has been interpreted as a line of crustal weakness (Moreno et al., 1994b). The Villarrica volcanic edifice is constructed of pyroclastic flow and scoria fall deposits as well pahoehoe lavas. The symmetrical, actual cone is located on the NW rim of a glaciated caldera (Moreno, 1994). Activity

at Villarrica has been characterized in the past by frequent small eruptions as well as highly explosive, caldera-forming pyroclastic eruptions of basaltic andesite magma (Clavero and Moreno, 1994). The stratovolcano is notable in that it has maintained an active lava lake in its summit crater from the end of the last eruption in 1985 until the present (Witter et al., 2004). During this time, Villarrica has continuously degassed from the lava lake with continuous magmatic material being expelled from the central crater predominantly through strombolian activity. In March 2015, a 3 month-long phase of escalating volcanic activity culminated into the largest paroxysm since 1985 (Aiuppa et al., 2017).

Samples collected for analysis include scoria from a few months after the 2015 eruption, with Fo content ranging from about 70 to 82 (avg. 77). The Cl contents of melt inclusions are consistently low, while the S contents are more variable but consistently low at low Fo content. Previously analyzed samples showed petrological similarities to those analyzed here. Samples from lava lake contain analyzed by (Witter et al., 2004) contained 33 wt.% plagioclase (An58 – 74), 7 wt.% olivine (Fo75 – 78), and trace amounts of chromian spinel. Glass inclusions in olivine and plagioclase are basaltic andesite in composition, are mostly degassed.

7.4. Noble gas geochemistry of fluid inclusions

Noble gas abundances and isotope results obtained from single-step crushing olivine and pyroxene phenocrysts phases from eruptive products from Peru (Sabancaya, Ubinas and El Misti) and Chile (Villarica) are summarized in table 7.1. Here we extend our noble gas results to southern segments of the Andean Volcanic Belt and aim to compare local and regional isotope signatures here reported for the different parts of the volcanic trench.

Sample preparation and noble gas extraction from fluid inclusions was carried out following the same procedure described in detail in chapter 6 of this dissertation (see previous chapter for analytical and technical details on sample preparation and analyzes). For the 5 samples analyzed for Villarica, R_C/R_A values as high as 6.7 ± 0.1 R_A (measured in olivines from Villarrica), and as low as 4.0 ± 0.2 R_A (measured in olivines from ~2.6 ka lapilli bombs) were obtained. The $^{40}Ar/^{36}Ar$ ratios measured between 334 ± 0.3 and 302 ± 0.1 showed values close to the atmospheric $^{40}Ar/^{36}Ar$ signature (~295.5).

For Peruvian samples, maximum R_C/R_A values for each individual volcanic system showed a consistent range, despite their $^{3}He/^{4}He$ ratios << 8 (MORB range, ± 1). Due to the more evolved nature of magmas found along this segment of the arc, olivine is scarce and recurrently found in insufficient amounts for analyzes. Therefore, fluid inclusions trapped within clinopyroxenes handpicked from juvenile blocks and andesitic lava flows were analyzed and yield R_C/R_A values comprised between 2.1 ± 0.2 (Sabancaya) and 6.4 ± 0.2 (El Misti). However, as mentioned above, maximum values for all 3 volcanoes showed $^{3}He/^{4}He$ ratios of 6.0, 6.0 and 6.4 for Ubinas, Sabancaya and El Misti, respectively.

7.4.1 Atmospheric contamination

Helium isotope ratios are reported in the form of R_C/R_A, where R_C is the air-corrected $^3He/^4He$ ratio of the sample, assessed based on $^4He/^{20}Ne$ ratios:

$$R_C/R_A = [(R_M/R_A)(He/Ne)_M - (He/Ne)_{air}]/[(He/Ne)_M - (He/Ne)_{air}]$$

where subscripts "M" and "air" refer to measured and atmospheric theoretical values, respectively, as described in the previous chapter 6.

The effect of air contamination on the $^3He/^4He$ ratio can be observed in the plot of R/R_A vs $^4He/^{20}Ne$ shown in figure 7.1, where FI data are compared to those obtained in FIs from Ecuador and Colombia (chapter 6). He-isotope data of FIs for Villarica and Peru (Sabancaya, El Misti, Ubinas) show significantly deviation from the range limited by the binary mixing lines between air and a magmatic end-member having an R_A of 7 and 9 (MORB range; Fig. 7.1). This suggests that a variable extent of air contamination affected nearly all the samples analyzed.

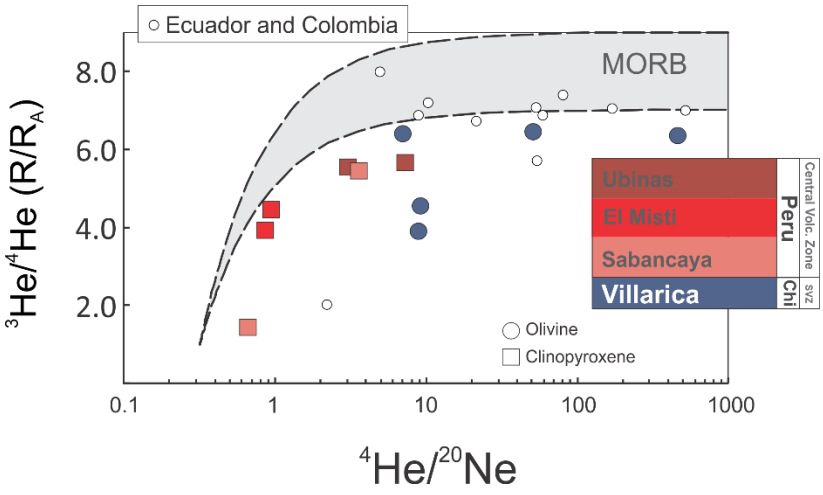

Figure 7.1: Plot of $^3He/^4He$ (R/R_A) vs $^4He/^{20}Ne$ for FIs hosted in olivines and pyroxenes (large symbols). The two curves describe a binary mixing between air and a magma source with He-isotope compositions of 7 and 9 R_A that describe the MORB range.

The systematics of Ne and Ar isotopes, along with He/Ne data shown in figure 7.1 highlight the air contamination in FIs, resulting in a mixing between mantle- and atmosphere-derived noble gases. Neon isotope results, in particular, clearly demonstrate that our data fall along the theoretical mixing line between air and a MORB- like mantle, defined by Sarda et al. (1988) and Moreira et al. (1998) at $^{21}Ne/^{22}Ne = 0.06$ and $^{20}Ne/^{22}Ne = 12.5$; Fig. 7.2). Similarly, $^{40}Ar/^{36}Ar$ values are well below the theoretical ratio in the mantle ($^{40}Ar/^{36}Ar$ up to 44,000; e.g., Burnard et al., 1997; Moreira et al., 1998) or typical mantle-derived samples (e.g., Kaneoka, 1983; Ozima and Podosek, 1983; Allègre et al., 1987), no exceeding $^{40}Ar/^{36}Ar \sim 360$, thus confirming the presence of a certain amount of contamination by atmosphere- derived fluids.

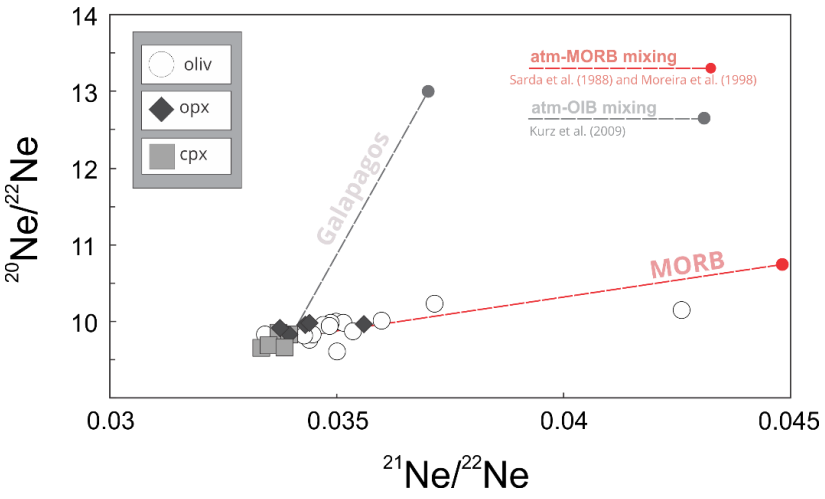

Figure 7.2: Diagram of $^{21}Ne/^{22}Ne$ vs. $^{20}Ne/^{22}Ne$. The red line represents binary mixing between air and a MORB mantle as defined by Sarda et al. (1988) and Moreira et al. (1998) at $^{21}Ne/^{22}Ne$ = 0.06 and $^{20}Ne/^{22}Ne$ = 12.5. The grey line indicates binary mixing between air and the OIB domain of the Galapagos Islands as determined by Kurz et al. (2009) at $^{21}Ne/^{22}Ne$ = 0.032 and $^{20}Ne/^{22}Ne$ = 12.5.

7.4.2. Diffusion-controlled isotope fractionation of He isotopes

Some of the $^{3}He/^{4}He$ reported here are most probably a result of low gas content and extensive post-entrapment He loss. In fact, all Peruvian samples recorded He concentrations below $1.3x10^{-13}$ mol g^{-1} (and as low as $0.08\ x10^{-13}$ mol g^{-1}). Just as previously reported for the orthopyroxenes analyzed from Cotopaxi (Ecuador), the lowest $^{3}He/^{4}He$ ratio obtained for the Peruvian segment (clinopyroxenes from Sabancaya) appears to be affected by a similar degree of diffusion-controlled isotope fractionation (Fig. 7.3; Tab. 7.1 contains all relevant information regarding noble gas contents in FIs discussed here). Other explanation for the lower $^{3}He/^{4}He$ ratios in pyroxenes is related to the closure temperatures of these phenocryst phases. Given their lower closure temperatures and higher He diffusion rates, pyroxenes are more susceptible to late-stage He exchange with a low $^{3}He/^{4}He$ source during ascent, presumably the surrounding crust.

Therefore, and despite the fact that all crystals may have undergone different extents of He loss during and post-crystallization, consistent isotope signatures obtained for the Peruvian arc segment (Central Volcanic Zone) may instead reflect assimilation of crustal isotope signatures and addition of radiogenic-^{4}He. Here, $^{3}He/^{4}He$ range from 2.1 to 6.4 R_A, but if excluded the lowest value obtained, all others are constrained between 6.0 and 6.4 R_A (obtained across all 3 volcanic systems).

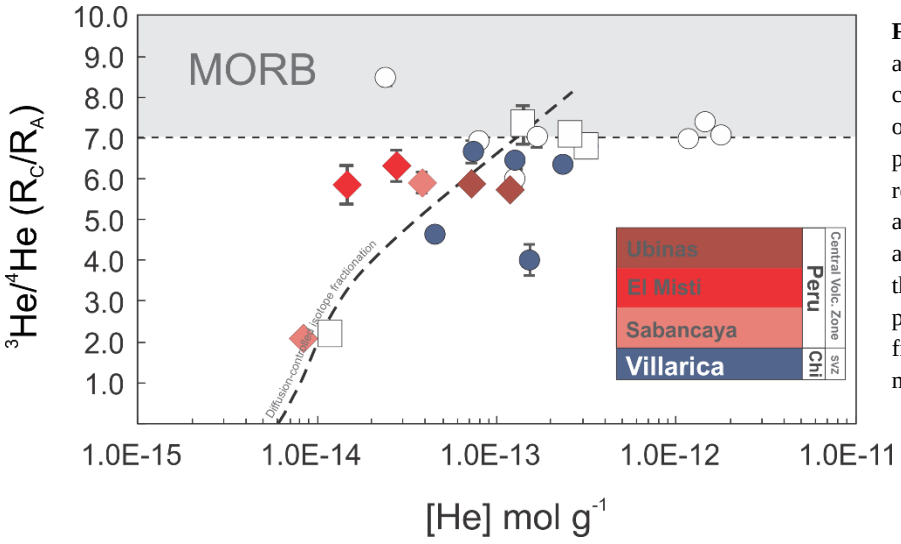

Figure 7.3: $^{3}He/^{4}He$ (R_C/R_A) ratios are plotted as a function of He concentrations in FIs (mol g^{-1}) from olivine (Villarica) and clinopyroxene phenocrysts (Peru). White symbols refer to data reported in chapter 6 and are show for comparison. The grey area shows the 8±1 MORB range, and the black dashed line represents the profile of diffusion-controlled fractionation assuming as an end-member a R_C/R_A of 7.0.

7.5 Subduction controls on Helium isotope signatures

Previous studies have argued that along-arc variations in slab thickness and subduction angle may be responsible for significantly distinct $^{3}He/^{4}He$ isotope signatures (e.g., Battaglia et al. 2018). This is based on the assumption that supercritical fluids bearing radiogenic-^{4}He (from the decay of U and Th hosted in subducted sediments) may reach higher depths and therefore alter the pristine composition of MORB-like fluids preserved at upper mantle depths.

Not only do the Andes show somewhat constant subduction angles along the trench, especially in comparison to CAVA segments where, as described by Battaglia et al. (2018), the slab dip increases up to 60°, they also show no evident correlation between Helium data reported here (and in the previous chapter for the NVZ segment) and small intra-arc variations of dip slab angle. Therefore, other mechanisms must be considered as responsibility for the reported $^{3}He/^{4}He$ variability of individual arc segments (NVZ, CVZ, SVZ) along the Andes.

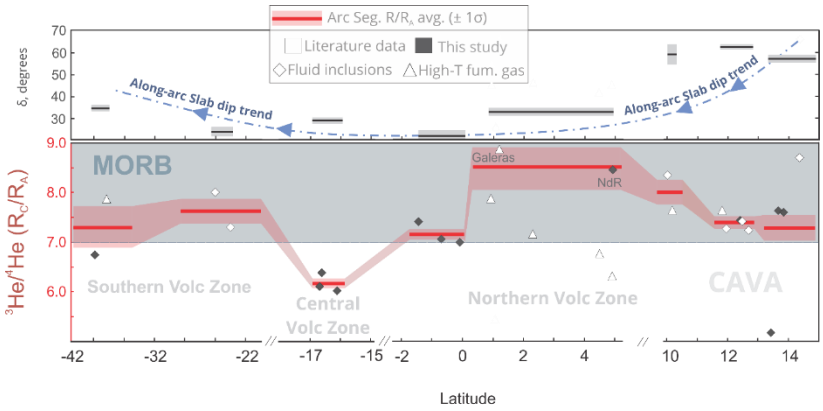

Figure 7.4: Along-arc variation of Helium isotope signatures (on the bottom). Shaded red area represents 1σ of the mean by averaging the highest $^{3}He/^{4}He$ for each volcanic system within their respective arc segment, and red lines represent $^{3}He/^{4}He$ averages for individual arc segments, including CAVA that it is here shown as comparison. On the top, variation of slab dip trend along CAVA and the Andes (data is from Syracuse, 2006). Note that preliminary data from CAVA is shown as a reference, but not discussed here.

7.6. Crustal controls on along-arc $^3He/^4He$ signatures

It is widely believed that crustal components are most significant in magmas erupted in the Central Volcanic Zone, where the crust is extremely thick (>70 km) and estimated rates of subduction

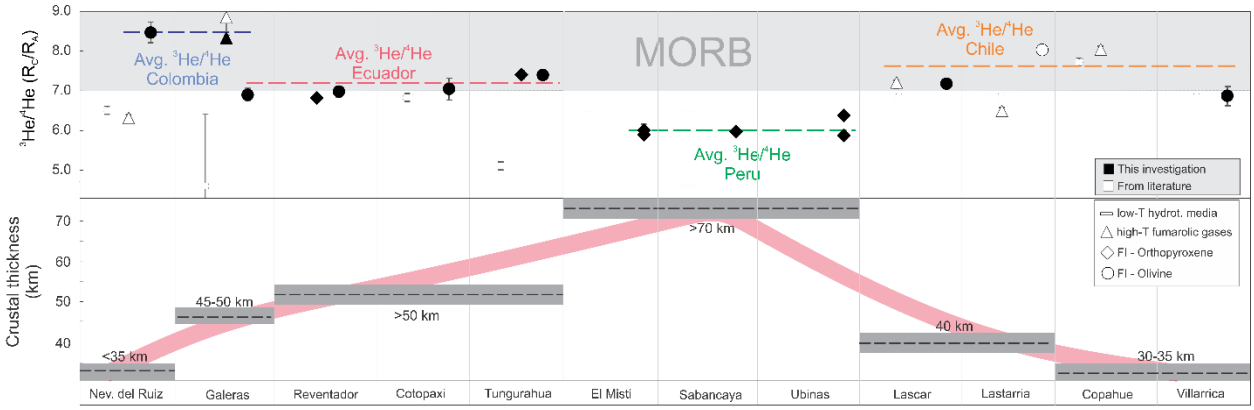

Figure 7.5: Crustal thickness variations along the Andes (see text for data provenance). Red shaded line represents the overall along-arc trend of the overlying crustal thickness. On the top, summary of results obtained from this investigation for $^3He/^4he$ isotope signatures for individual arc segments. Averages are estimated taking only into account the highest single value for each volcano.

erosion of the continental margin, possibly equivalent to as much as 4% of the volume of subducting oceanic crust, are also greatest due to the hyper-arid climate conditions and low sediment supply to the trench (e.g., Stern, 2004). However, this study found that crustal imprints may be possible to identify also in other arcs segments where crustal thickness doesn't reach values as high as those reported for the Central Volcanic Zone. In fact, all $^3He/^4He$ "end-members" suggested here for the different segments of the arc correlate to along-arc variations in crustal thickness (local and regional; Fig. 7.5) well documented in the literature (e.g., Beck et al., 1996).

In Colombia, where crustal thickness reaches values <35 km, values as high as 8.8 R_A have been reported (Sano et al., 1997 for Galeras fumarolic gases). Indeed, $^3He/^4He$ results obtained in olivine FIs from Nevado del Ruiz (~8.5 R_A) yield one of the highest ever $^3He/^4He$ values recorded in arc volcanism and are in agreement with even higher $^3He/^4He$ ratios measured in fumarolic gases in Galeras (as high as 8.8 R_A; Sano et al., 1997) and fumarolic gases sampled during this investigation and reported in the previous chapter (max R_A of ~ 8.3). Ecuador, on the other hand, sees an increment in crustal thickness (>50 km) and a rather lower $^3He/^4He$ "end-member" of about ~7.2 R_A. This trend becomes quite emphatic where crustal thickness is maximum. In Peru, none of maximum $^3He/^4He$ values obtained for Sabancaya, El Misti and Ubinas reached values higher than 6.5 R_A while showing small variations in between them. The consistency of these results coupled with crustal thickness variations along arc suggest that shallower processes may overwhelmingly control the isotopic signature of the fluids analyzed.

Furthermore, $CO_2/^3He$ molar ratios are systematically higher than the MORB average of $2x10^9$ (Marty and Jambon, 1995), especially for the Peru samples that reach values as high as $1.65x10^{10}$.The apparent excess of CO_2 (relative to ^3He) cannot be entirely due to physical or

chemical fractionation during the transfer of gases from the magmatic source to the surface. We therefore suggest that the effect of crustal outgassing may play a decisive role in the noble gas compositional trends identified along the volcanic arc (Fig. 7.6).

7.6 Conclusions

Temporal variations in Central Volcanic Zone magmas indicate that the extent of crustal contamination of CVZ magmas has increased through time, from prior to the Miocene to present day, as the crust has thickened to > 70 km (Lucassen et al., 2001). This is in agreement with the data reported for the Peruvian segment that shows higher extents of crustal contamination most possibly due to assimilation of radiogenic-^{4}He-rich from crustal lithologies through fluids migration into shallower crustal levels. Furthermore, this reinforces the argument discussed in the previous chapter for the controls on Helium isotope signature within the Northern Volcanic Zone, where crustal thickness anomalies around Nevado del Ruiz (<30km) and generally thicker overlying crust along the Ecuadorian Segment (>50km) appear to also correlate well with variations in the magmatic fluid's chemistry from these arc regions. Figure 7.3 puts in evidence the argument that along arc variations of crustal thickness may play a fundamental role in masking MORB-like signature of magmatic fluids at volcanic arcs.

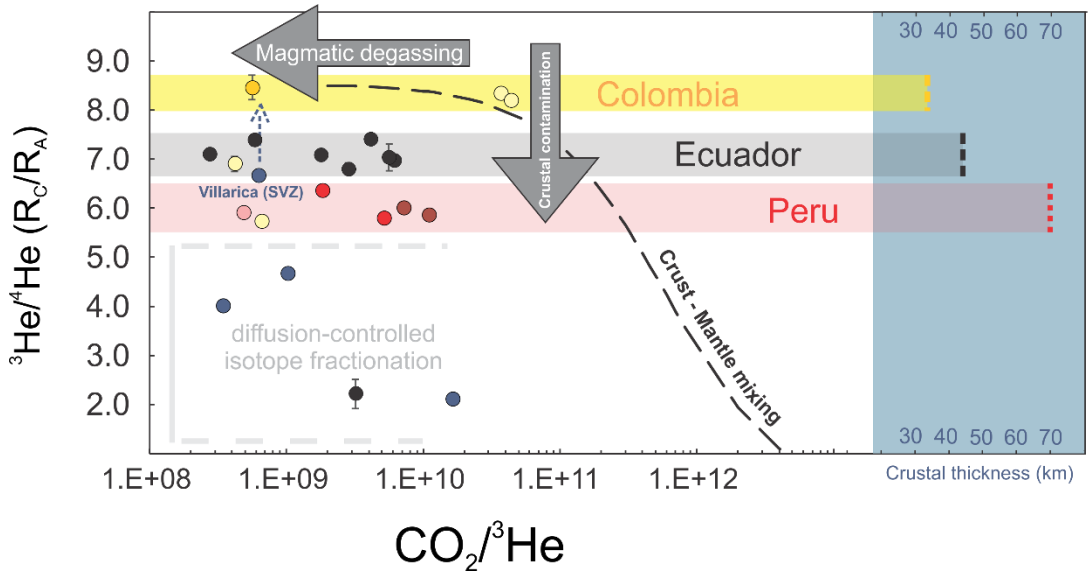

Figure 7.6: Variations of $CO_2/^3He$ vs. $^4He/^3He$ ratios in fluid inclusions from the Andean Volcanic Belt. "End-members" are given in shaded areas and represent $^3He/^4He$ ranges for individual arc segments. The along-arc correlation between 3He/4He and crustal thickness can be seen on the left; dashed lines represent avg. crustal thickness values for Peru, Colombia, and Ecuador reported in the literature (see text for references).

This dataset displays strong correlations with crustal structure that support the view that volcanic arc magmas interact with crustal wall rocks during their ascent and evolution. Therefore, we suggest that the most viable explanation for the lower $^3He/^4He$ ratios southward may be a result of prolonged diffusive exchange with radiogenic He from the surrounding crust (and associated fluids) occurring as ascends to arc regions of exceptionally thick continental crust. This agrees

with findings of others (Marty et al., 1994; Hilton et al., 1995; van Soest et al., 2002; Shaw et al., 2006) and underlines the sensitivity of He in identifying and assessing crustal contamination processes.

Acknowledgments

We are very grateful to all the staff members from *Observatorio Vulcanológico del INGEMMET,* especially to Fredy Apaza, for their help conducting all field work-related activities, including their crucial support on rock sampling. A special thanks also to Rigoberto Aguilar Contreras for his support throughout this investigation. I would also like to acknowledge prof. Philippe Robidoux for kindly assist us with samples from Villarica as well as the *Observatorio Volcanológico de Los Andes del Sur (OVDAS)*for their contribution in the field work portion of this project. We are also grateful to Mariano Tantillo and Mariagrazia Misseri for their support in sample preparation and noble gases analysis of FIs. The fieldwork portion of this work was funded by the DECADE initiative, from Deep Carbon Observatory - Alfred P. Sloan Foundation.

Chapter 7 – Table(s)

Table 7.1: Noble gas abundances and isotope ratios of olivine and pyroxene phenocrysts from Peru (Sabancaya, El Misti and Ubinas; CVZ) and Chile (Villarica; SVZ).

Table 7.1

Noble gas abundances and isotope ratios from mafic phenocrysts from Chile and Peru

Volcano	Sample ID	Sample details	Rock	Min. phase	Weight (g)	[He] $x10^{-13}$	[Ne] $x10^{-17}$	$[^{40}Ar]$ $x10^{-12}$	$[^{36}Ar]$ $x10^{-15}$	$[^{40}Ar^*]$ $x10^{-13}$	$^4He/^{20}Ne$	$^{20}Ne/^{22}Ne$	$^{21}Ne/^{22}Ne$	$^4He/^{40}Ar^*$	$^{40}Ar/^{36}Ar$	$^3He/^4He$ (R/R_A)	$^3He/^4He$ (R_C/R_A)
	Chile																
Villarrica	2015_A	Scoria	BA	Oliv		2.35	0.50	0.90	2.28	2.24	466.2	10.24 ± 0.16	0.0321 ± 0.0023	1.05			
	2015_B	Scoria	BA	Oliv		1.27	2.50	6.15	20.38	1.24	50.8	9.83 ± 0.03	0.0295 ± 0.0005	1.02	301.6 ± 0.1	6.43	6.46 ± 0.12
	HCH2A1	Pyroclast	BA	Oliv		0.72	10.32	1.03	3.40	0.21	7.0	9.81 ± 0.02	0.0293 ± 0.0003	3.39	301.8 ± 0.7	6.39	6.66 ± 0.13
	HCH2A4C	Lava flow	BA	Oliv		0.45	5.02	0.65	2.05	0.44	9.0	9.62 ± 0.07	0.0300 ± 0.0012	1.04	316.8 ± 0.2	4.52	4.66 ± 0.28
	HLN1A3D	Lapilli bomb	BA	Oliv		1.53	17.20	0.92	2.75	1.06	8.9	9.83 ± 0.04	0.0294 ± 0.0008	1.44	334.0 ± 0.3	3.89	4.01 ± 0.18
	Peru																
Ubinas	2014	Juvenile blocks	A	Cpx		0.72	9.86	6.95	19.75	11.19	7.3	9.67 ± 0.02	0.0284 ± 0.0003	0.06	352.2 ± 0.8	5.64	5.86 ± 0.16
	A&B	Juvenile blocks	A	Cpx		1.29	39.69	15.27	48.72	8.75	3.2	9.66 ± 0.02	0.0285 ± 0.0002	0.15	313.5 ± 0.04	5.49	6.01 ± 0.16
Sabancaya	Nov-28	Lava flow	A	Cpx		0.38	10.63	0.71	1.98	1.27	3.6	9.67 ± 0.03	0.0288 ± 0.0004	0.30	359.7 ± 0.2	5.45	5.92 ± 0.23
	SA-09-17 + SA-09-11	Lava flow	A	Cpx		0.08	12.57	0.93	2.92	0.70	0.7	9.77 ± 0.01	0.0292 ± 0.0003	0.12	319.4 ± 0.1	1.45	2.11 ± 0.18
El Misti	A	Lava flow	A	Cpx (green)		1.19	2.18	4.16	1.35	1.82	0.9	9.89 ± 0.01	0.0289 ± 0.00031	0.08	309.0 ± 0.06	3.93	5.80 ± 0.177
	B	Lava flow	A	Cpx (black)		0.78	1.31	4.84	1.56	2.32	0.9	9.84 ± 0.01	0.0297 ± 0.00019	0.12	310.4 ± 0.06	4.43	6.36 ± 0.190

Host rock chemical classification on the basis of SiO_2 contents: A (andesite), BA (basaltic-andesite)

Noble gas concentrations in mol g^{-1}

Mineral phases analyzed: Oliv (olivine), Opx (orthopyroxene), Cpx (clinopyroxene)

CHAPTER 8

Concluding remarks

This PhD investigation attempted to shine a light into the convoluted interplay between complex geodynamic settings and its controls on global geochemical cycles through subduction zones. Investigations of this nature encounter several obstacles which the scientific approaches described throughout this dissertation tried to resolve in order to improve our understanding of fluid's migration through the Earth's reservoirs and surface manifestations of volcanic activity that can help mitigate risks associated with highly hazardous volcanic phenomena.

In part this is due to the scarcity and/or type of noble gas media (bubbling springs, low- and high-temperature fumaroles, FIs) data (Fig. 8.1) that still dominates some arc regions where, despite persistent volcanic activity, Noble gas and/or volcanic gas compositions have not yet been analyzed or measured. As emphasized throughout this dissertation, the Andean Volcanic Belt, due to its extension, high-altitude volcanic chain and intense volcanic activity commonly found at some of biggest Andean gas emitters, remains understudied especially with regards to Noble gas constrains on magmatic fluids along the three volcanic regions, Northern, Central and Southern, originated through the subduction of the Nazca plate.

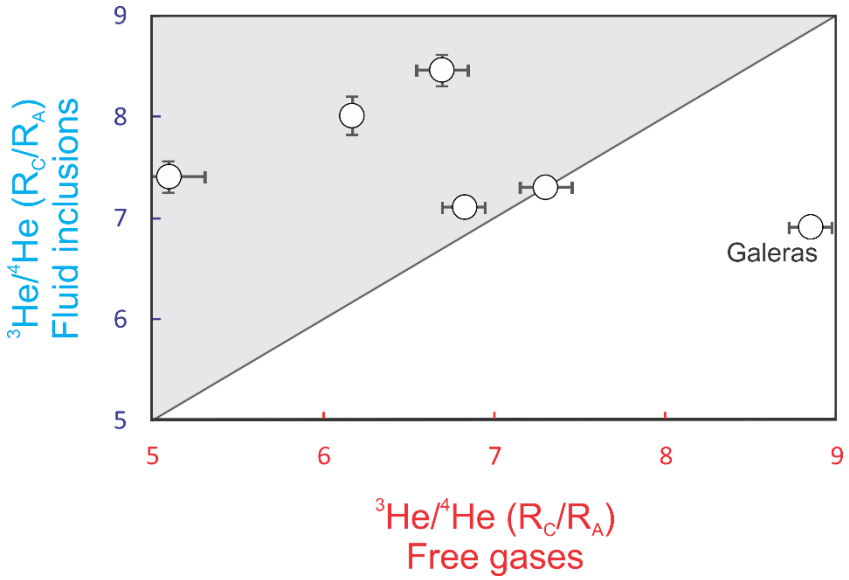

Figure 8.1: $^3He/^4He$ isotope signatures in FIs reported throughout this investigation and their comparison to free gases Helium ratios for the same volcano. Note that Galeras is the only volcanic system where higher $^3He/^4He$ ratios were registered in surface gases, rather than fluid inclusions.

Our new report on volcanic gas compositions and volatile fluxes for three of the most persistently active volcanoes in the CAS covered significant data gaps with regards to present-day volcanic emissions and total volatile budget of the Colombian Segment of the Northern Volcanic Zone. To the best of our knowledge, our observations represent the first ever results obtained for the major element composition of the Nevado del Ruiz volcanic plume, the strongest source of SO_2 in the

Northern Volcanic Zone (Carn et al., 2017). Our investigation estimated that subaerial emissions from CAS volcanoes contribute about 50% to the total subaerial CO_2 budget of the Andean Volcanic Belt and highlights the distinct magmatic CO_2/S_T signatures of Andean volcanoes, with emphasis on its northward increase and relation to along-arc variations in carbon-rich sediment input. Therefore, this study provides crucial evidence for slab-derived carbon to volcanic arc emissions and emphasizes the along-arc discrepancies in CO_2/S_T in Andean gases (~1 in Southern Chile).

This investigation also provided new helium isotope data here reported for the Ecuadorian, Colombian and Peruvian portions of the arc, which included the first helium isotope characterization of eruptive products from Reventador, Cotopaxi and Tungurahua (for which only peripheral, low-temperature data had been reported. To no surprise, this revealed significantly higher helium isotope signatures (Avg. R_C/R_A ~7.2) to those previously reported in literature. The highest $^3He/^4He$ ratio measured in rocks and gases for each individual volcanic system (7.0–8.5 R_A) is consistent with the typical MORB-range expected at arc volcanism (8±1 R_A). Excluding Galeras, for which previous studies had reported R_C/R_A values up to ~8.8 R_A, all values obtained in this study represent the highest R_C/R_A values ever reported for these volcanic systems.

The intra-segment consistency of our results and significant arc-scale variability here highlighted when averaging the highest $^3He/^4He$ from individual volcanic centers from Ecuador, Colombia and Peru, with estimated averages of ~7.2 R_A, ~8.5 R_A and ~6.0 R_A, respectively. However, no obvious correlation arises from the systematic differences in noble gas signatures put in evidence by this study and along-arc whole rock chemistry (e.g., Ba/La, La/Yb) from lavas and other eruptive products, which suggests that helium is predominantly of mantle origin and is largely independent of variations in the characteristics of the downgoing slab and variable along-arc subduction geometries. Therefore, the input of sediments from the subducted slab plays a minor role in the deep noble gas isotope signatures of arc fluids from Andean volcanism.

Instead, our study suggests that significant regional variations in crustal thickness, and the overall positive correlation between the overlying thickness of continental crust and helium isotope variations suggest that processes masking the pristine composition of deep mantle fluids may be happening at shallower depths, within the crust. Such interpretation has now been substantially improved upon, especially with data here acquired for Peruvian volcanoes, for which previous studies had not reported any noble gas data and where the overlying Andean continental crust reaches its maximum thickness.

It appears, therefore, that distinct factors control the along-arc variability of volcanic gas and noble gas compositions. Although volcanic gas compositions are time-dependent and may oscillate through periods of quiescent-to active volcanic activity, the current characterization of Andean subaerial fluids, namely CO_2/S_T ratios exhaustively explored here, seem to be decoupled to co-regional helium isotope signatures here improved upon by adding new data for previously uncharacterized volcanic systems. The first, as argued coherently throughout this dissertation, may

be controlled majorly by sediment materials transported via slab into the mantle wedge at subduction zones. The Carbon content of the sediments here ultimately drives the along-arc trend put in evidence by this study. On the other hand, noble gas signatures may be reworked at shallower depths within the subduction context, with crustal lithologies and overlying crustal thickness at volcanic arcs ultimately driving the variations here highlighted.

References

A

Abers, G. A., Plank, T. and Hacker, B. R., 2003. The wet Nicaraguan slab. Geophys. Res. Lett. 30, https://doi.org/10.1029/2002GL015649.

Abratis, M., Wörner, G., 2001. Ridge collision, slab-window formation, and the flux of Pacific asthenosphere into the Caribbean realm. Geology 29, 127–130. https://doi.org/10.1130/0091-7613(2001)029<0127:RCSWFA>2.0.CO;2

Aguilera, E., Almeida, E., Balseca, W., Barberi, F., Innocenti, F., Coltelli, M., Pasquare, G., 1988. El Reventador: an active volcano in the sub-andean zone of Ecuador. Rendiconti della Societa Italiana di Mineralogia e Petrologia 43, 853–875.

Aiuppa, A., Bitetto, M., Francofonte, V., Velasquez, G., Parra, C. B., Giudice, G., et al. (2017). A CO_2-gas precursor to the March 2015 Villarrica volcano eruption. Geochemistry, Geophysics, Geosystems, 18, 2120–2132. https://doi.org/10.1002/2017GC006892

Aiuppa, A., Federico, C., Giudice, G., Gurrieri, S., Liuzzo, M., Shinohara, H., et al. (2006). Rates of carbon dioxide plume degassing from Mount Etna volcano. Journal of Geophysical Research, 111, B09207. https://doi.org/10.1029/2006JB004307

Aiuppa, A., Fiorani, L., Santoro, S., Parracino, S., Nuvoli, M., Chiodini, G., et al. (2015). New ground-based LIDAR enables volcanic CO2 flux measurements. Scientific Reports, 5. https://doi.org/10.1038/srep13614

Aiuppa, A., Fischer, T. P., Plank, T., and Bani, P. (2019). CO2 flux emissions from the Earth's most actively degassing volcanoes, 2005–2015. Scientific Reports, 9(5442). https://doi.org/10.1038/s41598-019-41901-y

Aiuppa, A., Fischer, T. P., Plank, T., Robidoux, P., and Di Napoli, R. (2017). Along-arc and inter-arc variations in volcanic gas CO2/ST ratios reveal dual source of carbon in arc volcanism. Earth-Science Reviews, 168, 24–47. https://doi.org/10.1016/j.earscirev.2017.03.005

Aiuppa, A., Frederico, C., Guidice, G., and Gurrieri, S. (2005). Chemical mapping of a fumarolic field: La Fossa Crater, Vulcano Island (Aeolian Islands, Italy). Geophysical Research Letters, 32, L13309. https://doi.org/10.1029/2005GL023207

Aiuppa, A., Giudice, G., Gurrieri, S., Liuzzo, M., Burton, M., Caltabiano, T., et al. (2008). Total volatile flux from Mount Etna. Geophysical Research Letters, 35, L24302. https://doi.org/10.1029/2008GL035871

Aiuppa, A., Robidoux, P., Tamburello, G., Conde, V., Galle, B., Avard, G., et al. (2014). Gas measurements from the Costa Rica–Nicaragua volcanic segment suggest possible along-arc variations in volcanic gas chemistry. Earth and Planetary Science Letters, 407, 134–147. https://doi.org/10.1016/j.epsl.2014.09.041

Allègre, C.J., Staudacher, T., Sarda, P., 1987. Rare gas systematics: formation of the atmosphere, evolution and structure of the Earth's mantle. Earth Planet. Sci. Lett. 81, 127–150. https://doi.org/10.1016/0012-821X(87)90151-8

Ancellin, M-A., Samaniego, P., Vlast, I., Nauret, F., Gannoun, A., Hidalgo, S. 2017. Across-arc versus along-arc Sr-Nd-Pb isotope variations in the Ecuadorian volcanic arc, Geochem. Geophys.Geosyst., 18 https://doi.org/10.1002/2016GC006679

Andres, R. J., and Kasgnoc, A. D. (1998). A time-averaged inventory of subaerial volcanic sulfur emissions. Journal of Geophysical Research, 103, 25251–25261. https://doi.org/10.1029/98JD02091

Annen, C., Blundy, J.D., Sparks, R.S.J., 2006. The genesis of intermediate and silicic magmas in deep crustal hot zones. J. Petrol. 47, 505–539. https://doi.org/10.1093/petrology/egi084

Arango, E. E., Buitrago, A. J., Cataldi, R., Ferrara, G. C., Panichi, C., and Villegas, V. J. (1970). Preliminary study on the Ruiz Geothermal Project (Colombia). Geothermics, 2, 43–56. https://doi.org/10.1016/0375-6505(70)90005-2

B

Ballentine, C.J., Burgess, R., Marty, B., 2002. Tracing fluid origin, transport and interaction in the crust. Rev. Mineral. Geochemistry 47. https://doi.org/10.2138/rmg.2002.47.13

Ballentine, C.J., Marty, B., Lollar, B.S., Cassidy, M., 2005. Neon isotopes constrain convection and volatile origin in the Earth's mantle. Nature 433, 33–38. https://doi.org/10.1038/nature03182

Bani, P., Tamburello, G., Rose-Koga, E. F., Liuzzo, M., Aiuppa, A., Cluzel, N., et al. (2018). Dukono, the predominant source of volcanic degassing in Indonesia, sustained by a depleted Indian-MORB. Bulletin of Volcanology, 80(1). https://doi.org/10.1007/s00445-017-1178-9

Barazangi, M., Isacks, B.L., 1979. Subduction of the Nazca plate beneath Peru: evidence from spatial distribution of earthquakes. Geophys. J. R. Astron. Soc. 57, 537–555. https://doi.org/10.1111/j.1365-246X.1979.tb06778.x

Barragan, R., Geist, D., Hall, M., Larson, P., Kurz, M., 1998. Subduction controls on the compositions of lavas from the Ecuadorian Andes. Earth Planet. Sci. Lett. 154, 153–166. https://doi.org/10.1016/s0012-821x(97)00141-6

Barry, P. H., de Moor, J. M., Giovannelli, D., Schrenk, M., Hummer, D. R., Lopez, T., et al. (2019). Forearc carbon sink reduces long-term volatile recycling into the mantle. Nature, 568, 487–492. https://doi.org/10.1038/s41586-019-1131-5

Battaglia, A., Bitetto, M., Aiuppa, A., Rizzo, A.L., Chigna, G., Watson, I.M., D'Aleo, R., Juárez Cacao, F.J., de Moor, M.J., 2018. The magmatic gas signature of Pacaya Volcano, with implications for the volcanic CO_2 flux from Guatemala. Geochemistry, Geophys. Geosystems 19, 667–692. https://doi.org/10.1002/2017GC007238

Benjamin, E.R., Plank, T., Wade, J.A., Kelley, K.A., Haun, E.H., Alvarado, G.E., 2007. High water contents in basaltic magmas from Irazu Volcano, Costa Rica. J. of Volcanol. And Geotherm. Res. 168, 68-92. https://doi.org/10.1016/j.jvolgeores.2007.08.008

Bijwaard, H., Spakman, W., Engdahl, E.R., 1998. Closing the gap between regional and global travel time tomography. J. Geophys. Res. Solid Earth 103, 30,055–30,078. https://doi.org/10.1029/98jb02467

Boletines Informativos de actividad volcánica, Servicio Geológico Colombiano—Portal Servicio Geológico Colombiano [https://www2.sgc. gov.co/Noticias/Paginas/Boletines.aspx]

Bourdon, E., Eissen, J.P., Gutscher, M.A., Monzier, M., Hall, M.L., Cotten, J., 2003. Magmatic response to early aseismic ridge subduction: The Ecuadorian margin case (South America). Earth Planet. Sci. Lett. 205, 123–138. https://doi.org/10.1016/S0012-821X(02)01024-5

Boudoire, A.L. Rizzo, A. Di Muro, F. Grassa, M. Liuzzo. (2018) Extensive CO_2 degassing in the upper mantle beneath oceanic basaltic volcanoes: first insights from Piton de la Fournaise volcano (La Réunion Island).

Burton, M., and Sawyer, G. (2013). Deep carbon emissions from volcanoes. Reviews in Mineralogy and Geochemistry, 75, 323–354. https://doi.org/10.2138/rmg.2013.75.11

Bryant, J.A., Yogodzinski, G.M., Hall, M.L., Lewicki, J.L., Bailey, D.G., 2006. Geochemical constraints on the origin of volcanic rocks from the Andean Northern volcanic zone, Ecuador. J. Petrol. 47, 1147–1175. https://doi.org/10.1093/petrology/egl006

Burnard, P., 2013. The noble gases as geochemical tracers, The Noble Gases as Geochemical Tracers. https://doi.org/10.1007/978-3-642-28836-4

Burnard, P., Graham, D., Turner, G., 1997. Vesicle-specific noble gas analyses of "popping rock": Implications for primordial noble gases in earth. Science (80-.). 276, 568–571. https://doi.org/10.1126/science.276.5312.568

C

Calvache, M. L. (1990). Geology and volcanology of the recent evolution of Galeras volcano, Colombia. M. S Thesis, Louisiana State University.

Calvache, M. L., Cortes, G. P. J., and Williams, S. N. (1997). Stratigraphy and chronology of the Galeras volcanic complex, Colombia. Journal of Volcanology and Geothermal Research, 77, 5–19. https://doi.org/10.1016/S0377-0273(96)00083-2

Calvache, M. L., and Williams, S. N. (1997a). Emplacement and petrological evolution of the andesitic dome of Galeras volcano, 1990–1992. Journal of Volcanology and Geothermal Research, 77, 57–69. https://doi.org/10.1016/S0377-0273(96)00086-8

Calvache, M. L., and Williams, S. N. (1997b). Geochemistry and petrology of the Galeras Volcanic Complex, Colombia. Journal of Volcanology and Geothermal Research, 77, 21–38. https://doi.org/10.1016/S0377-0273(96)00084-4

Capasso, G., Carapezza, M.L., Federico, C., Inguaggiato, S., Rizzo, A., 2005. Geochemical monitoring of the 2002-2003 eruption at Stromboli volcano (Italy): Precursory changes in the carbon and helium isotopic composition

of fumarole gases and thermal waters. Bull. Volcanol. 68, 118–134. https://doi.org/10.1007/s00445-005-0427-5

Caracausi, A., Italiano, F., Paonita, A., Rizzo, A., Nuccio, P.M., 2003. Evidence of deep magma degassing and ascent by geochemistry of peripheral gas emissions at Mount Etna (Italy): Assessment of the magmatic reservoir pressure. J. Geophys. Res. Solid Earth 108, 1–15. https://doi.org/10.1029/2002jb002095

Carn, S. A., Fioletov, V. E., McLinden, C. A., Li, C., and Krotkov, N. A. (2017). A decade of global volcanic SO2 emissions measured from space. Scientific Reports, 7, 44095. https://doi.org/10.1038/srep44095

Carr, M.J., Feigenson, M.D., Bennett, E.A., 1990. Incompatible element and isotopic evidence for tectonic control of source mixing and melt extraction along the Central American arc. Contrib. to Mineral. Petrol. 105, 369–380. https://doi.org/10.1007/BF00286825

Carr, M.J., 1984. Symmetrical and segmented variation of physical and geochemical characteristics of the central american volcanic front. J. Volcanol. Geotherm. Res. 20, 231–252. https://doi.org/10.1016/0377-0273(84)90041-6

Carr, M.J., Saginor, I., Alvarado, G.E., Bolge, L.L., Lindsay, F.N., Milidakis, K., Turrin, B.D., Feigenson, M.D., Swisher, C.C., 2007. Element fluxes from the volcanic front of Nicaragua and Costa Rica. Geochemistry, Geophys. Geosystems 8. https://doi.org/10.1029/2006GC001396

Chiodini, G., Cionib, R., Guidib, M., Raco, B., and Marinic, L. (1998). Soil CO2 flux measurements in volcanic and geothermal areas. Applied Geochemistry, 13, 543–552. https://doi.org/10.1016/S0883-2927(97)00076-0

Craig, H., Lupton, J.E., 1976. Primordial neon, helium, and hydrogen in oceanic basalts. Earth Planet. Sci. Lett. 31, 369–385. https://doi.org/10.1016/0012-821X(76)90118-7

D

Dasgupta, R. (2013). Ingassing, storage, and outgassing of terrestrial carbon through geologic time. Reviews in Mineralogy and Geochemistry, 75, 183–229. https://doi.org/10.2138/rmg.2013.75.7

de Moor, J. M., Aiuppa, A., Avard, G., Wehrmann, H., Dunbar, N., Muller, C., et al. (2016). Turmoil at Turrialba volcano (Costa Rica): Degassing and eruptive processes inferred from high-frequency gas monitoring. Journal of Geophysical Research: Solid Earth, 121, 5761–5775. https://doi.org/10.1002/2016JB013150

de Moor, J. M., Kern, C., Avard, G., Muller, C., Aiuppa, A., Saballos, A., et al. (2017). A new sulfur and carbon degassing inventory for the Southern Central American Volcanic Arc: The importance of accurate time series datasets and implications for global volatile budgets. Geochemistry, Geophysics, Geosystems, 18, 4437–4468. https://doi.org/10.1002/2017GC007141

Dee, D. P., Uppala, S. M., Simmons, A. J., Berrisford, P., Poli, P., Kobayashi, S., et al. (2011). The ERA-Interim reanalysis: Configuration and performance of the data assimilation system. Quarterly Journal of the Royal Meteorological Society, 137, 553–597. https://doi.org/10.1002/qj.828

Dinger, F., Bobrowski, N., Simon, W., Bredemeyer, S., Hidalgo, S., Arellano, S., et al. (2018). Periodicity in the BrOSO2 molar ratios in the volcanic gas plume of Cotopaxi and its correlation with the Earth tides during the eruption in 2015. Solid Earth, 9, 247–266. https://doi.org/10.5194/se-9-247-2018

Di Piazza, A., Rizzo, A.L., Barberi, F., Carapezza, M.L., De Astis, G., Romano, C., Sortino, F., 2015. Geochemistry of the mantle source and magma feeding system beneath Turrialba volcano, Costa Rica. Lithos 232, 319–335. https://doi.org/10.1016/j.lithos.2015.07.012

E

Edmonds, M., Herd, R., Galle, B., and Oppenheimer, C. (2003). Automated, high time-resolution measurements of SO_2 flux at Soufrière Hills Volcano, Montserrat. Bulletin of Volcanology, 65, 578–586. https://doi.org/10.1007/s00445-003-0286-x

Edmonds, M., Gerlach, T. M., 2007. Vapor segregation and loss in basaltic melts. Geology 35, 751–754.

F

Farley, K.A., Neroda, E., 1998. Noble gases in the Earth's mantle. Annu. Rev. Earth Planet. Sci. 26, 189–218. https://doi.org/10.1146/annurev.earth.26.1.189.

Feininger, T., Seguin, M.K., 1983. Simple Bouguer gravity anomaly field and the inferred crustal structure of continental Ecuador. Geology 11, 40–44. https://doi.org/10.1130/0091-7613(1983)11<40:SBGAFA>2.0.CO;2

Finnegan, D. L., Kotra, J. P., Hermann, D. M. and Zoeller, W. H. (1989). The use of 7LiOH-impregnated filters for the collection of acidic gases and analysis by instrumental neutron activation analysis, Bull. Volcanol., 51, 83–87,1989.

Fischer, T. P. (2008). Fluxes of volatiles (H2O, CO2, N2, Cl, F) from arc volcanoes. Geochemical Journal, 42, 21–38. https://doi.org/10.2343/ geochemj.42.21

Fischer, T. P., and Chiodini, G. (2015). Volcanic, magmatic and hydrothermal gases. The Encyclopedia of Volcanoes, 2, 779–796. https://doi.org/10.1016/B978-0-12-385938-9.00045-6

Fischer, T. P., Sturchio, N. C., Stix, J., Arehart, G. B., Counce, D., and Williams, S. N. (1997). Chemical and isotopic composition of fumarolic gases and spring discharges from Galeras volcano, Colombia. Journal of Volcanology and Geothermal Research, 77, 229–253. https://doi.org/10.1016/S0377-0273(96)00096-0

Fischer, T.P., Takahata, N., Sano, Y., Sumino, H., Hilton, D.R., 2005. Nitrogen isotopes of the mantle: Insights from mineral separates. Geophys. Res. Lett. 32. https://doi.org/10.1029/2005GL022792

Fukao, Y., Widiyantoro, S., Obayashi, M., 2001. Stagnant slabs in the upper and lower mantle transition region. Rev. Geophys. 39, 291–323. https://doi.org/10.1029/1999RG000068

G

Galle, B., Johansson, M., Rivera, C., Zhang, Y., Kihlman, M., Kern, C., et al. (2010). Network for Observation of Volcanic and Atmospheric Change (NOVAC)—A global network for volcanic gas monitoring: Network

layout and instrument description. Journal of Geophysical Research, 115, D05304. https://doi.org/10.1029/2009JD011823

Galle, B., Oppenheimer, C., Geyer, A., McGonigle, A., Edmonds, M., and Horrocks, L. (2003). A miniaturized ultraviolet spectrometer for remote sensing of SO2 fluxes: A new tool for volcano surveillance. Journal of Volcanology and Geothermal Research, 119, 241–254. https://doi.org/10.1016/S0377-0273(02)00356-6

Ganne, J., Feng, X., 2017. Geochemistry, Geophysics, Geosystems. Geochemistry Geophys. Geosystems 1–26. https://doi.org/10.1002/2016GC006679.Received

Garrison, J.M., Davidson, J.P., Hall, M., Mothes, P., 2011. Geochemistry and petrology of the most recent deposits from Cotopaxi Volcano, Northern Volcanic Zone, Ecuador. J. Petrol. 52, 1641–1678. https://doi.org/10.1093/petrology/egr023

Gazel, E., Hoernle, K., Carr, M.J., Herzberg, C., Saginor, I., Bogaard, P. Van Den, Hauff, F., Feigenson, M., Swisher, C., 2011. Plume – subduction interaction in southern Central America: Mantle upwelling and slab melting. Lithos 121, 117–134. https://doi.org/10.1016/j.lithos.2010.10.008

Giggenbach, W. F., Garcia, N. P., Londoño, A. C., Rodriguez, L. V., Rojas, N. G., and Calvache, M. L. (1990). The chemistry of fumarolic vapor and thermal-spring discharges from the Nevado del Ruiz volcanic-magmatic-hydrothermal system, Colombia. Journal of Volcanology and Geothermal Research, 42, 13–39. https://doi.org/10.1016/0377-0273(90)90067-P

Global Volcanism Program (2013a). Galeras (351080) in Volcanoes of the world, v. 4.7.7. Venzke, E (ed.). Smithsonian Institution. Downloaded 20 Dec 2018 (https://volcano.si.edu/volcano.cfm?vn=351080). https://doi.org/10.5479/siGVPVOTW42013

Global Volcanism Program (2013b). Nevado del Ruiz (351020) in Volcanoes of the world, v. 4.7.7. Venzke, E (ed.). Smithsonian Institution. Downloaded 20 Dec 2018 (https://volcano.si.edu/volcano.cfm?vn=351020). https://doi.org/10.5479/siGVPVOTW42013

Global Volcanism Program (2013c). Puracé (351060) in Volcanoes of the world, v. 4.7.7. Venzke, E (ed.). Smithsonian Institution. Downloaded 20 Dec 2018 (https://volcano.si.edu/volcano.cfm?vn=351060). https://doi.org/10.5479/siGVPVOTW42013

Graham, D.W., 2002. Noble gas isotope geochemistry of mid-ocean ridge and ocean island basalts: Characterization of mantle source reservoirs. Rev. Mineral. Geochemistry 47, 247–317. https://doi.org/10.2138/rmg.2002.47.8

Graham, D.W., Hanan, B.B., Hémond, C., Blichert-Toft, J., Albarède, F., 2014. Helium isotopic textures in Earth's upper mantle. Geochemistry, Geophys. Geosystems 15, 2048–2074. https://doi.org/10.1002/2014GC005264

Guillier. B., Chatelain, J.L., Jaillard, E., Yepes, H., Poupinet, G., Fels, J. F., 2001. Seismological evidence on the geometry of the orogenic system in central-northern Ecuador (South America). Geophys. Res. Lett. 28, 3749-3752. https://doi.org/10.1029/2001GL013257

Gurenko, A. A., Hoernle, K. A., Hauff, F., Schmincke, H. U., Han, D., Miura, Y. N., and Kaneoka, I., 2006. Major, trace element and Nd-Sr-Pb-O-He-Ar isotope signatures of shield stage lavas from the central and western Canary Islands: insights into mantle and crustal processes. Chem. Geol. 233, 75–112. https://doi.org/10.1016/j.chemgeo.2006.02.016

Gutscher, M.A., Malavieille, J., Lallemand, S., Collot, J.Y., 1999. Tectonic segmentation of the North Andean margin: Impact of the Carnegie Ridge collision. Earth Planet. Sci. Lett. 168, 255–270. https://doi.org/10.1016/S0012-821X(99)00060-6

H

Hall, M. L. (1990). Chronology of the principal scientific and governmental actions leading up to the November 13, 1985 eruption of Nevado del Ruiz, Colombia. Journal of Volcanology and Geothermal Research, 42, 101–115. https://doi.org/10.1016/03770273(90) 90072-N

Hacker, B.R., Kelemen, P.B., Behn, M.D., 2011. Differentiation of the continental crust by relamination. Earth Planet. Sci. Lett. 307, 501–516. https://doi.org/10.1016/j.epsl.2011.05.024

Hall, M.L., Samaniego, P., Le Pennec, J.L., Johnson, J.B., 2008. Ecuadorian Andes volcanism: A review of Late Pliocene to present activity. J. Volcanol. Geotherm. Res. 176, 1–6. https://doi.org/10.1016/j.jvolgeores.2008.06.012

Hall, M.L., Robin, C., Beate, B., Mothes, P., Monzier, M., 1999. Tungurahua Volcano, Ecuador: Structure, eruptive history and hazards. J. Volcanol. Geotherm. Res. 91, 1–21. https://doi.org/10.1016/S0377-0273(99)00047-5

Hall, M., Mothes, P., 2008. The rhyolitic-andesitic eruptive history of Cotopaxi volcano, Ecuador. Bull. Volcanol. 70, 675–702. https://doi.org/10.1007/s00445-007-0161-2

Hart, S.R., 1984. He diffusion in olivine. Earth Planet. Sci. Lett. 70, 297–302. https://doi.org/10.1016/0012-821X(84)90014-1

Harrison, D., Barry, T., and Turner, G., 2004. Possible diffusive fractionation of helium isotopes in olivine and clinopyroxene phenocrysts. Eur. J. Mineral., 16, 213-220. https://doi.org/10.1127/0935-1221/2004/0016-0213

Hauri, E., 2002. SIMS analysis of volatiles in silicate glasses, 2: Isotopes and abundances in Hawaiian melt inclusions. Chem. Geol. 183, 115–141. https://doi.org/10.1016/S0009-2541(01)00374-6

Heier, K. S., and Adams, J. A. S. (1965). Concentration of radioactive elements in deep crustal material. Geochimica et Cosmochimica Acta, 29, pp. 53-61. doi:10.1016/0016-7037(65)90078-5

Hickey, R.L., Frey, F.A., Gerlach, D.C., Lopez-Escobar, L., 1986. Multiple sources for basaltic arc rocks from the southern volcanic zone of the Andes (34°–41°S): Trace element and isotopic evidence for contributions from subducted oceanic crust, mantle, and continental crust. J. Geophys. Res. 91, 5963. https://doi.org/10.1029/jb091ib06p05963

Hidalgo, S., Battaglia, J., Arellano, S., Sierra, D., Bernard, B., Rene, P., et al. (2018). Evolution of the 2015 Cotopaxi eruption revealed by combined geochemical and seismic observations. Geochemistry, Geophysics, Geosystems, 19, 2087–2108. https://doi.org/10.1029/2018GC007514

Hidalgo, S., Battaglia, J., Arellano, S., Sierra, D., Parra, R., Kelly, P., et al. (2016). Geochemical signals of unrest and eruption of Cotopaxi volcano in 2015 (conference paper). Cities on Volcanoes, 9.

Hilton, D. R., Fischer, T. P., and Marty, B. (2002). Noble gases and volatile recycling at subduction zones. Reviews in Mineralogy and Geochemistry, 47(1), 319–370. https://doi.org/10.2138/rmg.2002.47.9

Hilton, D.R., Hammerschmidt, K., Teufel, S., Friedrichsen, H., 1993. Helium isotope characteristics of Andean geothermal fluids and lavas. Earth Planet. Sci. Lett. 120, 265–282. https://doi.org/10.1016/0012-821X(93)90244-4

Hildreth, W. and Moorbath, S. (1988). Crustal contributions to arc magmatism in the Andes of Central Chile. Contrib. Mineral Petrol., 98, pp. 455-489. doi:10.1007/BF00372365

Hoernle, K., Werner, R., Morgan, J.P., Garbe-Schonberg, D., Bryce, J., Mrazek, J., 2000. Existence of complex spatial zonation in the Galapagos plume for at least 14 m.y. Geology 28, 435-438. https://doi.org/10.1130/0091-7613(2000)28<435:EOCSZI>2.0.CO;2

Huang, Y., Chubakov, V., Mantovani, F., Rudnick, R. L., and McDonough, W. F. (2013). A reference Earth model for the heat-producing elements and associated geoneutrino flux. Geochem. Geophys. Geosyst. 14, pp. 2003–29. doi:doi.org/10.1002/ggge.20129

J

Jackson, C.R.M., Parman, S.W., Kelley, S.P., Cooper, R.F., 2013. Noble gas transport into the mantle facilitated by high solubility in amphibole. Nat. Geosci. 6, 562–565. https://doi.org/10.1038/ngeo1851

Jarrard, R. D. (1986). Relations among subduction parameters. Reviews of Geophysics, 24, 217–284. https://doi.org/10.1029/RG024i002p00217

Jarrard, R. D. (2003). Subduction fluxes of water, carbon dioxide, chlorine, and potassium. Geochemistry, Geophysics, Geosystems, 4(5), 8905. https://doi.org/10.1029/2002GC000392

Jean-Baptiste, P., Allard, P., Fourré, E., Bani, P., Calabrese, S., Aiuppa, A., Gauthier, P.J., Parello, F., Pelletier, B., Garaebiti, E., 2016. Spatial distribution of helium isotopes in volcanic gases and thermal waters along the Vanuatu (New Hebrides) volcanic arc. J. Volcanol. Geotherm. Res. 322, 20–29. https://doi.org/10.1016/j.jvolgeores.2015.09.026

Johansson, M., Galle, B., Zhang, Y., Rivera, C., Deliang, C., and Wyser, K. (2009). The dual-beam mini-DOAS technique—Measurements of volcanic gas emission, plume height and plume speed with a single instrument. Bulletin of Volcanology, 71, 747–751. https://doi.org/10.1007/s00445-008-0260-8

Johnston, S.T., Thorkelson, D.J., 1997. Cocos–Nazca slab window beneath Central America. Earth and Planetary Science Letters 146, 465–474. https://doi.org/10.1016/S0012-821X(96)00242-7

K

Kaneoka, I., 1983. Noble gas constrains on the layered structure of the mantle. Nature 302, 698–700. https://doi.org/10.1038/302698a0

Kantzas, E. P., and McGonigle, A. J. S. (2008). Ground based ultraviolet remote sensing of volcanic gas plumes. Sensors, 8. https://doi.org/ 10.3390/s8031559

Kantzas, E. P., McGonigle, A. J. S., Tamburello, G., Aiuppa, A., and Bryant, R. G. (2010). Protocols for UV camera volcanic SO_2 measurements. Journal of Volcanology and Geothermal Research, 194(1-3), 55–60. https://doi.org/10.1016/j.jvolgeores.2010.05.003

Kelemen, P. B., and Manning, C. E. (2015). Reevaluating carbon fluxes in subduction zones, what goes down, mostly comes up. PNAS, 112(30), 3997–4006. https://doi.org/10.1073/pnas.1507889112

Kern, C., Werner, C., Elias, T., Sutton, A., and Lubcke, P. (2013). Applying UV cameras for SO2 detection to distant or optically thick volcanic plumes. Journal of Volcanology and Geothermal Research, 262, 80–89. https://doi.org/10.1016/j.jvolgeores.2013.06.009

Kerr, A.C., Kempton, P.D., Thompson, R.N., 1995. Crustal assimilation during turbulent magma ascent (ATA); new isotopic evidence from the Mull Tertiary lava succession, N. W. Scotland. Contrib. to Mineral. Petrol. 119, 142–154. https://doi.org/10.1007/BF00307277

Kimura, J.I., Kawabata, H., 2015. Geochemistry, Geophysics, Geosystems. Geochemistry Geophys. Geosystems 16, 267–300. https://doi.org/10.1002/2014GC005684.Key

Kobayashi, M., Sumino, H., Nagao, K., Ishimaru, S., Arai, S., Yoshikawa, M., Kawamoto, T., Kumagai, Y., Kobayashi, T., Burgess, R., Ballentine, C.J., 2017. Slab-derived halogens and noble gases illuminate closed system processes controlling volatile element transport into the mantle wedge. Earth Planet. Sci. Lett. 457, 106–116. https://doi.org/10.1016/j.epsl.2016.10.012

Kurz, M.D., Curtice, J., Fornari, D., Geist, D., Moreira, M., 2009. Primitive neon from the center of the Galápagos hotspot. Earth Planet. Sci. Lett. 286, 23–34. https://doi.org/10.1016/j.epsl.2009.06.008

L

Lages, J., Chacón, Z., Burbano, V., Meza, L., Arellano, S., Liuzzo, M., Giudice, G., Aiuppa, A., Bitetto, M., López, C., 2019. Volcanic Gas Emissions Along the Colombian Arc Segment of the Northern Volcanic Zone (CAS-NVZ): Implications for volcano monitoring and volatile budget of the Andean Volcanic Belt. Geochemistry, Geophys. Geosystems 1–25. https://doi.org/10.1029/2019gc008573

Le Pennec, J.L., Jaya, D., Samaniego, P., Ramón, P., Moreno Yánez, S., Egred, J., van der Plicht, J., 2008. The AD 1300-1700 eruptive periods at Tungurahua volcano, Ecuador, revealed by historical narratives, stratigraphy and radiocarbon dating. J. Volcanol. Geotherm. Res. 176, 70–81. https://doi.org/10.1016/j.jvolgeores.2008.05.019

Lee, C.T.A., Bachmann, O., 2014. How important is the role of crystal fractionation in making intermediate magmas? Insights from Zr and P systematics. Earth Planet. Sci. Lett. 393, 266–274. https://doi.org/10.1016/j.epsl.2014.02.044

Leeman, W.P., 1983. The influence of crustal structure on compositions of subduction-related magmas. J. Volcanol. Geotherm. Res. 18, 561–588. https://doi.org/10.1016/0377-0273(83)90026-4

Lewicki, J.L., Fischer, T., Williams, S.N., 2000. Chemical and isotopic compositions of fluids at Cumbal Volcano, Colombia: Evidence for magmatic contribution. Bull. Volcanol. 62, 347–361. https://doi.org/10.1007/s004450000100

Lübcke, P., Bobrowski, N., Illing, S., Kern, C., Nieves, J. M. A., Vogel, L., et al. (2012). On the absolute calibration of SO2 cameras. Atmospheric Measurement Techniques, 6, 677–696. https://doi.org/10.5194/amt-6-677-2013

M

Maldonado, L. F. M., Inguaggiato, S., Jaramillo, M. T., Garzón, G., and Mazot, A. (2017). Volatiles and energy released by Puracé volcano. Bulletin of Volcanology, 79–84. https://doi.org/10.1007/s00445-017-1168-y

Malinconico, L. L. Jr. (1987). On the variation of SO2 emission from volcanoes. Journal of Volcanology and Geothermal Research, 33, 231–237. https://doi.org/10.1016/0377-0273(87)90065-5

Martelli, M., Rizzo, A.L., Renzulli, A., Ridolfi, F., Arienzo, I., Rosciglione, A., 2014. Noble-gas signature of magmas from a heterogeneous mantle wedge: The case of Stromboli volcano (Aeolian Islands, Italy). Chem. Geol. 368, 39–53. https://doi.org/10.1016/j.chemgeo.2014.01.003

Martinez. N., 1932. Las grandes erupciones del Tungurahua de los años 19 16- 1918. Publicaciones del Observatorio Astronomico de Quito. Seccion de Geofisica. Quito (Ecuador).

Martínez, L.M., Valencia, L. G., Ceballos, J.A., Narváez, B.L., Pulgarín, B.A., Correa, A.M., Navarro, S.R., Murcia, H.F., Zuluaga, I., Rueda, J.B., Pardo, N., 2014. Geología y estratigrafía del Complejo Volcánico Nevado del Ruiz. Geología de volcanes, Dirección de Geociencias básicas. Servicio Geologico Colombiano.

Marty, B., 2012. The origins and concentrations of water, carbon, nitrogen and noble gases on Earth. Earth and Planetary Science Letters, Elsevier 313-314, 56-66. https://doi.org/10.1016/j.epsl.2011.10.040

Marty, B., Jambon, A., 1987. C/^{3}He in volatile fluxes from the solid Earth: implications for carbon geodynamics. Earth Planet. Sci. Lett. 83, 16-26. https://doi.org/10.1016/0012-821X(87)90047-1

Marty, B., Jambon, A., Sano, Y., 1989. Helium isotopes and CO_2 in volcanic gases of Japan. Chem. Geol. 76, 25–40. https://doi.org/10.1016/0009-2541(89)90125-3

Marty, B., and Tolstikhin, I. N. (1998). CO2 fluxes from mid-ocean ridges, arcs and plumes. Chemical Geology, 145, 233–248. https://doi.org/10.1016/S0009-2541(97)00145-9

Mason, E., Edmonds, M., Turchyn, A. V, 2017. Remobilization of crustal carbon may dominate volcanic arc emissions Science (80), 290–294. https://doi.org/10.1126/science.aan5049

Michelfelder, G.S., Feeley, T.C., Wilder, A.D., Klemetti, E.W., 2013. Modification of the Continental Crust by Subduction Zone Magmatism and Vice-Versa: Across-Strike Geochemical Variations of Silicic Lavas from Individual Eruptive Centers in the Andean Central Volcanic Zone. Geosciences, 3, pp. 633-667. doi:10.3390/geosciences3040633

Monsalve, M. L. (1996). Depósitos piroclásticos asociados a la actividad explosiva del volcán Puracé actual (Colombia), VIII Congreso Colombiano de Geología, Manizales, Tomo III.

Monsalve, M. L., and Pulgarín, B. (1993). Mapa preliminar de Amenaza Volcánica Potencial del Volcán Puracé. Memoria explicativa. Revista INGEOMINAS, 2, 3–27.

Montelli, R., Nolet, G., Dahlen, F.A., Masters, G., 2006. A catalogue of deep mantle plumes: New results from finitefrequency tomography. Geochemistry, Geophys. Geosystems 7. https://doi.org/10.1029/2006GC001248

Moreira, M., 2013. Noble gas constraints on the origin and evolution of earth's volatiles. Geochem. Perspec. 2, 229–230. https://doi.org/10.7185/geochempersp.2.2

Moreira, M., Blusztajn, J., Curtice, J., Hart, S., Dick, H., Kurz, M.D., 2003. He and Ne isotopes in oceanic crust: Implications for noble gas recycling in the mantle. Earth Planet. Sci. Lett. 216, 635–643. https://doi.org/10.1016/S0012-821X(03)00554-5

Moreira, M., Kunz, J., Allègre, C., 1998. Rare gas systematics in popping rock: Isotopic and elemental compositions in the upper mantle. Science (80) 279, 1178–1181. https://doi.org/10.1126/science.279.5354.1178

Mysen, B.O., Kushiro, I., Nicholls, I.A., Ringwood, A.E., 1974. A possible mantle origin for andesitic magmas: discussion of a paper by Nicholls and Ringwood. Earth Planet. Sci. Lett. 21, 221-229. https://doi.org/10.1016/0012-821X(74)90157-5

Mori, T., and Burton, M. (2006). The SO2 camera: A simple, fast and cheap method for ground-based imaging of SO2 in volcanic plumes. Geophysical Research Letters, 33, L24804. https://doi.org/10.1029/2006GL027916

Moussallam, Y., Peters, N., Masias, P., Apaza, F., Barnie, T., Schipper, C. I., et al. (2017). Magmatic gas percolation through the old lava dome of El Misti volcano. Bulletin of Volcanology, 46–79. https://doi.org/10.1007/s00445-017-1129-5

Moussallam, Y., Tamburello, G., Peters, N., Apaza, F., Schipper, C. I., Curtis, A., et al. (2017). Volcanic gas emissions and degassing dynamics at Ubinas and Sabancaya volcanoes; implications for the volatile budget of the central volcanic zone. Journal of Volcanology and Geothermal Research, 343, 181–191. https://doi.org/10.1016/j.jvolgeores.2017.06.027

N

Nicholls, I.A., Ringwood, A.E., 1972. Production of silica-saturated tholeiitic magmas in island arcs. Earth Planet. Sci. Lett. 17, 243–246. https://doi.org/10.1016/0012-821X(72)90282-8

Notsu, K., Nakai, S., Igarashi, G., Ishibashi, J., Mori, T., Suzuki, M., Wakita, H., 2001. Spatial distribution and temporal variation of 3He/4He in hot spring gas released from Unzen volcanic area, Japan. J. Volcanol. Geotherm. Res. 111, 89–98. https://doi.org/10.1016/S0377-0273(01)00221-9

O

Ojeda, A., Havskov, J., 2001. Crustal structure and local seismicity in Colombia. J. Seismol. 5, 575–593. https://doi.org/10.1023/A:1012053206408

Oppenheimer, C., Fischer, T.P., Scaillet, B., 2013. Volcanic Degassing: Process and Impact, 2nd ed, Treatise on Geochemistry: Second Edition. Elsevier Ltd. https://doi.org/10.1016/B978-0-08-095975-7.00304-1

Ozima, M., Igarashi, G., 2000. The primordial noble gases in the Earth: A key constraint on Earth evolution models. Earth Planet. Sci. Lett. 176, 219–232. https://doi.org/10.1016/S0012-821X(00)00005-4

Ozima, M., Podosek, F.A. 1983. Noble Gas Geochemistry, 367. Cambridge, London, New York, New Rochelle, Melbourne, Sydney: Cambridge University Press.

Ozima, M., Podosek, F.A. 2009. Noble Gases in the Earth. Noble Gas Geochemistry 217–252. https://doi.org/10.1017/cbo9780511545986.009

P

Panter, K.S., Kyle, P.R., Smellie, J.L., 1997. Petrogenesis of a phonolite-trachyte succession at Mount Sidley, Marie Byrd Land, Antarctica. J. Petrol. 38, 1225–1253. https://doi.org/10.1093/petroj/38.9.1225

Paonita, A., A. Caracausi, G. Iacono-Marziano, M. Martelli, A. Rizzo (2012), Geochemical evidence for mixing between fluids exsolved at different depths in the magmatic system of Mt Etna (Italy), Geochimica et Cosmochimica Acta, 84, 380-394. doi: 10.1016/j.gca.2012.01.028doi:10.1016/j.gca.2012.01.028.

Paonita, A., A. Caracausi, M. Martelli, A.L. Rizzo (2016), Temporal variations of helium isotopes in volcanic gases quantify pre-eruptive refill and pressurization in magma reservoirs: The Mount Etna case. Geology, G37807.1, doi: 10.1130/G37807.1.

Plank, T. (2014). The chemical composition of subducting sediments. Treatise on Geochemistry, 2(4), 607–629. https://doi.org/10.1016/B978-0-08-095975-7.00319-3

Plank, T., and Langumir, C. H. (1988). The chemical composition of subducting sediment and its consequences for the crust and mantle. Chemical Geology, 145, 325–394. https://doi.org/10.1016/S0009-2541(97)00150-2

Porcelli, D., Wasserburg, G.J., 1995. Mass transfer of helium, neon, argon, and xenon through a steady-state upper mantle. Geochim. Cosmochim. Acta 59, 4921–4937. https://doi.org/10.1016/0016-7037(95)00336-3

Porcelli, D., Woolum, D., Cassen, P., 2001. Deep earth rare gases: Initial inventories, capture from the solar nebula, and losses during moon formation. Earth Planet. Sci. Lett. 193, 237–251. https://doi.org/10.1016/S0012-821X(01)00493-9

Prévot, R., Chatelain, J.-L., Guillier, B., Yepes, H., 1996. Tomographie des Andes Équatoriennes: évidence d'une continuité des Andes Centrales. Comptes Rendus l'Académie des Sci. Paris 323, 833–840.

Protti, M., Giiendel, F., Mcnally, K., 1995. Correlation between the age of the subducting Cocos plate and the geometry of the Wadati-Benioff zone under Nicaragua and Costa Rica. Geol. Soc. Of America. https://doi.org/10.1130/SPE295-p309

Pulgarín, B., Correa, A. M., Cepeda, H. and Ancochea, E. (2001). Aspectos geológicos del complejo volcánico Nevado del Huila (CVNH). Popayán, INGEOMINAS.

Q

Queißer, M., Burton, M., and Kazahayaab, R. (2018). Insights into geological processes with CO2 remote sensing—A review of technology and applications. Earth Science Reviews, 188, 389–426. https://doi.org/10.1016/j.earscirev.2018.11.016

R

Rama, S.N.I., Hart, S.R., Roedder, E., 1965. Excess radiogenic argon in fluid inclusions. J. Geophys. Res. 70, 509-511. https://doi.org/10.1029/JZ070i002p00509

Reubi, O., Blundy, J., 2009. A dearth of intermediate melts at subduction zone volcanoes and the petrogenesis of arc andesites. Nature 461, 1269–1273. https://doi.org/10.1038/nature08510

Ridolfi, F., Puerini, M., Renzulli, A., Menna, M., Toulkeridis, T., 2008. The magmatic feeding system of El Reventador volcano (Sub-Andean zone, Ecuador) constrained by texture, mineralogy and thermobarometry of the 2002 erupted products. J. Volcanol. Geotherm. Res. 176, 94–106. https://doi.org/10.1016/j.jvolgeores.2008.03.003

Rizzo A.L., Caracausi, A., Favara, R., Martelli, M., Nuccio, P.M., Paonita, A., Rosciglione, A., Paternoster, M., 2006. New insights into magma dynamics during last two eruptions of Mount Etna as inferred by geochemical monitoring from 2002 to 2005. Geochem. Geophys. Geosyst., 7. https://doi.org/10.1029/2005GC001175

Rizzo, A.L, Grassa, F., Inguaggiato, S., Liotta, M., Longo, M., Madonia, P., Brusca, L., Capasso, G., Morici, S., Rouwet, D., Vita, F., 2009. Geochemical evaluation of observed changes in volcanic activity during the 2007 eruption at Stromboli (Italy). J. Volcanol. Geot. Res. 182, 246–254. https://doi.org/10.1016/j.jvolgeores.2008.08.004

Rizzo, A.L., Federico, C., Inguaggiato, S., Sollami, A., Tantillo, M., Vita, F., Bellomo, S., Longo, M., Grassa, F., Liuzzo, M., 2015a. The 2014 effusive eruption at Stromboli volcano (Italy): Inferences from soil CO_2 flux and $^3He/^4He$ ratio in thermal waters. Geophys. Res. Lett., 42(7), 2235-2243. https://doi.org/10.1002/2014GL062955

Rizzo, A.L., Barberi, F., Carapezza, M.L., Di Piazza, A., Francalanci, L., Sortino, F., D'Alessandro, W., 2015b. New mafic magma refilling a quiescent volcano: Evidence from He-Ne-Ar isotopes during the 2011–2012 unrest at Santorini, Greece. Geochem. Geophys. Geosyst., 16, 798-814. https://doi.org/10.1002/2014GC005653.

Rizzo, A.L., Di Piazza, A., de Moor, J.M., Alvarado, G.E., Avard, G., Carapezza, M.L., Mora, M.M., 2016. Eruptive activity at Turrialba volcano (Costa Rica): Inferences from $^3He/^4He$ in fumarole gases and chemistry of the products ejected during 2014 and 2015. Geochem. Geophys. Geosyst., 17, 4478–4494. https://doi.org/10.1002/2016GC006525.

Rizzo, A.L., Pelorosso, B., Coltorti, M., Ntaflos, T., Bonadiman, C., Matusiak-Małek, M., Italiano, F., Bergonzoni, G., 2018. Geochemistry of noble gases and CO_2 in fluid inclusions from lithospheric mantle beneath Wilcza Góra (Lower Silesia, Southwest Poland). Frontiers in Earth Sciences 6, 215. https://doi.org/10.3389/feart.2018.00215.

Robidoux, P., Aiuppa, A., Rotolo, S.G., Rizzo, A.L., Hauri, E.H., Frezzotti, M.L., 2017. Volatile contents of mafic-to-intermediate magmas at San Cristóbal volcano in Nicaragua. Lithos 272–273, 147–163. https://doi.org/10.1016/j.lithos.2016.12.002

Rudnick, R.L., Gao, S., 2013. Composition of the Continental Crust, 2nd ed, Treatise on Geochemistry: Second Edition. Elsevier Ltd. https://doi.org/10.1016/B978-0-08-095975-7.00301-6

Rudnick, R.L., 1995. Nature Crust: and Composition of the Continental Perspective. Phys. Earth Planet. Inter. 145, 267–309.

S

Samaniego, P., Eissen, J.P., Le Pennec, J.L., Robin, C., Hall, M.L., Mothes, P., Chavrit, D., Cotten, J., 2008. Pre-eruptive physical conditions of El Reventador volcano (Ecuador) inferred from the petrology of the 2002 and 2004-05 eruptions. J. Volcanol. Geotherm. Res. 176, 82–93. https://doi.org/10.1016/j.jvolgeores.2008.03.004

Samaniego, P., Le Pennec, J.L., Robin, C., Hidalgo, S., 2011. Petrological analysis of the pre-eruptive magmatic process prior to the 2006 explosive eruptions at Tungurahua volcano (Ecuador). J. Volcanol. Geotherm. Res. 199, 69–84. https://doi.org/10.1016/j.jvolgeores.2010.10.010

Samaniego, P., Martin, H., Monzier, M., Robin, C., Fornari, M., Eissen, J.P., Cotten, J., 2005. Temporal evolution of magmatism in the Northern Volcanic Zone of the Andes: The geology and petrology of Cayambe volcanic complex (Ecuador). J. Petrol. 46, 2225–2252. https://doi.org/10.1093/petrology/egi053

Sang, Y., Wakita, H., 1987. Helium isotopes and heat flow on the ocean floor. Chem. Geol. Isot. Geosci. Sect. 66, 217–226. https://doi.org/10.1016/0168-9622(87)90043-1

Sang, Y., Wakita, H., 1988. Helium isotope ratio and heat discharge rate in the Hokkaido Island, Northeast Japan. Geochem. J. 22, 293-303. https://doi.org/10.2343/geochemj.22.293

Sano, Y., Wakita, H., 1985a. Geographical distribution of $^{3}He/^{4}He$ ratios in Japan: implications for arc tectonics and incipient magmatism. J. Geophys. Res. 90, 8729–8741. https://doi.org/10.1029/JB090iB10p08729

Sano, Y., Gamo, T., Williams, S.N., 1997. Secular variations of helium and carbon isotopes at Galeras volcano, Colombia. J. Volcanol. Geotherm. Res. 77, 255–265. https://doi.org/10.1016/S0377-0273(96)00098-4

Sano, Y., Kagoshima, T., Takahata, N., Nishio, Y., Roulleau, E., Pinti, D.L., Fischer, T.P., 2015. Ten-year helium anomaly prior to the 2014 Mt Ontake eruption. Sci. Rep. 5, 1–7. https://doi.org/10.1038/srep13069

Sano, Y., Marty, B., 1995. Origin of carbon in fumarolic gas from island arcs. Chem. Geol. 119, 265-274. https://doi.org/10.1016/0009-2541(94)00097-R

Sano, Y., Nakamura, Y., Wakita, H., Urabe, A., Tominaga, T., 1984. Helium-3 Emission Related to Volcanic Activity Science, 224,150-151. https://doi.org/10.1126/science.224.4645.150

Sano, Y., Takahata, N., Seno, T., 2006. Geographical distribution of 3He/4He ratios in the Chugoku District, Southwestern Japan. Pure Appl. Geophys. 163, 745–757. https://doi.org/10.1007/s00024-006-0035-0

Sano, Y., Wakita, H., Williams, S.N., 1990. Helium-isotope systematics at Nevado del Ruiz volcano, Colombia: implications for the volcanic hydrothermal system. J. Volcanol. Geotherm. Res. 42, 41–52. https://doi.org/10.1016/0377-0273(90)90068-Q

Sano, Y., Williams, S.N., 1996. Fluxes of mantle and subducted carbon along convergent plate boundaries. Geophys. Res. Lett. 23, 2749-2752. https://doi.org/10.1029/96GL02260

Sarda, P., Staudacher, T., Allègre, C.J., 1988. Neon isotopes in submarine basalts. Earth Planet. Sci. Lett. 91, 73–88. https://doi.org/10.1016/0012-821X(88)90152-5

Scarsi, P., 2000. Fractional extraction of helium by crushing of olivine and clinopyroxene phenocrysts: Effects on the $^{3}He/^{4}He$ measured ratio. Geochimica et Cosmochimica Acta, 64, 3751–3762. https://doi.org/10.1016/S0016-7037(00)00419-1

Schiano, P., Monzier, M., Eissen, J.P., Martin, H., Koga, K.T., 2010. Simple mixing as the major control of the evolution of volcanic suites in the Ecuadorian Andes. Contrib. to Mineral. Petrol. 160, 297–312. https://doi.org/10.1007/s00410-009-0478-2

Schipper, C. I., Moussallam, Y., Curtis, A., Peters, N., Bernie, T., Bani, P., et al. (2017). Isotopically (δ13C and δ18O) heavy volcanic plumes from Central Andean volcanoes: A field study. Bulletin of Volcanology, 79(65). https://doi.org/10.1007/s00445-017-1146-4

Sano, Y., T. Kagoshima, N. Takahata, Y. Nishio, E. Roulleau, D.L. Pinti, T.P. Fischer (2015), Ten-year helium anomaly prior to the 2014 Mt Ontake eruption, Scientific reports, 5.

Schwandner, F. M., Gunson, M. R., Miller, C. E., Carn, S. A., Eldering, A., Krings, T., et al. (2017). Spaceborne detection of localized carbon dioxide sources. Science, 358(6360). https://doi.org/10.1126/science.aam5782

Shaw, A.M., Hilton, D.R., Fischer, T.P., Walker, J.A., de Leeuw, G.A.M., 2006. Helium isotope variations in mineral separates from Costa Rica and Nicaragua: Assessing crustal contributions, timescale variations and diffusion-related mechanisms. Chem. Geol. 230, 124–139. https://doi.org/10.1016/j.chemgeo.2005.12.003

Shinohara, H. (2005). A new technique to estimate volcanic gas composition: plume measurements with a portable multi-sensor system. Journal of Volcanology and Geothermal Research, 143, 319–333. https://doi.org/10.1016/j.jvolgeores.2004.12.004

Shinohara, H. (2013). Volatile flux from subduction zone volcanoes: Insights from a detailed evaluation of the fluxes from volcanoes in Japan. Journal of Volcanology and Geothermal Research, 268, 46–63. https://doi.org/10.1016/j.jvolgeores.2013.10.007

Shinohara, H., Aiuppa, A., Giudice, G., Gurrieri, S., and Liuzzo, M. (2008). Variation of H_2O/CO_2 and CO_2/SO_2 ratios of volcanic gases discharged by continuous degassing of Mount Etna volcano, Italy. Journal of Geophysical Research, 113, B09203. https://doi.org/10.1029/2007JB005185

Siebert, L., Cottrell, E., Venzke, E. & Andrews, B. Earth's Volcanoes and Their Eruptions: An Overview, In Te Encyclopedia of Volcanoes (Second Edition). (eds Sigurdsson, H., Houghton, B., McNutt, S., Rymer, H. and Stix, J.). Academic Press, Elsevier,239–254, 2015.

Smye, A.J., Jackson, C.R.M., Konrad-Schmolke, M., Hesse, M.A., Parman, S.W., Shuster, D.L., Ballentine, C.J., 2017. Noble gases recycled into the mantle through cold subduction zones. Earth Planet. Sci. Lett. 471, 65–73. https://doi.org/10.1016/j.epsl.2017.04.046

Sobolev, A. V., Chaussidon, M., 1996. H_2O concentrations in primary melts from supra-subduction zones and mid-ocean ridges: Implications for H2O storage and recycling in the mantle. Earth Planet. Sci. Lett. 137, 45–55. https://doi.org/10.1016/0012-821x(95)00203-o

Stix, J., Calvache, M. L., and Williams, S. N. (1997). Galeras volcano, Colombia: Interdisciplinary study of a Decade volcano. Journal of Volcanology and Geothermal Research, 77(1-4). https://doi.org/10.1016/S0377-0273(96)00082-0

Stix, J., and de Moor, J. (2018). Understanding and forecasting phreatic eruptions driven by magmatic degassing. Earth, Planets and Space, 70,v10–83. https://doi.org/10.1186/s40623-018-0855-z

Stix, J., Zapata, J. A., Calvache, M. L., Cortes, G. P., Fischer, T. P., Gomez, D., et al. (1993). A model of degassing at Galeras volcano,vColombia, 1988–1993. Geology, 21, 963–967. https://doi.org/10.1130/0091v7613(1993)021<0963:AMODAG>2.3.CO;2

Sturchio, N. C., Williams, S. N., Garcia, N. P., and Londono, A. C. (1988). The hydrothermal system of Nevado del Ruiz volcano, Colombia. Bulletin of Volcanology, 50(6), 399–412. https://doi.org/10.1007/BF01050639

Sturchio, N. C., Williams, S. N., and Sano, Y. (1993). The hydrothermal system of Volcan Puracé, Colombia. Bulletin of Volcanology, 55, 289–296. https://doi.org/10.1007/BF00624356

Syracuse, E. M., and Abers, G. A. (2006). Global compilation of variations in slab depth beneath arc volcanoes and implications. Geochemistry, Geophysics, Geosystems, 7, Q05017. https://doi.org/10.1029/2005GC001045

T

Tamburello, G. (2015). Ratiocalc: Software for processing data from multicomponent volcanic gas analyzers. Computational Geosciences,82, 63–67. https://doi.org/10.1016/j.cageo.2015.05.004

Tamburello, G., Agusto, M., Caselli, A., Tassi, F., Vaselli, O., Calabrese, S., et al. (2015). Intense magmatic degassing through the lake of Copahue volcano, 2013–2014. Journal of Geophysical Research: Solid Earth, 120, 6071–6084. https://doi.org/10.1002/2015JB012160

Tamburello, G., Aiuppa, A., Kantzas, E. P., McGonigle, A. J. S., and Ripepe, M. (2012). Passive vs. active degassing modes at an open-vent volcano (Stromboli, Italy). Earth and Planetary Sciences Letters, 359–360, 106–116. https://doi.org/10.1016/j.epsl.2012.09.050

Tamburello, G., Hansteen, T., Bredemeyer, S., Aiuppa, A., and Tassi, F. (2014). Gas emissions from five volcanoes in northern Chile and implications for the volatiles budget of the Central Volcanic Zone. Geophysical Research Letters, 41, 4961–4969. https://doi.org/10.1002/2014GL060653

Tamburello, G., Kantzas, E. P., McGonigle, A. J. S., and Aiuppa, A. (2011). Vulcamera: A program for measuring volcanic SO2 using UV cameras. Annals of Geophysics, 54(2), 219–221. https://doi.org/10.4401/ag-5181

Tamburello, G., Kantzas, E. P., McGonigle, A. J. S., Aiuppa, A., and Gaetano, G. (2011). UV camera measurements of fumarole field degassing (La Fossa crater, Vulcano Island). Journal of Volcanology and Geothermal Research, 199(1-2), 47–52. https://doi.org/10.1016/j. jvolgeores.2010.10.004

Tamburello, G., Pondrelli, S., Chiodini, G., and Rouwet, D. (2018). Global-scale control of extensional tectonics on CO2 Earth degassing. Nature Communications, 9. https://doi.org/10.1038/s41467-018-07087-z

Tatsumi, Y., 1989. Migration of fluid phases and genesis of basalt magmas in subduction zones. J. Geophys. Res. 94, 4697–4707. https://doi.org/10.1029/JB094iB04p04697

Tassi, F., Vaselli, O., Barboza, V., Fernandez, E., Duarte, E., 2004. Fluid geochemistry and seismic activityin the period 1998-2002 at Turrialba Volcano (Costa Rica). Annals of Geophysics 47, 1501-1511. https://doi.org/10.4401/ag-3355

Thouret, J. C., Cantagrel, J. M., Salinas, R., and Murcia, S. (1990). Quaternary eruptive history of Nevado del Ruiz (Colombia). Journal of Volcanology and Geothermal Research, 41, 225–251. https://doi.org/10.1016/0377-0273(90)90090-3

Thouret, J. C., Vatin-Perignon, N., Cantagrel, J. M., Salinas, R., and Murcia, A. (1985). Le Nevado del Ruiz (Cordillere Central des Andes de Colombie): Stratigraphie, structures et dynamisme d'un appareil volcanique andesitique, compose et polygenique. Revue de géologie dynamique et de géographie physique, 26, 257–271.

Trenkamp, R., Kellogg, J.N., Freymueller, J.T., Mora, H.P., 2002. Wide plate margin deformation, southern Central America and northwestern South America, CASA GPS observations. J. South Am. Earth Sci. 15, 157–171. https://doi.org/10.1016/S0895-9811(02)00018-4

Trull, T.W., Kurz, M.D., 1993. Experimental measurements of 3He and 4He mobility in olivine and clinopyroxene at magmatic temperatures. Geochim. Cosmochim. Acta 57, 1313–1324. https://doi.org/10.1016/0016-7037(93)90068-8

Trull, T.W., Kurz, M.D., 1999. Isotopic fractionation accompanying helium diffusion in basaltic glass. J. Mol. Struct. 485–486, 555–567. https://doi.org/10.1016/S0022-2860(99)00057-5

U

Umeda, K., Asamori, K., Ninomiya, A., Kanazawa, S., Oikawa, T., 2007. Multiple lines of evidence for crustal magma storage beneath the Mesozoic crystalline Iide Mountains, northeast Japan. J. Geophys. Res. Solid Earth 112, 1–9. https://doi.org/10.1029/2006JB004590

V

van der Hilst R.D., Widiyantoro S., Engdahl, E.R., 1997. Evidence for deep mantle circulation from global tomography. Nature 386, 578-584. https://doi.org/10.1038/386578a0

van Keken, P.E., Ballentine, C.J., 1999. Dynamical models of mantle volatile evolution and the role of phase transitions and temperature-dependent rheology. J. Geophys. Res. Solid Earth 104, 7137–7151. https://doi.org/10.1029/1999jb900003

van Keken, P.E., Hauri, E.H., Ballentine, C.J., 2002. Mantle Mixing: The Generation, Preservation, and Destruction of Chemical Heterogeneity. Annu. Rev. Earth Planet. Sci. 30, 493–525. https://doi.org/10.1146/annurev.earth.30.091201.141236

Vatin-Pérignon, N., Goemans, P., Oliver, R.A., Briqueu, L., Thouret, J.C., Salinas, R., Murcia, A., 1988. Magmatic evolution of the Nevado del Ruiz volcano, Central Cordillera, Colombia: Mineral chemistry and geochemistry. Géodynamique, ORSTOM 3, 163–194.

Van Soest, M.C., Hilton, D.R., Kreulen, R., 1998. Tracing crustal and slab contributions to arc magmatism in the Lesser Antilles island arc using helium and carbon relationships in geothermal fluids. Geochim. Cosmochim. Acta 62, 3323–3335. https://doi.org/10.1016/S0016-7037(98)00241-5

Vatin-Pérignon, N., Goemans, P., Oliver, R.A., Palacio, E.P., 1990. Evaluation of magmatic processes for the products of the Nevado del Ruiz Volcano, Colombia from geochemical and petrological data. J. Volcanol. Geotherm. Res. 41, 153–176. https://doi.org/10.1016/0377-0273(90)90087-V

Voight, B. (1990). The 1985 Nevado del Ruiz volcano catastrophe: Anatomy and retrospection. Journal of Volcanology and Geothermal Research, 44, 349–386. https://doi.org/10.1016/0377-0273(90)90027-D

Voight, B., Calvache, M. L., Hall, M. L., and Monsalve, M. L. (2016). Nevado del Ruiz volcano, Colombia 1985. In P. T. Bobrowsky (Ed.), Encyclopedia of natural hazards. Encyclopedia of Earth Sciences Series (pp. 732–738). Dordrecht: Springer. https://doi.org/10.1007/978-1- 4020-4399-4_253

von Huene, R., and Scholl, D. W. (1991). Observations at convergent margins concerning sediment subduction, subduction erosion, and the growth of continental crust. Reviews of Geophysics, 29, 279–316. https://doi.org/10.1029/91RG00969

W

Wallace, P. J., Gerlach, T. M., 1994. Magmatic vapor source for sulfur dioxide released during volcanic eruptions: evidence from Mount Pinatubo. Science, 265, 497–499.

Wallace, P. J., Plank, T., Edmonds, M., and Hauri, E. H. (2015). Volatiles in magmas. In H. Sigurdsson, B. Houghton, S. McNutt, H. Rymer, andJ. Stix (Eds.), The encyclopedia of volcanoes (2nd ed., pp. 163–183). San Diego, CL: Elsevier Inc., Academic Press.

Weber, M.B.I., Tarney, J., Kempton, P.D., Kent, R.W., 2002. Crustal make-up of the northern Andes: evidence based on deep crustal xenolith suites, Mercaderes, SW Colombia. Tectonophysics, 345, 49–82. https://doi.org/10.1016/S0040-1951(01)00206-2

Wegner, W., Wörner, G., Harmon, R.S., Jicha, B.R., 2011. Magmatic history and evolution of the Central American Land Bridge in Panama since Cretaceous times. GSA Bulletin 123, 703-724. https://doi.org/10.1130/B30109.1

Williams, S.N., Sano, Y., Wakita, H., 1987. Helium-3 emission from Nevado del Ruiz, Colombia. Geophys. Res. Lett. 14, 1035–1038. https://doi.org/10.1029/GL014i010p01035